



UNIVERSITAT POLITÈCNICA DE CATALUNYA

BARCELONATECH

Escola d'Enginyeria de Telecomunicació
i Aeroespacial de Castelldefels

TREBALL DE FI DE GRAU

TFG TITLE: Inductive Energy Transfer System based on Drone

DEGREE: Grau en Enginyeria d'Aeronavegació

AUTHORS: Lluís Hontecillas
Ignacio Izquierdo

ADVISOR: Óscar Casas

DATE: 29 de febrer de 2016

Título: Sistema Inductivo de Transferencia de Energía basado en Drone

Autores: Lluís Hontecillas
Ignacio Izquierdo

Director: Óscar Casas

Fecha: 29 de febrer de 2016

Resumen

El objetivo de este proyecto es modelar y validar un sistema inductivo con el fin de ser capaz de alimentar de forma inalámbrica un sensor. Así pues, el diseño del sistema debe ser lo suficientemente pequeño y ligero para cumplir los requisitos del nano-cuadricóptero, en el que el sistema va a ser equipado. Recientes investigaciones sobre sistemas inductivos añadidas a la tendencia de *Energy Harvesting* predicen un futuro basado en la energía inalámbrica. Por lo tanto, surge la posibilidad de dejar atrás la actual dependencia de la alimentación de dispositivos mediante cable.

Al principio del trabajo, se exponen detalladamente las bases de la inducción de resonancia magnética con tal de entender como la energía puede ser transferida. A continuación, se presenta un modelo inductivo basado en dos bobinas resonantes; exponiendo sus características principales, así como el comportamiento de las variables de la bobina y sus efectos. Por ello, se definen diferentes bobinas usando la configuración resonante más adecuada con tal de transferir la máxima potencia.

Una vez definido el modelo, numerosas mediciones de las bobinas de ensayo, bajo diferentes condiciones, son llevadas a cabo para validarla, y así seleccionar las más adecuadas para su implementación en el sistema inductivo. La arquitectura y el diseño del sistema de transferencia de energía inalámbrica se estudian centrándonos en el transmisor y el receptor individualmente. Mientras en el circuito transmisor se ha intentado optimizar el peso, un hecho recurrente a lo largo del proyecto, en el circuito receptor se ha intentado adquirir y gestionar de manera eficiente los milivatios de potencia recibidos.

Al final del proyecto se emplea un sensor de temperatura como aplicación demostrativa. El experimento muestra satisfactoriamente la transferencia de potencia inalámbrica para la configuración resonante seleccionada. El sistema es capaz de cargar la batería y alimentar el sensor de manera conjunta.

Title : Inductive Energy Transfer System based on Drone

Authors: Lluís Hontecillas
Ignacio Izquierdo

Advisor: Óscar Casas

Date: February 29, 2016

Overview

The aim of this project is to model and validate an inductive system in order to be able to power wirelessly a sensor. The design of the inductive system must be small and light enough to fulfil the requirements of a nano-quadcopter, in which the system is going to be outfitted. Recent investigations about inductive systems added to the *Energy Harvesting* trend, predict a future based on wireless power. Thereby, the possibility to change the current “wire-dependence” of any device.

At the beginning the bases of magnetic resonant induction are given in detail to understand how the energy can be transferred. Then, an inductive model based on two resonant coils is presented. Its main features are explained, as well as the behaviour of the coil variables and their effects. Some coils are defined to be tested using the most suitable resonant configuration. Hence, providing that our purpose is not to optimize efficiency, but to achieve higher receiver power levels.

Once the model is defined, numerous measurements of the test coils, under different conditions, are performed to validate the model, and so select the most suitable coils for our inductive system. The architecture and design of the wireless power transfer system are studied separately; transmitter and receiver. While attempting to minimize the weight at transmitter’s side, a recurring topic during the project, on the receiver side it is intended to efficiently acquire and manage the microwatts to milliwatts of power generated from the transmitter.

At the end of the project a temperature sensor is introduced as a technology demonstration. The experiment results shows successfully wireless power transfer for the resonant configuration selected, being able to completely charge the battery and to power the temperature sensor, at the same time.

CONTENTS

CHAPTER 1. Introduction	1
1.1 Motivation of the Project	1
1.2 Objectives	1
1.3 Brief History	2
1.4 Category for the Wireless Power Transfer Systems	2
1.5 Discussion	3
CHAPTER 2. Modeling Magnetic Induction System	7
2.1 Magnetic Field	7
2.2 Magnetic Induction	8
2.2.1 Magnetic Flux	8
2.2.2 Induced EMF and Faraday's Law	9
2.2.3 Inductance	9
2.3 Resonance	11
2.3.1 Energy Pendulum	11
2.3.2 Series Resonance	13
2.3.3 Parallel Resonance	14
2.4 Characterizing the Inductor	14
2.4.1 Coil Resistance	16
2.4.2 Coil Inductance	18
2.4.3 Coil Parasitic Capacitor	18
2.5 Coreless Transformer Modeling	19
2.5.1 Electrical Circuit	19
2.5.2 Compensation Topologies	22
2.6 Design Considerations	29
2.6.1 Power Level	29
2.6.2 Quality Factor	30
2.6.3 Coupling Factor	31
2.6.4 Operating Frequency	31
2.6.5 Size and Weight	33

2.7 Detailed Designs	37
2.7.1 Discussion	38
CHAPTER 3. Architecture and Design of the WPT System	41
3.1 Quadcopter	41
3.1.1 Controlling the <i>Crazyflie</i>	42
3.1.2 Motor Mount Design	43
3.2 Transmission System	44
3.2.1 Power Source	44
3.2.2 Voltage Regulator	45
3.2.3 Oscillator	46
3.2.4 Power Driver	47
3.2.5 Transmitter Circuit Assembly	49
3.3 Receiver system	50
3.3.1 Voltage Doubler	51
3.3.2 DC-DC boost converter	52
3.3.3 Storage element	53
3.3.4 Application	54
3.3.5 Receiver Circuit Assembly	54
CHAPTER 4. Experimental Results	57
4.1 Validations and Measurements	57
4.1.1 Resistance Estimation	57
4.1.2 Inductance Estimation	58
4.1.3 Quality Factor	58
4.1.4 Inductive System Performance	59
4.1.5 Overall System Performance	61
Conclusions	65
Bibliography	67
APPENDIX A. Inductance Characterization	73
A.1 Inductance Estimation Table	73
A.2 Equivalent coil impedance	73

APPENDIX B. Model equations	75
B.1 Secondary capacitor in series	75
B.2 Secondary capacitor in parallel	75
B.3 Primary capacitor in series	76
B.4 Primary capacitor in parallel	76
APPENDIX C. Coils Experimental Results	79
C.1 Inductance and Resistance	79
C.2 Quality Factor	80
APPENDIX D. Circuit Schematics	81
D.1 Voltage Regulator	81
D.2 Power Driver	81
D.3 Transmitter	82
D.4 Receiver	83
APPENDIX E. Experimental Results	85
E.1 Model A	85
E.2 Model B	90
E.3 Model C	95
E.4 Output power for models D1 and D2	100
APPENDIX F. Programming Code	103

LIST OF FIGURES

1.1	Types of wireless power transfer inside the EM spectrum	5
2.1	Geometry for calculating the magnetic field at a point on the z axis	8
2.2	Magnetic field lines from transmitter to receiver coil	9
2.3	Voltage and current behaviour inside a LC circuit	12
2.4	Series resonance	13
2.5	Series RLC circuit	14
2.6	Parallel resonance	14
2.7	Parallel RLC circuit	15
2.8	Modeling of a single magnetic coil	15
2.9	Skin depth and resistance varying frequency for a fixed coil	17
2.10	General electric circuit	20
2.11	Reflected impedance circuit schematic	21
2.12	Equivalent impedance circuit schematic	22
2.13	Compensation topologies	23
2.14	Equivalent circuit impedance w.r.t frequency for SS topology	25
2.15	Equivalent circuit impedance w.r.t frequency for SP topology	25
2.16	Equivalent circuit impedance w.r.t frequency for PS topology	26
2.17	Equivalent circuit impedance w.r.t frequency for PP topology	26
2.18	Efficiency for all topologies	27
2.19	Output power for all topologies	27
2.20	Output power for SS and SP topologies varying the load resistance	28
2.21	Output power for SS and SP topologies varying the load resistance	28
2.22	Voltage transfer function over frequency for different systems	30
2.23	Frequency band constraints	32
2.24	Inductance w.r.t. wire diameter for fixed coil radius of 4 cm and different turns	34
2.25	Calculated inductance for different number of turns and coil radii values . .	35
2.26	Contour lines of the magnetic coupling obtained for different distances . . .	36
2.27	Flowchart of the algorithm to design the coil size	38
3.1	Block diagram	41
3.2	Transmitter circuit	42
3.3	Crazyflie 2.0 features	42
3.4	Crazyflie's computer client	43
3.5	Motor mount process design	43
3.6	Crazyflie's battery size	44
3.7	TPS61088 design circuit	45
3.8	Oscillator schematic	46
3.9	Simplified transistor diagram	48
3.10	Transmitter SMD design	49
3.11	Transmitter circuit	49
3.12	Thrust depending on the power level of the motors	50
3.13	Single voltage doubler stage	51
3.14	SOT-23 Package for HSMS-2850 Schottky diode	51

3.15	Single voltage doubler stage	52
3.16	<i>bq25504 EVM</i> schematic	53
3.17	<i>eZ430-RF2500</i> debugging interface (left) and target board (right)	54
3.18	Receiver circuit	55
4.1	Experimental quality factor of model coils	59
4.2	Measuring procedure	62
4.3	Nano-quadcopter's battery discharging profile	63
4.4	Overall system measurement.	63
C.1	Inductance and resistance w.r.t. frequency	80
C.2	Experimental quality factor	80
D.1	Efficiency w.r.t. output current	81
D.2	ULN2803 Darlington driver	81
D.3	Transmitter circuit schematic	82
D.4	Receiver circuit schematic	83
E.1	Efficiency w.r.t. distance for SS topology	85
E.2	Output power w.r.t. distance for SS topology	86
E.3	Efficiency w.r.t. distance for SP topology	86
E.4	Output power w.r.t. distance for SP topology	87
E.5	Efficiency w.r.t. load resistance for SS topology	88
E.6	Output power w.r.t. load resistance for SS topology	88
E.7	Efficiency w.r.t. load resistance for SP topology	89
E.8	Output power w.r.t. load resistance for SP topology	90
E.9	Efficiency w.r.t. distance for SS topology	90
E.10	Output power w.r.t. distance for SS topology	91
E.11	Efficiency w.r.t. distance for SP topology	92
E.12	Output power w.r.t. distance for SP topology	92
E.13	Efficiency w.r.t. load resistance for SS topology	93
E.14	Output power w.r.t. load resistance for SS topology	94
E.15	Efficiency w.r.t. load resistance for SP topology	94
E.16	Output power w.r.t. load resistance for SP topology	95
E.17	Efficiency w.r.t. distance for SS topology	96
E.18	Output power w.r.t. distance for SS topology	96
E.19	Efficiency w.r.t. distance for SP topology	97
E.20	Output power w.r.t. distance for SP topology	98
E.21	Efficiency w.r.t. load resistance for SS topology	98
E.22	Output power w.r.t. load resistance for SS topology	99
E.23	Efficiency w.r.t. load resistance for SP topology	100
E.24	Output power w.r.t. load resistance for SP topology	100
E.25	Experimental demonstration of the output power depending on the coil receiver radius	101

LIST OF TABLES

1.1	A comparison among the wireless power transfers	4
2.1	Electric parameters	19
2.2	Arbitrary values of the electric parameters	24
2.3	Geometric parameters of coil models.	33
2.4	Electrical resistivity of several common metal conductors	34
2.5	Wire diameter	35
2.6	Geometric parameters of coil models	37
3.1	Battery's electrical specifications	44
3.2	Regulator requirements	45
3.3	XO parameters	47
3.4	Electrical characteristics	48
3.5	Switching characteristics	49
3.6	Mass constraint at transmitter side	50
3.7	SPICE parameters for HSMS-2850	52
4.1	Inductance calculation and measurement results	57
4.2	Inductance calculation and measurement results	58
4.3	Self-frequencies	59
4.4	Consumption comparison	64
A.1	Coefficient K	73

CHAPTER 1. INTRODUCTION

1.1 Motivation of the Project

In the last years, our society has experienced a silent, but intense trend towards autonomous electronic devices (e.g. laptops, digital cameras, smartphones, smartwatches, etc.) that we use in our daily life. In most cases, these devices are powered by batteries, which need to be charged very often. Conventional recharges are made through the use of wires transmitting electrical energy from the generating point to the electrical device, but it has many problems related to alternating electric current while distribution. Even so, the greatest drawback is the lack of mobility. Moreover consumers have become inside a recharging lifestyle led by the combination of high-performance handheld electronics with a current battery technology incapable to satisfy consumers' desire.

This fact motivated us to wonder whether there exist physical principles that could enable wireless powering of these and similar devices. Different technologies allow contactless energy transfer, each of them with their respective pros and cons. Recent investigations made us move towards inductive coupling systems due to its safety, lack of interference, and efficiency at medium ranges.

1.2 Objectives

The aim of this project is to accomplish a brand new concept of inductive coupling implementing and outfitting the induction system on a nano-quadcopter with restrictive payload capabilities. A flying energy transporter widens the prospects and possibilities of unmanned aerial vehicles in such different fields, as aerospace, biomedical, multisensors, smart farming and robotics applications.

The study and modeling a resonant inductive system permits to design any inductive system by only having the requirements, such as power level or transfer distance. Based on different papers and projects, we decide to design the system with the purpose of transferring power up to 20 cm. This distance will constraint the dimensions of the inductive coils carried by the quadcopter.

One of the important goals of this project is to design and implement the inductive system inside a closed *system* such as the nano-quadcopter. To achieve this, a strict calculation of performance and weight of each circuit should be made in order not to exceed the maximum take-off mass.

Eventually, it is intended to demonstrate our system by powering a sensor, and also charging a small battery. Depending on the overall circuit efficiency and on the carrying energy, the transfer distance could be increased or reduced.

1.3 Brief History

The idea of Wireless Power Transfer (WPT) is almost 200 years old. In 1826 Andre-Marie Ampere developed Ampere's circuital law, which shows the capacity of the electric current to produce a magnetic field. Five years later, Michael Faraday developed in England the Faraday's law of induction describing electromagnetic force can be induced in a conductor by a time-varying magnetic flux. In the United States Joseph Henry, independently to Faraday, discovers the same induced currents. [1]

In 1867 James Maxwell predicted the existence of electromagnetic waves. Twenty years later, the first spark transmitter generated a spark in a receiver that was several meters away from it. The German physicist Heinrich Hertz proved the existence of electromagnetic waves using this example [2].

The Serbian American inventor and engineer Nikola Tesla learned of Hertz's work by the following year and began duplicating his experiments.

In 1891, before the electrical-wire grid, Tesla proposed the first WPT theories [3] carrying out various wireless transmission and reception experiments though air or matter. But, it was in 1894 when Tesla developed the equipment to wirelessly light incandescent lamps at his New York laboratory. This method used Resonant Inductive Coupling (RIC), which involves tuning two nearby coils to resonate at the same frequency. After this, no significant advances were made for more than 50 years.

In 1969, Peter Glaser propose a transmission power link from space down the Earth. The project was named *Solar Power Satellite* and it was based in harvesting solar radiation in space using satellites, which would convert it to microwave energy and then transmit it to Earth for use in electrical power systems.

In the early 1970s, experiments with RFID tags, done by the U.S. government [4], began and by the early 2000's the Professor She Yuen developed a charger to provide resonant power transfer for small electronics.

Recently, in 2007 MIT researchers were able to power a 60 Watt light bulb from a power source while providing forty percent efficiency over distance in excess of two meters using RIC. Until that moment, the maximum transfer distances achieved between transmitter and receiver were on centimeter range scale. This event signified a turning point in WPT systems. In 2009 Sony showed a wireless electrodynamic-induction powered TV set, 60 V over 50 cm. Haier showed a wireless LCD TV at CES 2010 using researched Wireless Home Digital Interface [5].

In July 2010 wireless charging technology for portable electronic devices up to 5 W reached commercialization stage through the launch of the *Qi* Standard by the Wireless Power Consortium, now comprising over 135 companies worldwide. Practically, it means that all receivers under *Qi* specification can be supplied by all transmitters, signed with *Qi* Standard, embracing compatibility between different devices.

1.4 Category for the Wireless Power Transfer Systems

Wireless energy transfer systems, also called wireless power transfer (WPT), basically work by modulating the generated electric, magnetic, or electromagnetic fields to transport

power from a transmitter towards a receiver at certain distance.

WPT systems can be cataloged by many ways, for example by the efficiency, power level, operating frequency, transmission distance, and so on. In this project, we classify the category of wireless power transfer systems by the working range. Figure 1.1 shows the category.

As above figure shows, there are two basic sorts. They are the near-field transfers and the far-field transfers, since the field propagation behaviour and the consequent propagation losses strongly differ depending on the field region.

In near-field or nonradiative region, the oscillating electric and magnetic fields are separate [6] and power can be transferred via electric fields (\vec{E}) by capacitive coupling (electrostatic induction) or via magnetic fields (\vec{B}) by inductive coupling (electromagnetic induction) between coils of wire. These fields are not radiative, meaning the energy stays within a short distance of the transmitter and if there is no receiving device within their limited range to couple to, no power leaves the transmitter.

In radiative or far-field region the electric and magnetic fields are perpendicular to each other and propagate as an electromagnetic wave, such as microwaves, radio or light waves. This part of the energy is radiative, meaning it leaves the antenna whether or not there is a receiver to absorb it. The portion of energy which does not strike the receiving antenna is dissipated and lost to the system.

The boundary between the two kinds of transfers is vaguely defined. For transmitters and receivers in diameters shorter than half of the operating wavelength, the near field is the region within a radius of wavelength ($r < \lambda$), while the far-field is the region out of a radius of two wavelengths ($r > 2\lambda$). The middle region between is known as “transition zone”. For transmitters and receivers in diameter larger than a half-wavelength, the near and far field transfers are defined by the Fraunhofer distance [7]:

$$d_f = \frac{2D^2}{\lambda} \quad (1.1)$$

where D is the dimension of the largest antenna of the power transmitter and the receiver, λ is the wavelength of the electromagnetic wave.

There exist other radiative technologies, such as radio or WiFi, which use the same fields and waves as wireless power transmission systems. In this case, the main goal is to transmit information, so the amount of power reaching in the receiver is unimportant as long as it is enough to achieve a reasonable signal to noise ratio, making the message intelligible.

1.5 Discussion

In radiative techniques \vec{E} and \vec{B} field strength decreases with distance from the source as $1/r^2$ for the radiated power intensity of electromagnetic radiation. However, near-field \vec{E} and \vec{B} strength decreases more rapidly with distance, being proportional to $1/r^3$. We could

think this can be a bother when transferring power. And that is true, but this effect is mostly notable when transmitting over long-distance, which is not the priority of the project. This advantage of far-field over near-field techniques lies on the capability to focus electromagnetic radiation by reflection or refraction into beams. To achieve this narrow beams are necessary antennas much larger than the wavelength of the waves, corresponding to frequencies above 1 GHz, in the microwave range or above. Far-field techniques were rapidly refused because of the physical constraints of the transmitter antenna size, discussed on section [2.6.5.5](#).

Seeing all the available technologies scope inside non-radiative techniques it is quite reasonable to guide towards Resonant Magnetic Induction. This power transfer is reminiscent of the usual magnetic induction; however, the usual non-resonant induction is very inefficient for midrange applications which compromise distances from one antenna diameter up to ten times the antenna diameter [\[8\]](#). As opposed to directed electromagnetic radiation, such as lasers, it does not need an uninterrupted line of sight between the source and the device, as well as a sophisticated tracking mechanism when the device changes its position.

In addition, the fact that magnetic fields interact so weakly with biological organisms is also important for safety considerations [\[9\]](#). Capacitive coupling was rejected because of safety issues related to the necessity of a high source voltage.

To summarize, Resonant Magnetic Induction was the unique WPT system which met mostly all requirements. It allows us to transfer power, nearly omni-directional, over midrange distances in an efficient way. Furthermore, this WPT system is irrespective of the geometry of the surrounding space, with low interference and losses into environmental objects. It also accomplishes the first and one of the most important proposal in this work; to design a small wireless transfer system capable to be carried in a nano-quadcopter.

WPT system	Frequency	Directivity	Range	Efficiency
Capacitive Coupling	Low Hz~MHz	Weak	Short	High
Inductive Coupling	Low Hz~MHz	Weak	Short	High
Propagating Electromagnetic	Medium MHz~GHz	Medium	Medium	Medium
Microwave	High GHz~THz	Strong	Long	Low
Photo-electricity	High >THz	Strong	Long	Low

Table 1.1: A comparison among the wireless power transfers

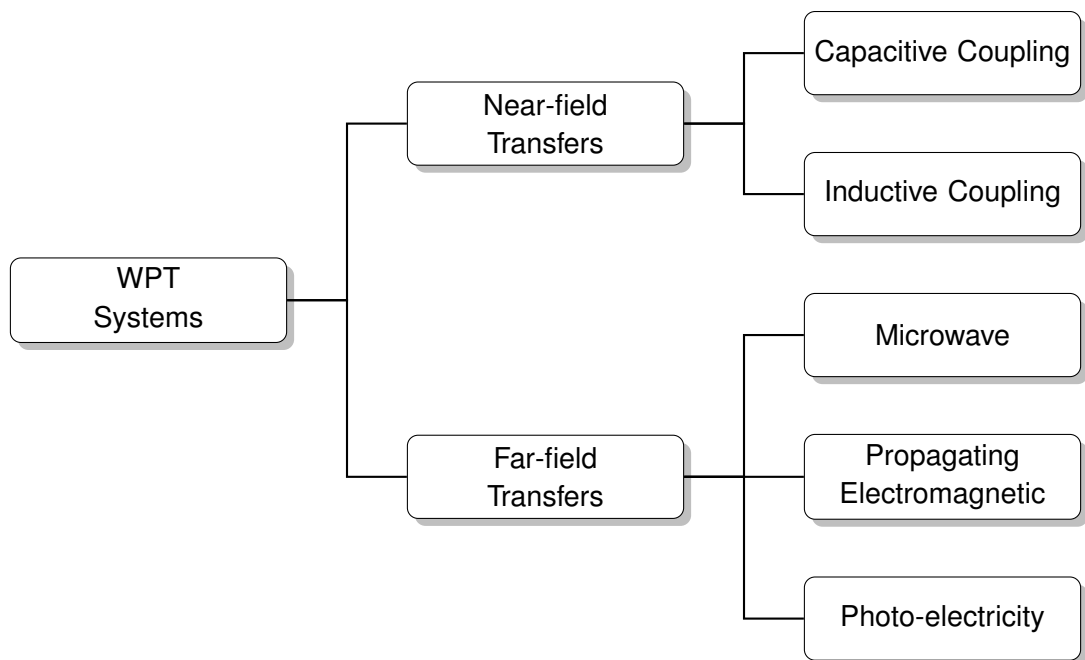


Figure 1.1: Types of wireless power transfer inside the EM spectrum

CHAPTER 2. MODELING MAGNETIC INDUCTION SYSTEM

A model is probably the most important part when designing a system. Therefore, the system modeling has been studied in detail in order to reproduce reality as close as possible. It is a great advantage to have a reliable model which can reproduce system's behaviour for any conditions. The model will provide us not only with the characterization of the power coils, but also will forecast the operating system constraints.

2.1 Magnetic Field

The magnetic field can be produced as consequence of a point charge q moving at a velocity \vec{v} in the space or when a current I is flowing through a length element $d\vec{l}$. The moving point charge $q\vec{v}$ and the current element $Id\vec{l}$ are named sources of the magnetic field. The most suitable source to determine the magnetic field due to a current loop is an infinitesimal current element. In this case, the expression to compute the magnetic field at a distance r is called Biot-Savart law:

$$d\vec{B} = \frac{\mu_0}{4\pi} \frac{Id\vec{l} \times \hat{r}}{r^2} \quad (2.1)$$

where μ_0 is a constant of proportionality named the magnetic constant (permeability in free space) and has the exact value of $4\pi \cdot 10^{-7} \text{ T}\cdot\text{m/A}$.

Imagine that a current flows through a circular loop of radius R made of a conductive material. The magnitude of the magnetic field at a point on the axis of this loop can be determined using the Biot-Savart law. As figure 2.1 shows, the generated magnetic field is perpendicular to \hat{r} and also to $Id\vec{l}$ and follows the expression below:

$$|d\vec{B}| = \frac{\mu_0}{4\pi} \frac{Id\vec{l}}{(z^2 + R^2)}$$

where in comparison to the Biot-Savart law, $r^2 = z^2 + R^2$ and the vectorial product $|d\vec{l} \times \hat{r}|$ is equal dl because $d\vec{l}$ is perpendicular to \hat{r} .

When we sum around all the current elements in the loop, the components of $d\vec{B}$ perpendicular to the axis of the loop sum to zero, which leave only the component dB_z that is parallel to the axis [10]. By developing the equation, dB_z can be expressed as:

$$dB_z = \frac{\mu_0}{4\pi} \frac{Idl}{(z^2 + R^2)} \sin\theta = \frac{\mu_0}{4\pi} \frac{Idl}{(z^2 + R^2)} \frac{R}{\sqrt{z^2 + R^2}} = \frac{\mu_0}{4\pi} \frac{RIdl}{(z^2 + R^2)^{3/2}}$$

$$B_z = \oint dB_z = \frac{\mu_0}{4\pi} \frac{RI}{(z^2 + R^2)^{3/2}} \oint dl$$

In the case of a circular coil, the integral of dl around a loop is $2\pi R$ and taking into account that the coil has N turns, the magnetic field on z axis can be computed as follows:

$$B_z = \frac{\mu_0}{2} \frac{NR^2 I}{(z^2 + R^2)^{3/2}} \quad (2.2)$$

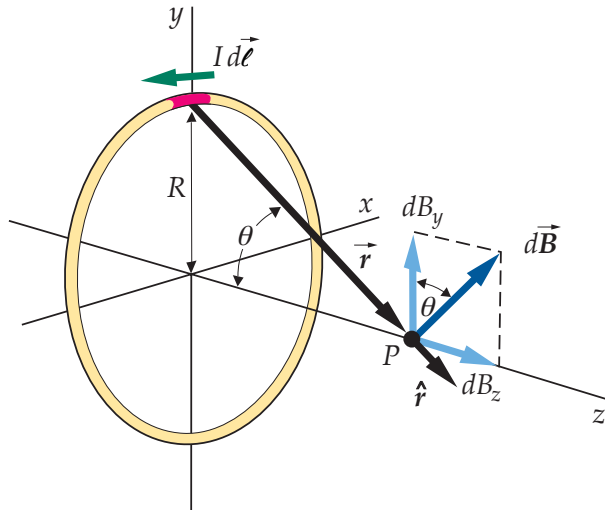


Figure 2.1: Geometry for calculating the magnetic field at a point on the z axis

2.2 Magnetic Induction

In the early 1930s Michael Faraday and Joseph Henry independently discovered that in a changing magnetic field a changing magnetic flux through a surface bounded by a closed stationary loop of wire induces a current in the wire [1.3](#). This current is also found in a static magnetic field when a changing magnetic flux is created by a moving loop of wire through the surface bounded by the wire itself.

2.2.1 Magnetic Flux

The magnetic flux through a surface is the surface integral of the normal component of the magnetic field \vec{B} passing through that surface. In our case these surfaces are defined as the transmitter and receiver coils. As \vec{B} is proportional to the number of field lines per unit area, the magnetic flux is proportional to the number of field lines through an element area [\[10\]](#). Since the coil surface is flat and has a constant area A and several turns N , if we assume \vec{B} is uniform in magnitude and direction everywhere on the surface, the magnetic flux through the coil surface is:

$$\phi_m = \vec{B} \cdot \hat{n}A = NBA \cos\theta \quad (2.3)$$

Where θ is the angle between the direction of \vec{B} and the direction of the unit vector normal to the coil surface \hat{n} .

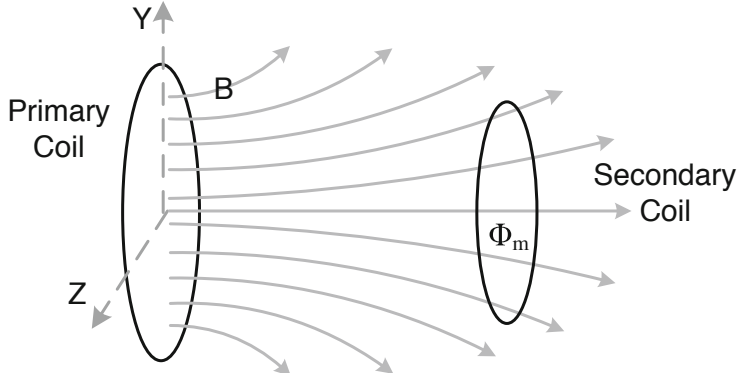


Figure 2.2: Magnetic field lines from transmitter to receiver coil

2.2.2 Induced EMF and Faraday's Law

Equation 2.3 shows that flux can be changed by increasing or decreasing B , by increasing or decreasing A , or by changing the angle θ . The idea of changing A or θ is really difficult to achieve and implement compared to changing B . Given the magnetic field created by the coil is due to a current in the transmission circuit, the magnitude of the magnetic field can be increased or decreased by increasing or decreasing the current. This change of current will be obtained by using alternating current (AC). The result of this variation of magnetic flux is an emf ε induced along the path that is equal in magnitude to the rate of change of the magnetic flux through the surface. This is known as Faraday's law:

$$\varepsilon = -\frac{d\Phi_m}{dt} \quad (2.4)$$

According to the Faraday's law, the polarity of the induced magnetic field is such that it produces a magnetic field opposes the change which produces it. Because the induced voltage and the current are produced at the secondary side, power is successfully transferred from the primary to the secondary side. This is the basic working principles of the inductive coupling.

2.2.3 Inductance

The simplest way to define what the inductance means is that it is like a resistance but in AC current. It is an opposition to the rate of change of the current. The unit of inductance is the henry (H). As it is shown at follows, one henry is the amount of inductance required to generate one volt when the current is changing at the rate of one ampere per second.

$$V_L = L \frac{dI}{dt} \quad (2.5)$$

So it is correct to say that the inductance behaves like a resistance (in AC) because the larger inductance the bigger induced voltage keeping the rate of change of current constant.

In this project are used two types of inductances: the first one, to generate the magnetic flux in one coil, called self-inductance; and the second one, to relate the amount of magnetic flux given by one coil to another coil when they are close enough.

2.2.3.1 Self Inductance

In this section, the definition of the self-inductance is related to the magnetic field. The reason is because if it is considered a current I going through a coil, this coil generates a magnetic field B that is proportional to I [10]. The magnetic flux generated by B is also proportional to I , as it has expressed in equation 2.6:

$$\phi_m = L \cdot I \quad (2.6)$$

As shown in the previous equation, the inductance L is the proportionality constant and it is called self-inductance. The SI unit of the self-inductance is the henry, as it has said above, and one henry corresponds to one tesla times square meter per ampere.

$$1 \text{ H} = 1 \text{ T} \cdot \text{m}^2/\text{A} = 1 \text{ Wb/A}$$

One possible way to compute the self-inductance of a coil is by calculating, due a knowing current, the magnetic field at every point on the surface bounded by the coil, computing the generated magnetic flux and isolate the self-inductance from the equation 2.6 [10]. But the computing of the magnetic field at every point is not a trivial task. Thus, there exist many formulas to easily compute the self-inductance of many types of coils depending on its structure or its geometrical shape, like long solenoids, ferrite-core, air-core and toroid-core inductor, etc. For example, the self-inductance of a long, tightly wound solenoid can be determined by substituting the magnetic flux by the formulas obtained in the electromagnetism theory:

$$\phi_m = NBA = \frac{\mu_0 N^2 IA}{h} \quad (2.7)$$

where N is the number of turns, and A and h are the coil area and height respectively. If the current flowing through a coil divides the magnetic flux, there is obtained the self-inductance of a long solenoid.

$$L = \frac{\phi_m}{I} = \frac{\mu_0 N^2 A}{h} \quad (2.8)$$

These formulas have the characteristic that the value of the coil only depends on the geometrical shape of the coil. Note that these formulas only depend on the geometrical shape of the coil.

2.2.3.2 Mutual inductance

Imagine that two or more circuits are close to each other. The amount of magnetic flux through one circuit to the other ones is proportional to the current generated in the first circuit, like the magnetic flux generated by one coil, as we can see in equation 2.6. The difference is that the proportionality constant is not the self inductance but also is the mutual inductance.

To obtain an expression of the mutual inductance, it is necessary to know the expression of the magnetic field at a distance z . In section 2.1 it has been determined the equation of computing the magnetic field due to a current loop. This expression can be used for a coil when it is multiplied by N turns.

Once we have determined the expression of the magnetic field, and considering that two coils are close to each other at a distance z , we can obtain an expression of the magnetic flux through the primary coil to the secondary one (equation 2.9). We will use a similar equation (2.3) to determine this flux. To simplify the calculations, we are considering that the magnetic flux goes through the perpendicular direction to the area of the primary coil, thus, the value of $\cos \theta$ becomes one.

$$\phi_{m12} = M I_1 = N_2 B_1 A_2 \quad (2.9)$$

Note that the mutual inductance M is the proportionality constant of the magnetic flux, as it has said above. The equation 2.2 must be substituted to the equation 2.9 and isolate the mutual inductance.

$$M = \frac{\mu_0}{2} \frac{R_1^2 N_1 I_1}{(z^2 + R_1^2)^{3/2}} \frac{N_2 A_2}{I_1}$$

$$M = \frac{\mu_0}{2} \frac{N_1 N_2 R_1^2 R_2^2 \pi}{(z^2 + R_1^2)^{3/2}} \quad (2.10)$$

As it shows the previous equation, at great distances from the coil, $|z|$ is much greater than R_1 and the mutual inductance varies inversely proportional to the distance cubed. This is important to be taken into account because the magnetic flux given by a primary coil to a secondary coil is proportional to the mutual inductance and it will drop rapidly if the distance increases. The conclusion of this is that the closer link distance, the more energy transferred to a secondary coil and a better coupling will be.

2.3 Resonance

The resonant circuit, also called LC circuit, can store electrical energy whether it oscillates at its natural frequency (2.11). The circuit is composed by a coil inductance and a capacitor. The capacitor stores energy in the electric field E between its plates, depending on the voltage across it, and an inductor stores energy in its magnetic field B , depending on the current through it.

2.3.1 Energy Pendulum

Capacitors and inductors are flip-sides of the same reactive coin, storing and releasing energy in complementary modes. If either the capacitor or inductor starts out in a charged state, by connecting momentarily a battery or by approaching a magnet, the two components will begin to exchange energy between them, back and forth, creating their own AC voltage.

Frequently, resonance effect is explained using the pendulum analogy comparing the change in kinetic and potential energy to the variation of voltage and current inside the circuit. The pendulum swings at a certain frequency depending on the length of the string holding the mass and not on the mass suspended. In physics, this kind of sine-wave oscillation for a mechanical system is called *Simple Harmonic Motion (SHM)*. The same occurs

in the LC circuit where the oscillation and so the frequency are strictly dependent on the sizes of the capacitor and inductor.

$$\omega_0 = \sqrt{\frac{g}{L}} \quad \omega_0 = \frac{1}{\sqrt{LC}} \quad (2.11)$$

If the power supply frequency for a circuit exactly matches the natural frequency of the circuit's LC combination (Equation 2.11), the circuit is said to be in a state of resonance.

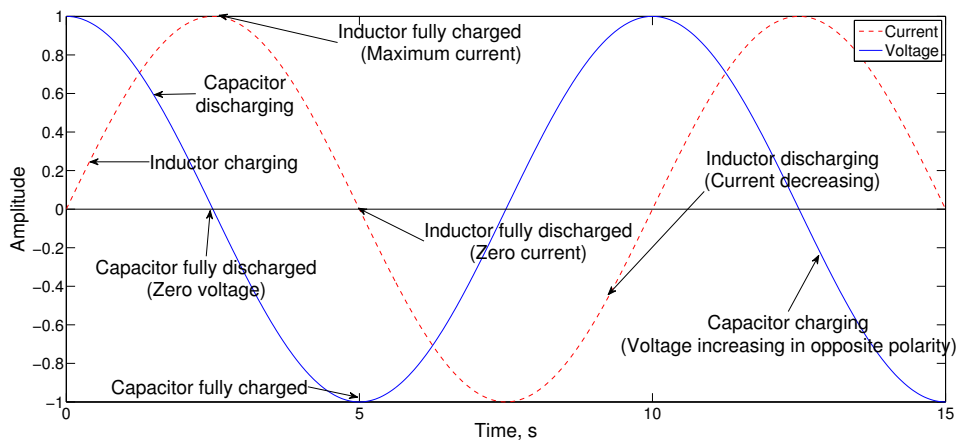


Figure 2.3: Voltage and current behaviour inside a LC circuit

It can be noticed that there is a phase shift of 90° over time between voltage and current measurement in the LC circuit of Figure 2.3. This fact will be discussed later. In the same way, whether position and velocity traces of the pendulum were drawn, the same phase shift will be observed.

Both the mechanical and electrical circuits once they have began to oscillate do not last forever. Either resistive or friction losses are the responsible of a finite lifetime.

The pendulum analogy is totally valid for explaining all kind of resonances (e.g., acoustic, mechanical, electromagnetic, etc.) but not enough clear for understanding the resonance between two magnetically coupled resonators. For the purpose of understanding better the behaviour of a coupled system, we think it would be useful to quote the following analogy from F. Hadley¹:

"Imagine a room with 100 identical wine glasses, each filled with wine up to a different level, so they all have different resonant frequencies. If an opera singer sings a sufficiently loud single note inside the room, a glass of the corresponding frequency might accumulate sufficient energy to even explode, while not influencing the other glasses. In any system of coupled resonators there often exists a so-called "strongly coupled" regime of operation. If one ensures to operate in that regime in a given system, the energy transfer can be very efficient."

In our case, the transmitter coil instead of irradiating the environment with electromagnetic waves, it fills the space around it with a non-radiative magnetic field oscillating at a fixed

¹Franklin Hadley is a Professor with Tenure in the Department of Mechanical Engineering and Materials Science in Duke University.

frequency. The non-radiative field mediates the power exchange with the receiver coil, which is specially designed to resonate with the field. The nature of the process ensures a strong interaction between the coils, while minimizing the interaction with the rest of objects [9].

The use of resonance results in a much higher efficiency compared to non-resonant inductors, such as typical transformers which require very short range. In addition, by working at the resonant frequency the circuit can achieve its maximum amplitude.

2.3.2 Series Resonance

In order to analyse both series and parallel resonance, a resistance has been added to avoid infinity currents and zero voltage values. These RLC circuits will provide a first approach for understanding the differences when designing the resonant circuit.

As it is said before, resonance occurs when a series resonant circuit is driven from an external source at a frequency ω_0 at which the inductive and capacitive reactances are equal in magnitude.

$$X_L = X_C$$

This cancellation leaves only the resistance² to contribute to the impedance,

$$Z_{min} = \sqrt{R^2 + (X_L - X_C)^2} = R$$

The impedance is also at a minimum at resonance (see Figure 2.5(a)). Below that natural frequency, called resonant frequency ω_{res} , the series resonant circuit looks capacitive since the impedance of the capacitor increases while inductive reactance is decreasing. Above resonance the circuit behaves oppositely.

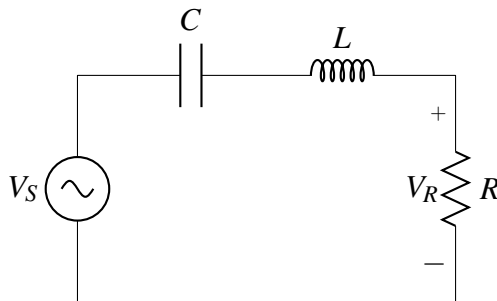


Figure 2.4: Series resonance

At resonance frequency, due to the smallest circuit impedance, the current is greatest,

$$I_{max} = \frac{V}{Z_{min}} \quad (2.12)$$

Thus, resonant current peak is set by the resistor value.

²An LC circuit is an idealized model since it assumes there is no dissipation of energy due to resistance.

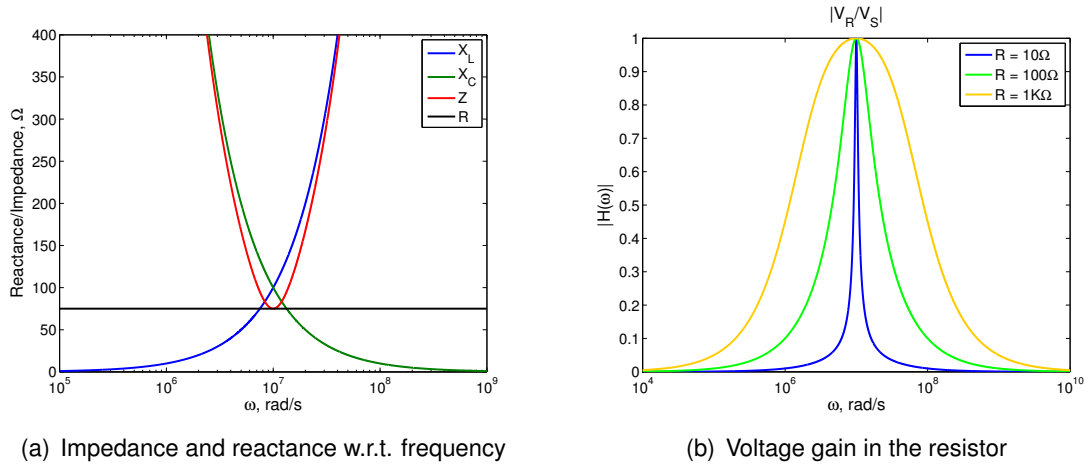


Figure 2.5: Series RLC circuit

2.3.3 Parallel Resonance

In the same way as series resonance, the parallel resonant circuit is purely resistive at ω_{res} , where $X_L = X_C$.

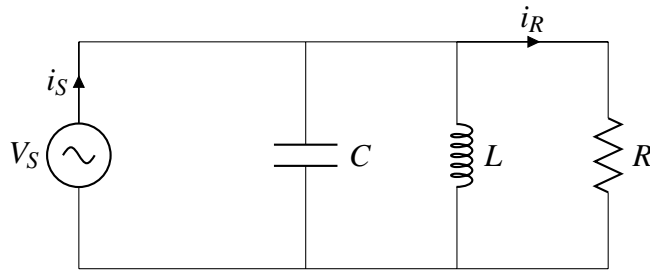


Figure 2.6: Parallel resonance

This time the parallel RLC circuit has a current gain rather than a voltage gain. Its impedance is maximized at the resonant frequency rather than minimized.

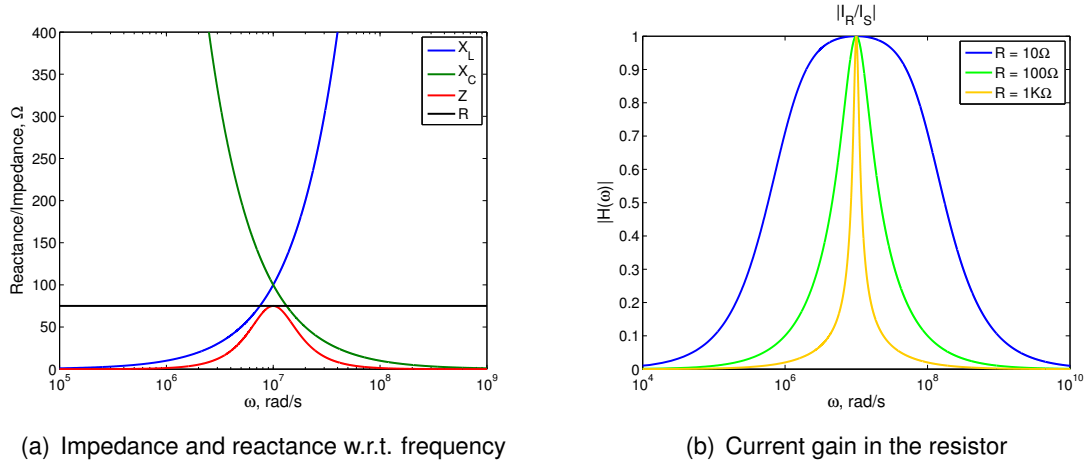
Below this frequency, the resonant circuit looks inductive since the impedance of the inductor is lower. Above resonance, the capacitive reactance decreases. In both cases the current drawn is larger than the current at resonance case [11]. In both parallel and series circuits, the resonant frequency remains the same.

Figure 2.7(a) shows how impedance is at a peak at resonant frequency and therefore voltage is maximum. The reason for this is that voltage is proportional to impedance.

$$V = I \cdot Z \quad (2.13)$$

2.4 Characterizing the Inductor

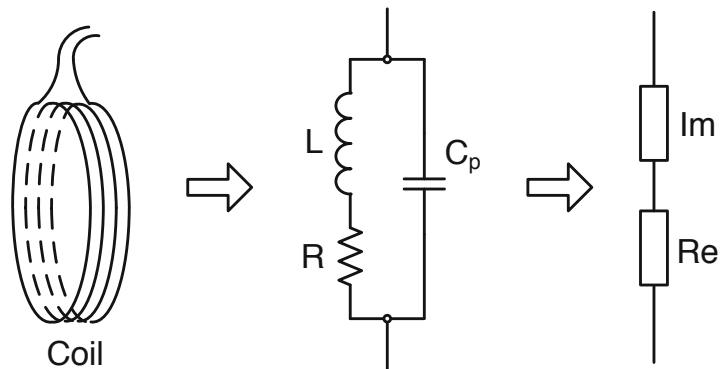
In order to transfer power wirelessly, the LC-pair is adopted because it is the oldest and most frequently used technique. It is rapidly assembled by winding a *piece* of wire and

**Figure 2.7:** Parallel RLC circuit

placing a capacitor either in series or parallel, depending on the desire effect. The capacitor is adopted at both side to keep the coils resonate at the designed frequency.

There are many ways to model a coil. Figure 2.8 shows one of them, composed by the coil inductance L itself and a coil conductor resistor R . This resistance is placed to quantify *Copper loss* or winding loss which is the term used to describe the energy dissipated by resistance in the wire used to wind the coil [12]. There is also an equivalent parasitic capacitor C_p connected to the inductor and resistor. This parasitic capacitance is due to the fact that the inductor is made out of a coil of insulated wire. Therefore, tiny capacitors are created between the windings since there are two sections of wire separated by an insulator.

Another simplified equivalent circuit is shown on the right in Figure 2.8. The impedance of the coil is represented by a real impedance component Re and an imaginary impedance component Im (impedance equations are presented in Appendix A.2). This modeling approach has been verified, especially in the low frequency range [5]. For high-accuracy applications, like PCB spiral coils, complex models [13] can be used.

**Figure 2.8:** Modeling of a single magnetic coil

2.4.1 Coil Resistance

The calculation of the resistance of a coil is important because it limits the power transferred in a WPT system. If the resistances of a coil were zero, the power transfer efficiency would be 100%, and there would not exist any limitation to transfer energy at a given distance. However, the ideal world does not exist and appear resistances that generate heat due to Joule effect: power losses. The goal of a WPT system is to minimize this power losses to ensure the maximum transferred power and efficiency.

2.4.1.1 DC Resistance

At low frequencies ($f < 200$ kHz) [3] the resistance experiments a DC behavior. The value of this resistance does only depend on the wire geometry and material. The DC resistance of a metal conductor is given by [5]

$$R_{DC} = \rho \frac{l}{S} \quad (2.14)$$

where l is the wire length in meters, S is the wire section in square meters and ρ is the electrical resistivity of the metal material, measured in $\Omega \cdot m$. In table 2.4 are exposed different electrical resistivities for some metal conductors.

2.4.1.2 AC Resistance

When the frequency increases up to 200 kHz we can not talk anymore about DC resistance, the reason is the appearance of some effects that increase the wire resistance with the frequency. From now on, the resistance will behave as an AC resistance due to the *skin-effect* and *proximity-effect*.

Skin-effect happens in all wire and cable. When the signal is DC, it uses the entire conductor, with the same amount of current flowing in the center of the wire as on the outside. As the frequency is increased, the current density begins to move further away from the conductor that inside it. Consequently, the equivalent cross section of the conductor decreases and as Figure 2.9 shows, the wire resistance is increased with frequency. To quantify the *skin-effect* it is introduced the skin depth δ . Skin depth is a measure of how far electrical conduction takes place in a conductor, and is a function of frequency, no matter how thick the wire is. It is calculated as described below [14],

$$\delta = \frac{1}{\sqrt{\pi f \mu \sigma}} \quad (2.15)$$

where σ is the electrical conductivity of the wire material ($\sigma_{copper} = 5.8 \times 10^7$ S/m), f is frequency in Hz and μ is the total permeability defined as the permeability in free space times the material permeability ($\mu = \mu_0 \cdot \mu_m$).

Owing to skin depth decreases with respect to the frequency as a negative exponential, conductors can become thinner at higher frequencies with little impact on circuit loss, because skin depth shrinks with frequency. A rule of thumb is always plan on providing at

least five skin depths of low-loss conductor in order to provide good performance without the need of invest better conductors [15]. This effect can be reduced by using *Litz wire* [16].

The resistance corresponding to *skin-effect* can be determined in the following way:

$$R_{skin} = R_{DC} \frac{4d}{\delta} \quad (2.16)$$

The R_{skin} is the result of multiplying the R_{DC} by the coefficient $4d/\delta$, which is proportional to the square root of the frequency.

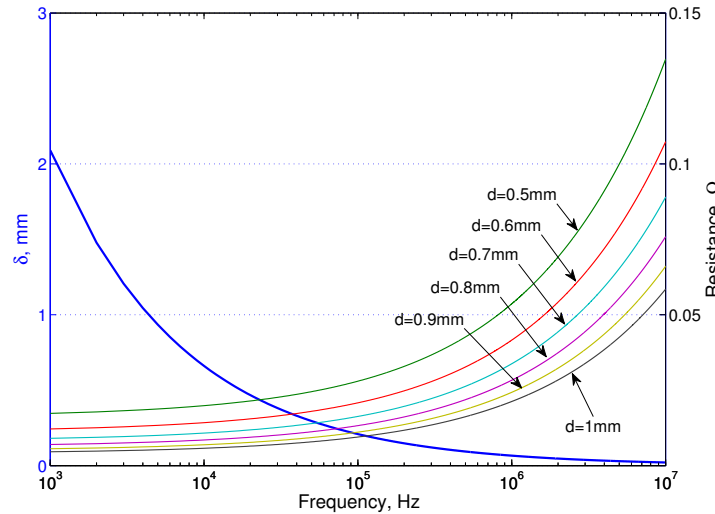


Figure 2.9: Skin depth and resistance varying frequency for a fixed coil

Besides the *skin-effect* there is another phenomena that increase the resistance value of a conductor when is applied an alternating current, called *proximity-effect*. This effect is the apparent increase in the resistance of the wire due to the circulating current in the conductor caused by the alternating flux of the other nearby conductors. As a result, more power losses in the windings appear. To quantify the *proximity-effect*, there is used the Dowell's assumption [16]:

$$R_{proximity} = R_{DC} \Psi \left[\frac{\sinh(2\Psi) + \sin(2\Psi)}{\cosh(2\Psi) - \cos(2\Psi)} + \frac{2}{3}(m^2 - 1) \frac{\sinh(2\Psi) - \sin(2\Psi)}{\cosh(2\Psi) + \cos(2\Psi)} \right] \quad (2.17)$$

In the above equation, the parameter Ψ can be determined in the following form:

$$\Psi = \left(\frac{100d}{2\delta} \right) \sqrt{\pi}$$

Here, m indicates the number of layers, and δ is the skin depth previously mentioned.

To conclude this section, the total equivalent series resistance R_{ES} that appears when an alternating current flows through a wire is the sum of all these effects in addition to the "parasitic" resistance of the wire, called DC resistance.

$$R_{ES} = R_{DC} + R_{skin} + R_{proximity} \quad (2.18)$$

2.4.2 Coil Inductance

In this project air-core inductors are required due their low weight compared to solid-core, despite the last provide better coupling. The reason of avoiding better *transformers*, as it said in previous sections, is that the primary coil is wanted to go on a nano-quadcopter. Thus, the most typical formulas to compute the self-inductance of an air-core inductor are exposed below.

The most typical formula that is used in many projects or studies is the equation of a circular loop coil [17], [18], [19]:

$$L = \mu_0 R N^2 \left(\ln \frac{8R}{d/2} - 1.75 \right) \quad [\text{H}] \quad (2.19)$$

where d is the wire diameter.

Another equation is the Harold A. Wheeler's formula to compute the inductance for a finite-length solenoid:

$$L = \frac{N^2 R^2}{9R + 10h} \quad [\mu\text{H}] \quad (2.20)$$

The units of length are expressed in inches. This formula is correct to within 1 per cent for coils with $h > 0.8R$ [20].

Similar to the Harold A. Wheeler's formula, an equation for air-cored inductor is exposed below [21]:

$$L = 2KRN^2 \quad [\mu\text{H}] \quad (2.21)$$

where K is a parameter that depends on the dimension ratio (D/h) of the coil, whose values are listed in Appendix A and the units of length in this equation are expressed in centimeters.

2.4.3 Coil Parasitic Capacitor

Every coil has a parasitic capacitor. Since the inductor is made out of a coil of insulated wire, tiny capacitors between the windings are created. This is due each section of windings is at a slightly different potential because of wire inductance and resistance. When the current frequency is high enough, most current in the coil would be bypassed via the parasitic capacitor [5]. As a result, the coil can not be viewed as a lumped inductor anymore. The coil's inductance would resonate with the parasitic capacitor at a frequency. This frequency is called the self-resonant frequency (f_s).

$$f_s = \frac{1}{2\pi\sqrt{LC_{par}}} \quad (2.22)$$

The parasitic capacitance is connected in parallel to the inductor and the resistor. Its value is relatively small, of the order of 1 pF, which is insignificant at low frequencies but not at very high frequencies (> 5 MHz) [22]. Because of this capacitance, the coil has a self-resonance frequency between 10 MHz and 25 MHz.

The parasitic capacitance effect can be alleviated by keeping inductor windings far apart, and so reducing the capacitance by using helical coils. The second option to reduce parasitic capacitors is to work at a frequency low enough. This frequency will be discussed in Section 2.6.4. For the following theoretical model parasitic capacitors will be disregarded.

2.5 Coreless Transformer Modeling

In this section the electrical model of the resonant magnetic induction system will be determined by using the air coreless transformers theory, in which WPT systems are based on. It is called transformer because it transforms electrical energy into magnetic energy, then back into electrical energy again. Because its operation depends on electromagnetic induction between two stationary coils and a magnetic flux and polarity, transformers are necessarily AC devices.

Parameter	Definition
V_S	Source voltage
I_1	Primary current
I_2	Secondary current
R_1	Primary resistance
R_2	Secondary resistance
R_L	Load resistance
L_1	Primary inductance
L_2	Secondary inductance
C_1	Primary capacitor
C_2	Secondary capacitor
M	Mutual inductance
ω	Angular frequency

Table 2.1: Electric parameters

2.5.1 Electrical Circuit

In the first analysis, the electric system of non-resonant induction is discussed in a generic way. A typical inductive system consists of a primary transmitter coil (Tx) and a secondary receiver coil (Rx), but there can be added more coils to the system.

The Tx coil is characterized by a winding that has a resistance R_1 and an inductance L_1 . Similarly, the secondary coil Rx is characterized by a winding resistance, R_2 and an inductance, L_2 .

As it can be seen in Figure 2.10, the system does not include compensation capacitors neither in the transmission side nor the reception. Thus, a non-resonant³ is studied on a first approach. The system is excited by a perfect sine wave in steady state condition. For simplicity, the lumped element model is assumed regarding that λ is much bigger than the

³Note this is stated for ideal coils which need of a compensation to become resonant.

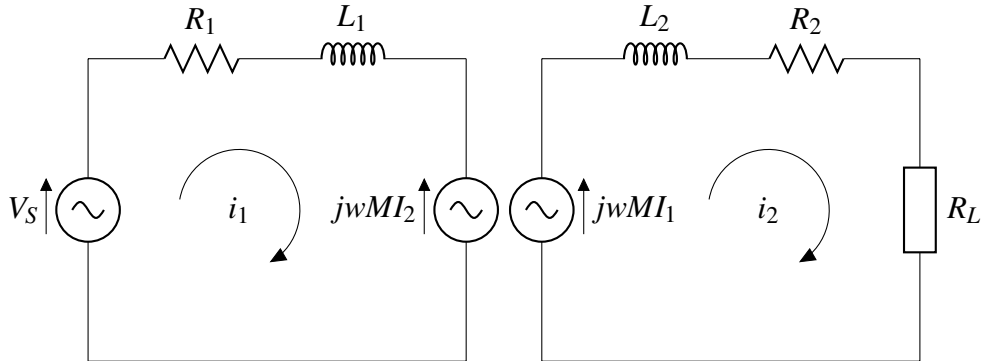


Figure 2.10: General electric circuit

characteristic length of the circuit. This assumption declares that all circuit elements, such as resistors, inductors and capacitors, are concentrated into idealized electrical components.

The circuit model offers a convenient way to systematically analyze the characteristic of the system [23]. By applying circuit theory Kirchhoff's Voltage Law (KVL) to this system a relationship between currents through each coil and the voltage applied to the transmitter coil can be described as the following equation system:

$$\left\{ \begin{array}{l} V_S = R_1 \cdot I_1 + j\omega L_1 \cdot I_1 - j\omega M \cdot I_2 \\ 0 = R_2 \cdot I_2 + R_L \cdot I_2 + j\omega L_2 \cdot I_2 - j\omega M \cdot I_1 \end{array} \right. \quad (2.23)$$

$$\left\{ \begin{array}{l} V_S = R_1 \cdot I_1 + j\omega L_1 \cdot I_1 - j\omega M \cdot I_2 \\ 0 = R_2 \cdot I_2 + R_L \cdot I_2 + j\omega L_2 \cdot I_2 - j\omega M \cdot I_1 \end{array} \right. \quad (2.24)$$

These equations show how the primary side induces voltage into the secondary side which depends on the frequency, mutual inductance and the primary coil's current, which is also called magnetizing current since it is the responsible of generating the magnetic field and so the magnetic flux.

The system of linear equations can be arranged as the following symmetric matrix 2.25.

$$\begin{bmatrix} V_S \\ 0 \end{bmatrix} = \begin{bmatrix} Z_1 & -j\omega M \\ -j\omega M & Z_2 \end{bmatrix} \begin{bmatrix} I_1 \\ I_2 \end{bmatrix} \quad (2.25)$$

In order to transfer the maximum power and reduce losses the proposed model is based on [3], which defines an equivalent impedance matching method. The procedure analyses the effect of the complete secondary circuit on the primary side. Thus, the secondary circuit is viewed from the voltage supply as a reflected impedance Z_R .

Firstly, the secondary current will be isolated from the Equation 2.24, becoming:

$$I_2 = \frac{j\omega M}{R_2 + R_L + j\omega L_2} \cdot I_1 \quad (2.26)$$

To determine the expression of Z_R , all the secondary-side components, including the load resistance R_L , can be gathered into a single impedance expresion called secondary impedance Z_2 :

$$Z_2 = R_2 + R_L + j\omega L_2 \quad (2.27)$$

In the same way, the primary circuit impedance is defined in the next manner:

$$Z_1 = R_1 + j\omega L_1 \quad (2.28)$$

Now, the current at secondary circuit can be expressed as:

$$I_2 = \frac{j\omega M}{Z_2} \cdot I_1 \quad (2.29)$$

Substituting I_2 in Equation 2.24, we are forcing voltage source to “see” secondary circuit as a single impedance, Z_R .

$$V_S = Z_1 \cdot I_1 + \frac{\omega^2 M^2}{Z_2} \cdot I_1 \quad (2.30)$$

where Z_R is defined as:

$$Z_R = \frac{\omega^2 M^2}{Z_2} \quad (2.31)$$

Thereby, equation 2.30 is rearranged in the form:

$$V_S = (Z_1 + Z_R) \cdot I_1 \quad (2.32)$$

To simplify even more the expression, it is possible to define the whole circuit as the following single impedance (see Figure 2.12):

$$V_S = Z_{eq} \cdot I_1 \quad (2.33)$$

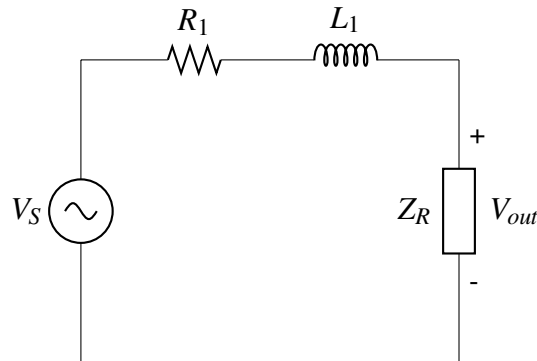


Figure 2.11: Reflected impedance circuit schematic

Once the Z_R is determined, it is possible to calculate the voltage drop across it by using the voltage divider expression:

$$V_{out} = V_S \cdot \frac{Z_R}{Z_R + Z_1} \quad (2.34)$$

Hence, the power transferred to the reflected impedance is given by:

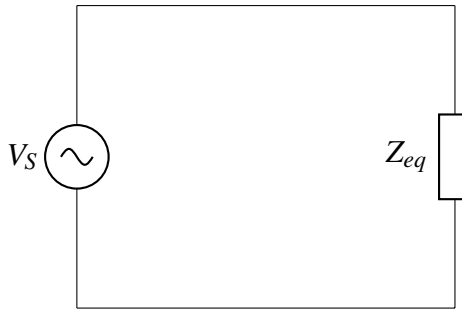


Figure 2.12: Equivalent impedance circuit schematic

$$P_{out} = \frac{V_{out}^2}{Z_R} \quad (2.35)$$

Replacing V_{out} for the expression 2.34, the power at the reflected impedance only depends on the source voltage (also called V_{in}).

$$P_{out} = V_{in}^2 \cdot \frac{Z_R}{(Z_1 + Z_R)^2} \quad (2.36)$$

For the fixed value of Z_1 , it is found the optimal Z_R value computing the partial derivative of P_{out} with respect to Z_L .

$$P_{out_{max}} \Rightarrow \frac{dP_{out}}{dZ_R} = \frac{(Z_1 + Z_R)^2 - 2 \cdot Z_R \cdot (Z_1 + Z_R)}{(Z_1 + Z_R)^4} = 0 \quad (2.37)$$

It is found that the maximum power transfer occurs when $Z_R = Z_1$. This results in a restrictive parameter since Z_R depends on the mutual inductance which in turn depends on the distance between the transmitter and receiver coil. Thus, there is no a unique optimal value of Z_R .

In order to discuss the air-core transformer, the general non-resonant system has been introduced. This system has an important energetic drawback. Secondary coil impedance is used to be high. Hence, it is the responsible for a significant current drop in the load resistance 2.29 [3]. Whether the power transferred to the load is intended to be increased, at first sight, the input voltage should be also increased owing to P_{out} is proportional to the square of V_{in} . But this solution is not optimal at all because it requires higher current amplitudes in the primary coil, and therefore greater Joule losses.

In the following section, resonance capacitors will be added to the primary and secondary circuits. They will cancell (or decrease notably) the large reactance of a coil by working at the resonant frequency. These capacitors allow to reduce the current amplitudes and, as a result, to improve the efficiency of the coreless transformer.

2.5.2 Compensation Topologies

As it is said in Section 2.3, the transmitting and receiving coils are designed to operate at the resonant frequency to establish an efficient energy channel for power transfer. This

is done by using compensation capacitors. Here, the four typical resonant configurations are discussed, which are labeled as SS, SP, PS and PP. The first S or P indicates series or parallel for the primary capacitors and the second S or P means the same for the secondary capacitor. Depending on the resonant type, if the primary capacitor is in series, the transmitting coil will be driven by an AC voltage source, and, whether it is in parallel, the transmitting coil will be driven by an AC current source [24].

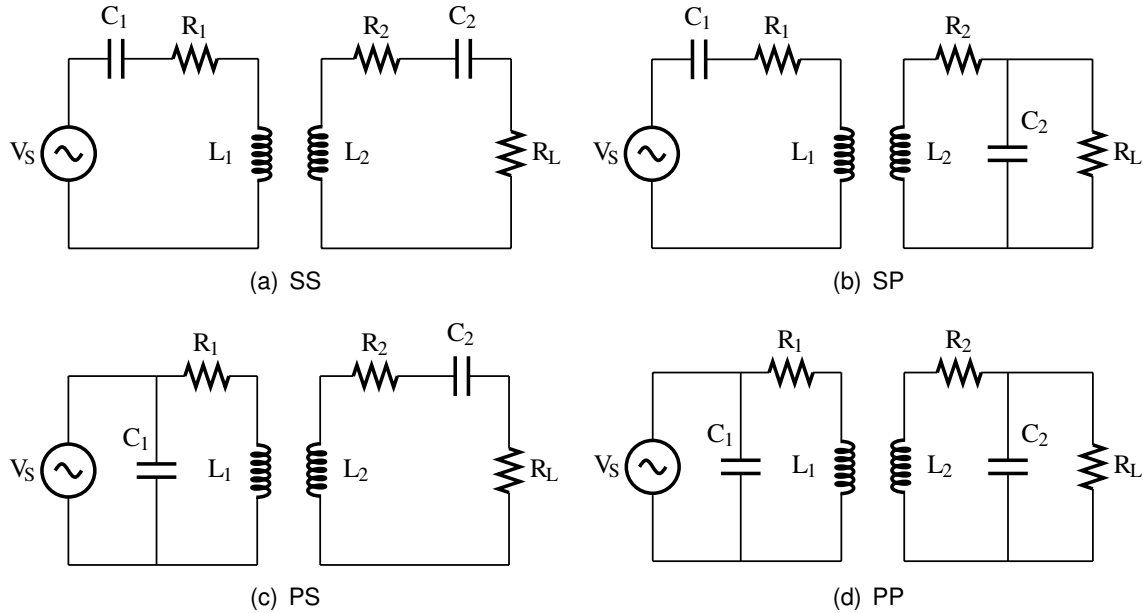


Figure 2.13: Compensation topologies

In this section each topology is evaluated in a detailed way to determine their advantages and drawbacks, and then, to conclude which is the most suitable topology according to our application. Therefore, the equations determined in Section 2.5.1 will be changed due to the insertion of the compensation capacitors, depending on the used topology. This new equations are listed in Appendix B.

Eventually the best topology in terms of maximum transferred power will be chosen. Arbitrary values are selected from the system parameters represented in Table 2.2.

All the calculations for computing the efficiency and the output power (load power) are done using the alternating current basics. Thus, the input power P_{in} and the load power P_L are given by,

$$P_{in} = V_{in} \cdot I_{in} \cdot \cos(\varphi) \quad (2.38)$$

$$P_L = (I_L)^2 \cdot R_L \quad (2.39)$$

where φ is the phase between the input voltage and the primary current. In the previous equations, it is used the root mean square (RMS) for V_{in} , I_{in} and I_L ; as a consequence, the power results are expressed in its average value. Note that P_{in} is multiplied by the power factor $\cos(\varphi)$ which corresponds to compute the active power or consumable power.

Parameter	Value
V_S	5 V
R_S	50 Ω
R_1	0.5 Ω
R_2	0.5 Ω
R_L	50 Ω
L_1	10 μH
L_2	10 μH
C_1	2 nF
C_2	2 nF
M	3 μH

Table 2.2: Arbitrary values of the electric parameters

2.5.2.1 SS topology

The equivalent circuit of the SS topology can be determined by gathering the expression of Z_R with Z_{eq} listed in Appendix B.1 and B.3 respectively. By varying the frequency, the efficiency η and the output power (load power) will show their maximum at the resonance frequency.

In Figure 2.18, when the frequency grows, the efficiency tends to a constant value that depends on the system parameters. This statement does not mean that is optimal to work at high frequencies because the output power drops sharply when the frequency overtakes the resonance frequency. The explanation is that the input power also falls with the same magnitude as the output power.

Another interesting parameter for studying in each topology is the equivalent impedance of the system. This impedance will help us to determine the optimal compensation for our application because its behavior depends on the operating frequency. Figure 2.14 shows that at the resonance frequency, the whole imaginary part of Z_{eq} is canceled and the system impedance is purely resistive. The impedance of this compensation topology behaves as a capacitance since the frequency increases to the resonance frequency; from this point, it will behave as an inductance.

2.5.2.2 SP topology

It is possible to model the SP topology using the formulas obtained for Z_R and Z_{eq} in Appendix B.2 and B.3 respectively. As it is explained in Appendix B.2, to transfer the maximum power to the system load, is recommended to delete the imaginary part of Z_R . This is done by changing the secondary capacitor value to a value that can be computed using the Equation B.7, allowing to transfer only consumable power to the load. As a consequence, the maximum efficiency and load power will be at a different frequency than the resonance frequency of the whole system⁴. The impedance's model has a similar curve as in case of the SS topology impedance as Figure 2.15 shows.

⁴The system resonance frequency in this case will be a trade-off between the resonance frequency of both primary and secondary circuits due to the different capacitance used.

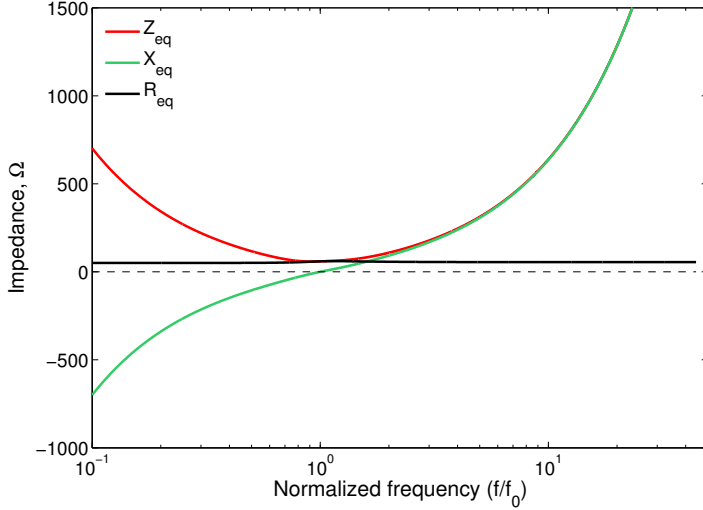


Figure 2.14: Equivalent circuit impedance w.r.t frequency for SS topology

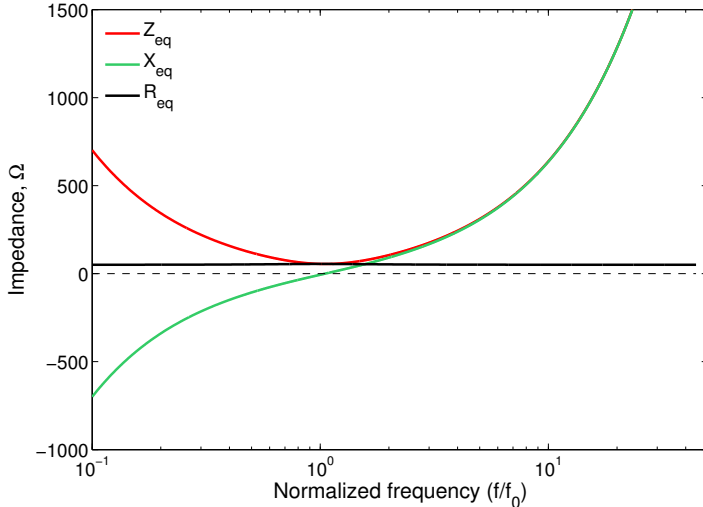


Figure 2.15: Equivalent circuit impedance w.r.t frequency for SP topology

2.5.2.3 PS topology

The SP topology are modeled with the equations for Z_R and Z_{eq} listed in Appendix B.1 and B.4 respectively. A parallel capacitor is generally used to generate large currents in the primary coil [3]. An interesting point for the parallel primary topologies is that the voltage delivered from the source is the same voltage applied to the capacitor.

Note that as in case of the secondary capacitor in parallel, the equivalent impedance of this topology shows a reactance, as it is explained in Appendix B.4. This imaginary part has to be deleted whether is wanted to transfer the maximum power. In this case, the optimal capacitor will be the obtained in Equation B.12. Hence, the system will resonate at a different frequency than the resonance one. This new capacitor has an important dependence on the selected secondary topology because it is inversely proportional to the Z_R .

In this topology, the total impedance shifts from an inductive circuit at low frequencies to a capacitive circuit at high frequencies. At the resonance frequency, the equivalent impedance becomes purely resistive and reaches its maximum value. This is an important fact to be taken into account when going to be used a parallel primary topology, because the power transfer can be maximized only by having a current source input [25]. Nevertheless, in this project is only used a sinusoidal voltage source to drive the system.

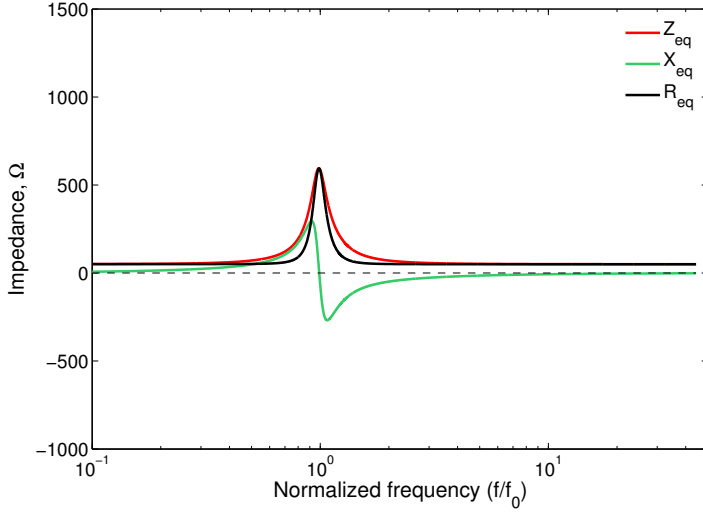


Figure 2.16: Equivalent circuit impedance w.r.t frequency for PS topology

2.5.2.4 PP topology

Finally, the PP topology can be obtained through the equations for Z_R and Z_{eq} listed in Appendix B.2 and B.4 respectively. This topology is well suited to supply a stable secondary load current due to parallel position of the secondary capacitor [3]. In Figure 2.19 this point is verified when the frequency increases from the resonant one.

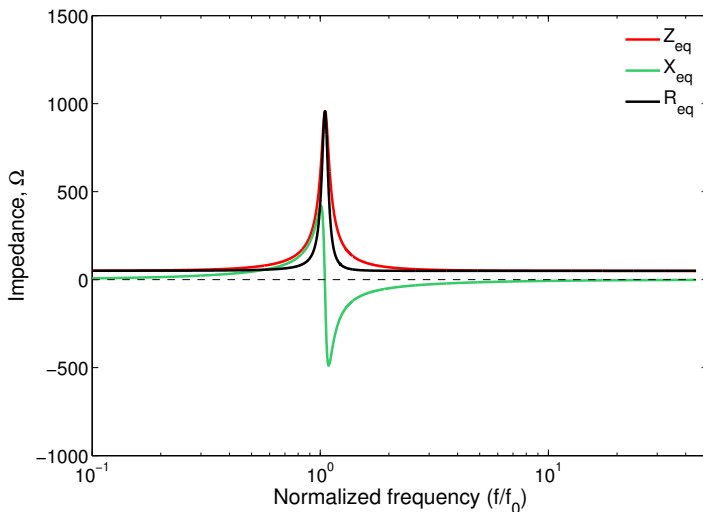


Figure 2.17: Equivalent circuit impedance w.r.t frequency for PP topology

The WPT system for this topology will be subjected in the same conditions as in case of the PS topology. Hence, is optimal to drive it with a current source due to its great impedance at the resonance frequency.

2.5.2.5 Discussion

In this section the comparison between each topology is done. The choice of the optimal compensation topology will be made depending on the power levels for a given system load. With the system parameters values, tabulated in Table 2.2, the expressions of the efficiency and output power are expressed in Figures 2.18 and 2.19.

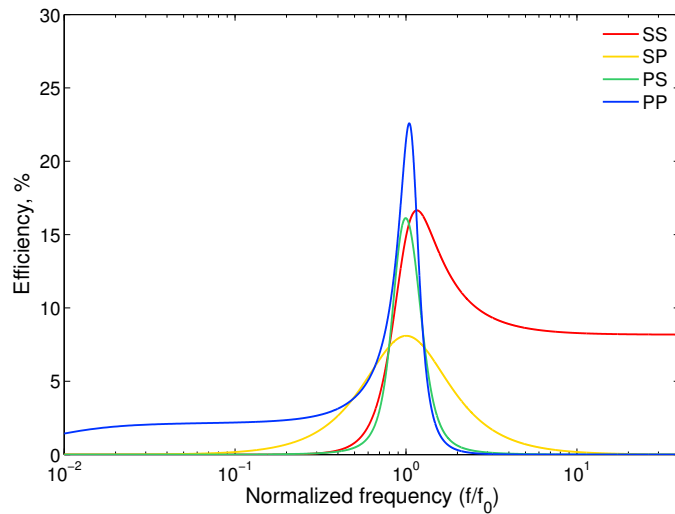


Figure 2.18: Efficiency for all topologies

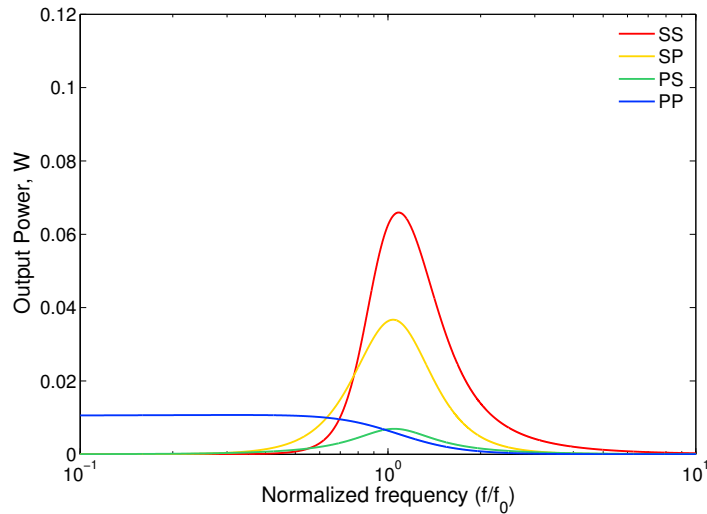


Figure 2.19: Output power for all topologies

The previous figures show that, for the chosen parameters, the optimal topology in terms of output power is the SS topology. The primary series topology has the characteristic that

the compensator capacitor does not depend on the load, so it is a good option to select when the loading profile is variable. By comparing the two primary series topologies, when the load becomes higher it is optimal to select a SP topology because the more load resistance, the higher output power levels. This statement can be verified looking at Figure 2.20.

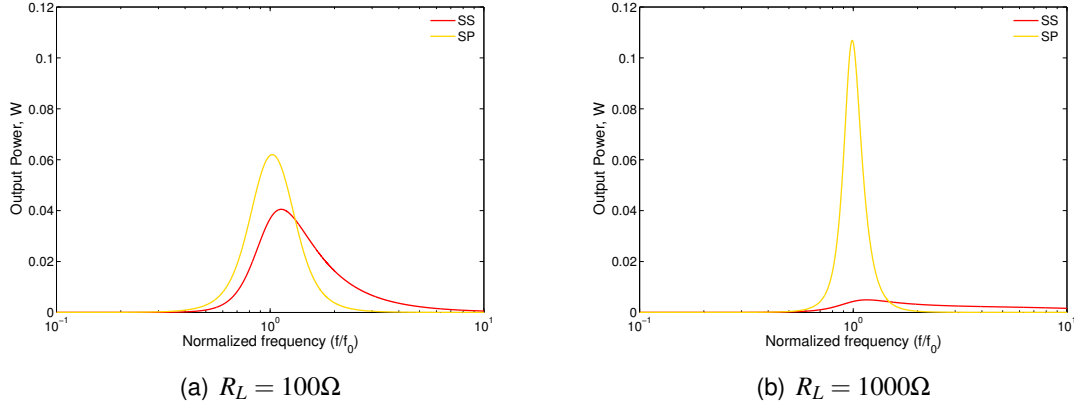


Figure 2.20: Output power for SS and SP topologies varying the load resistance

For primary compensated topologies, the compensator capacitor varies with the system load whether is desirable to transfer maximum consumable power at a specific frequency. The output power for these topologies increases when the system load becomes small. In Figure 2.21, the power roughly increases for a PS topology for a small system load but with a lower frequency tolerance. In contrast, a PP topology has a high frequency tolerance in terms of output power. If the system has not a good frequency stability, the best topology to select is the PP topology.

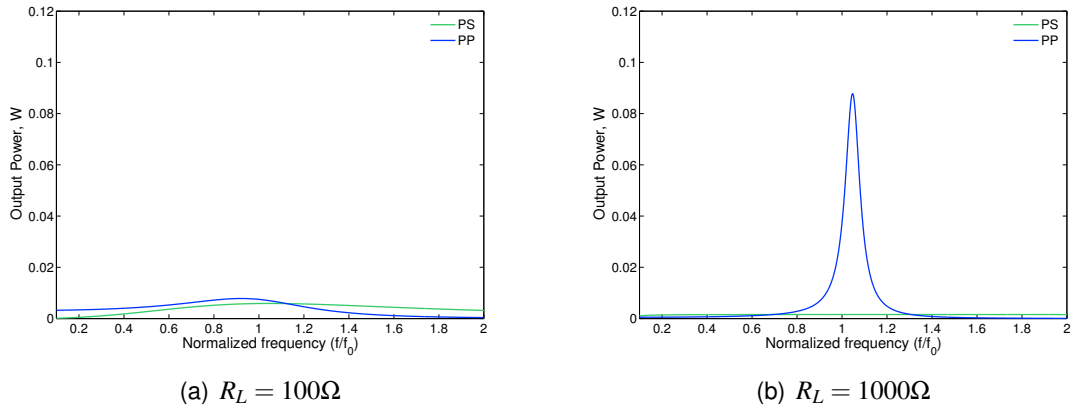


Figure 2.21: Output power for SS and SP topologies varying the load resistance

As previous figures show, the worts topology in terms of output frequency is the PS topology. Then, this topology is rejected for using in the studied application. The remaining topologies have good power levels but only one can be selected.

For low load resistances, the better option is the SS topology and is the best manner to transfer energy because both primary and secondary capacitors delete the imaginary parts of impedance allowing to transfer active power.

When the load resistance increases, secondary parallel capacitors are necessary. To select between SP or PP topologies, we are focused in the effect of the primary capacitors. PP topology generates more amount of reactive power (losses) than SP topology with resonant capacitor, due to the parallel capacitor position on both sides. As a result, the second selected topology is SP topology.

In following sections is discussed the performance of these two topologies and is determined which is the most suitable form to place the compensation capacitors.

2.6 Design Considerations

Wireless power transfer is a promising way of transfer energy which is said to extend and create new applications restricted in past because of energy issues. By implementing the coupling system on a nano-quadcopter we are trying to enlarge this list of applications. Nevertheless, this attempt of bringing WPT to a new dimension using a nano-quadcopter have involved serious payload constraints.

2.6.1 Power Level

The power level describes how much power the system is dealing with. We focus on the input and output power of the system, P_{in} and P_{out} respectively, which define induction efficiency.

$$\eta = \frac{P_{out}}{P_{in}} \quad (2.40)$$

Although a high power level is not a priority, it is necessary to have at least the boundary power value necessary for running the final application. Whether this power level is higher as the desired it will mean that the distance z (which is referred to the axial distance) could be increased.

While power level is smaller than expected, it would be necessary to increase at least one of the following parameters in order to rise the transferred power:

- Mutual inductance
- Voltage induced in the secondary coil
- Current through the primary coil

The three parameters are quite related among them. The first one, mutual inductance is strongly dependent on the distance ($M \propto 1/z^3$). Thus, the first and easiest solution is reduce the axial distance between coils. The second possibility is to increase the induced voltage in the secondary coil, which is proportionally to the operating frequency. Eventually, the magnetizing current through the primary coil can rised by decreasing the operating frequency. This may sound weird since the power transferred can be increased by either decreasing or increasing frequency. A trade-off should be sought to maintain the output power without compromising the transfer distance.

Another important point to consider, once distance and frequency are established, is impedance matching. As we said in Section 2.5.1 the maximum transfer power occurs

when there is an impedance matching between Z_1 and Z_R . Taking into account that the only variable parameter inside the Z_R expression is the resistance of the load R_L , it will be necessary to define the most suitable load value. Note that the reflected impedance depends on R_L and distance, which is expressed by mutual inductance M . This lead to define an average value of R_L for an specific range of distances.

2.6.2 Quality Factor

The quality factor or Q factor is a dimensionless parameter that describes how under-damped a power antenna is; the higher Q factor, the less damping there is. Thus, both Tx and Rx coils are intended to have great Q factor values because the higher the Q factor are, the higher the transfer efficiency will be [5]. Q factor at the same time is the response to the previous power trade-off between a higher frequency and therefore higher induced voltage or lower frequency and a greater magnetizing current, and it defined as:

$$Q = \frac{\omega L}{R} = \frac{\omega_0}{\Delta\omega} \quad (2.41)$$

Q depends on the applied frequency $2\pi f = \omega$, the inductance value L and the resistance of the coil R . Occasionally radiation resistance R_{rad} is included in the denominator [26]. As stated before in Section 2.4.1 this resistance can be neglected. Q factor also can be seen as a selectivity factor, that is why it is sometimes defined as the quotient of natural frequency ω_0 by the bandwidth $\Delta\omega$.

Q factor is an image of the quality of a given coil. It defines its capacity to generate a large magnetic field and low losses [3]. According to [27], a quality factor below 10 represents a really poor coil that should be avoided for WPT, and values around 100 are excellent for industrial applications. *Good* coils will permit higher operating frequencies, while coils with small Q factor will tend to transfer at lower frequencies as is shown in the next figure.

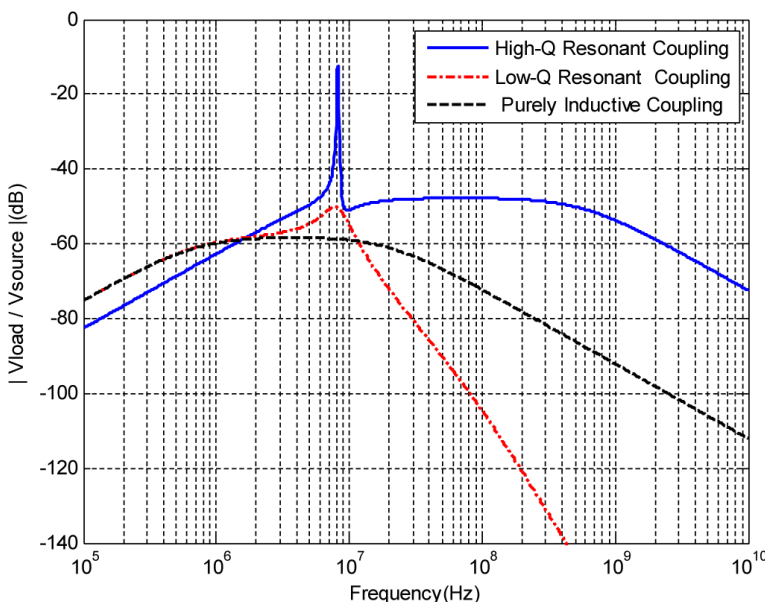


Figure 2.22: Voltage transfer function over frequency for different systems

From Figure 2.22 it can be observed three different inductive coupling systems. The high-Q resonant coupling has the highest Q factor, and therefore the narrower bandwidth. Note that in some applications, such as ours, the Q factor is not always the higher, the better. A really high Q factor above 1000, achieved by using open-ended helical coils like in [8], involves a tight bandwidth. Since the resonant frequencies of Tx and Rx coils can not be identically the same, a too narrower band could cause mistuning. In the above figure it can be noticed the huge difference between a pure inductive system and a resonant one. It must be remarked for resonant systems that after their resonant frequency, the overall performance is cut down.

2.6.3 Coupling Factor

Together with Q factor, the coupling factor is the most typical parameter to describe air-core transformers. It is expressed as follows:

$$k = \frac{M}{\sqrt{L_1 L_2}} \quad (2.42)$$

This performance parameter measures the fraction of magnetic flux generated by the *Tx* coil is penetrating the *Rx* coil. The more flux reaches the *Rx* coil, the better the two coils are coupled. This level of coupling is expressed by the coupling factor k . It varies between 0 and 1. For $k = 0$ the two coils are completely decoupled, while the ideal $k = 1$ would mean totally coupled coils.

Coupling factor is determined by the size and the position of primary and secondary coils. In Section 2.6.5.5 it is discussed the better coils dimension with the purpose to maximize the coupling between them.

2.6.4 Operating Frequency

The operating frequency is another important design consideration in the WPT system. This frequency describes the rate of generation of the electromagnetic waves by the primary coil. For sure, the secondary coil must be designed to work at the operating frequency. As mentioned earlier in Section 2.3.2, to work at resonance it is necessary to drive the primary coil from an external source, in our case it will be an oscillator the responsible of producing the periodic sine wave, *oscillating* at the same operating frequency.

Determine the ideal operating frequency is not possible without knowing many factors as, coil sizes, Q factors, self-resonant frequency, efficiency, etc. Hence, it is intended to determine the suitable frequency band in which the coils could work properly. This frequency range takes into account either the upper and lower frequency boundaries.

The upper limit is restricted by the maximum switching frequency of the transmitter power driver (red dashed line in Figure 2.23). Another limitation at high frequencies is the one related to coil self-resonance frequency (f_s), and so the parasitic capacitance of the coils. Initially any coil is designed to work at f_s to provide the highest possible Q factor.

Exciting the windings with an excitation frequency of approximately 10% of f_s will ensure that the parasitic capacitive effects will not influence the inductor impedance values, and

that the parasitic capacitances can be removed from the inductor model shown in Figure 2.8 [22]. Owing to the fact that the experimental results of f_s are not higher than 30 MHz, the maximal operating frequency is set to be at least 5 times lower than the self resonance frequency, as follows,

$$f \leq \frac{f_s}{5} \quad (2.43)$$

For low frequencies there are no restrictions, but recommendations. The *Wireless Power Consortium* suggests as admissible, Q factor values above 100 for WPT applications. To achieve the desired Q factor, frequencies higher than 500 kHz are typically needed.

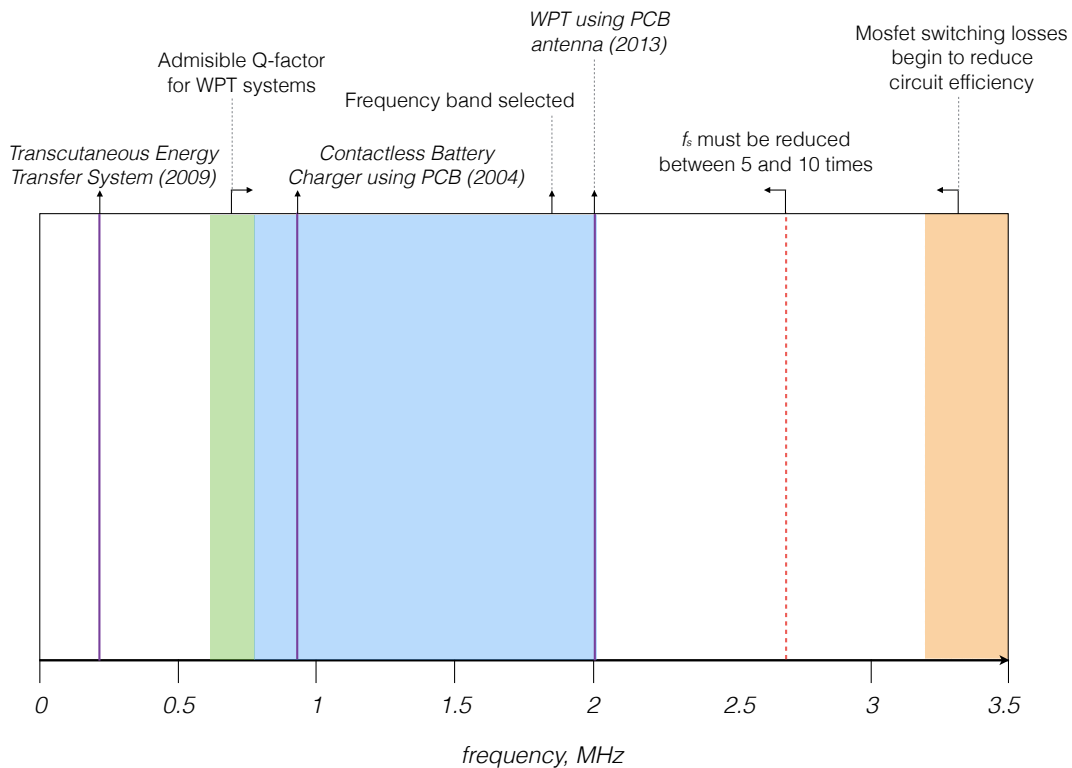


Figure 2.23: Frequency band constraints

Figure 2.23 shows the specific frequency band for coils' diameters between 3 and 10 cm which is the desired order of magnitude of the coils. The vertical purple lines indicate different⁵ works based on WPT systems similar as ours in terms of transfer distance and coil sizes.

Having set the frequency boundaries and some WPT example applications, for this work the frequency band between 700 kHz and 2 MHz is studied for the next proposed systems.

⁵Transcutaneous Energy Transfer System [1], Contactless Battery Charger using PCB [28] and WPT using PCB antenna [29] are useful examples to consider when selecting the operating frequency.

2.6.5 Size and Weight

In order to study the behaviour of coils depending on the different coil parameters, such as coil diameter, number of turns, metal conductor or conductor diameter, different models have been designed and tested.

Before knowing power specifications, coil outfitting supports or drone's stability limitations we began to design the power coils. Using a nano-quadcopter as carrying system and resonant induction as mean of power transfer, we set a goal in transferring power up to 20 cm. We chose these range of distances based on previous works [17] [18] [30]⁶. In front of a design with at least four freedom degrees we decided to fence each variable to reduce the number of possible coil designs.

Parameter	Definition
R	Coil radius
D	Coil diameter
A	Coil area
d	Wire diameter
l	Wire length
S	Wire section
h	Coil height
z	Axial distance
N	Number of turns
m	Coil mass

Table 2.3: Geometric parameters of coil models.

2.6.5.1 Coil Shape

Winding shape is the most common type of sorting coils. Typical shapes of WPT inductors include circular, square, rectangular and all regular polygons. Whether all these shapes are compared for a given size of the inductor area, it is seen that circular coils obtain a higher magnetic coupling than any other shape. This can be explained by the distortion of the field distribution around the corners of those shapes [31]. Using circular coils we ensure to have the higher possible efficiency.

2.6.5.2 Metal Conductor

Each conductor has a different electrical resistivity which is an important parameter to define its DC and AC resistance. This defines the metal used to produce the coils. The following table shows the electrical resistivity of common metal conductors at 20 °C.

At first sight silver seems the best conductor due to it has the lowest electrical resistivity and consequently lowest internal resistance at room temperature, but the huge price difference between silver and copper is not worth for only an increase of 5% in electrical

⁶All the publications selected are similar with regards to operating frequency.

Electrical resistivity of Aluminum	$2.44 \cdot 10 \times 10^{-8} (\Omega \cdot \text{m})$
Electrical resistivity of Gold	$1.72 \cdot 10 \times 10^{-8} (\Omega \cdot \text{m})$
Electrical resistivity of Copper	$1.68 \cdot 10 \times 10^{-8} (\Omega \cdot \text{m})$
Electrical resistivity of Silver	$1.59 \cdot 10 \times 10^{-8} (\Omega \cdot \text{m})$

Table 2.4: Electrical resistivity of several common metal conductors

resistivity. Silver is approximately 140 times more expensive than copper [32]. As a result, the power coils are made of copper.

2.6.5.3 Conductor Diameter

This parameter is strongly related with skin effect, discussed in Section 2.4.1, and therefore wire resistance. It was analysed whether for the same coil height h , fixing the main radius R , it was advisable to maximize the number of turns or wire diameter.

Figure 2.24 shows that for smaller wire diameter, e.g. $d=0.5$ mm and $N=20$ turns, a bigger inductance (Equation 2.20) value is achieved in comparison to any other configuration with the same h , such as $d=1$ mm and $N=10$ turns. It seems to be better for coil Q factor to reduce wire section, but as always it is a compromise. As Figure 2.9 shows, decreasing wire diameter we are increasing coil resistance. This effect is most notorious for high frequencies. Hence, it is necessary to “wait” for quality factor values.

As stated previously in 2.4.1 to obtain a good wire performance, the minimum wire diameter will be five times the skin depth δ . Hence, above 1 MHz the minimum diameter will necessary be at least $47 \mu\text{m}$.

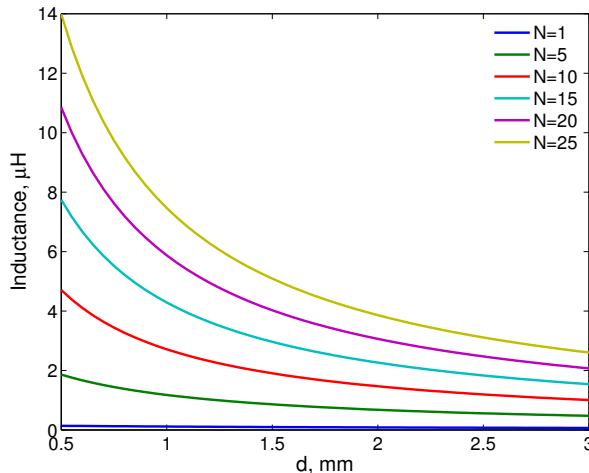


Figure 2.24: Inductance w.r.t. wire diameter for fixed coil radius of 4 cm and different turns

Due to commercial availability we select two different wire diameter, displayed in the following table:

Wire diameter	Insulation	Total diameter
1 mm	Polymeric varnish	~ 1 mm
0.59 mm	Polymeric layer	1.4 mm

Table 2.5: Wire diameter

2.6.5.4 Number of turns

First, we determine the maximum number of turns for the quad-copter in 20 turns. This number did not compromise the drone stability in its vertical axis because does not change at all the gravity center. Having a wire reference maximum diameter of 1.4 mm, it means that the largest coil of 20 turns will have 2.8 cm of height, even less height than the quad-copter.

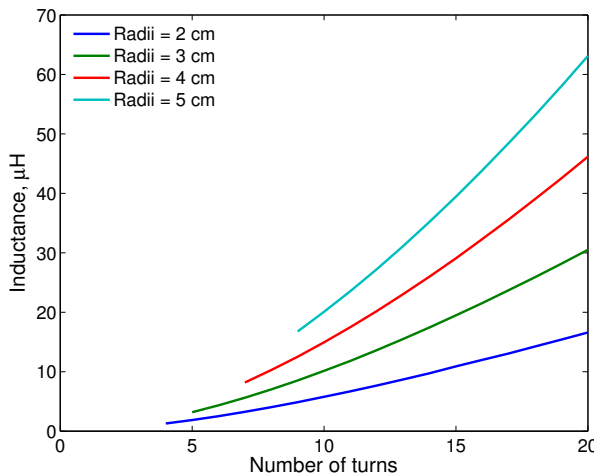
**Figure 2.25:** Calculated inductance for different number of turns and coil radii values

Figure 2.25 shows coil inductance depending on the number of turns and on the radius. As the number of turns is increased, coil inductance rises proportionally. In addition, for the same number of turns, higher inductance values are obtained whether the coil radius is increased. It is observed that plotted lines tend to move to the right. This effect is caused by the interpolation method used in this graph, which does not provide higher D/h values from the reference table [21]. Initially, an increase in coil's radius appears to improve the quality factor of the coil which is a desired purpose. Regrettably we are again in a trade-off situation. By increasing the number of turns we are also increasing the total wire length. This results in a lower quality factor knowing that it is inversely proportional to coil resistance (Equation 2.41). It must be mentioned here that coupling factor does not depend on the number of turns.

2.6.5.5 Coil radius

As we said in 1.5, midrange WPT applications contain distances from coil diameter up to ten times the coil diameter. Thus, if we aspire to transfer power up to 20 cm, at least, a coil with 2 cm of diameter is needed. To design such a smaller coil was refused because it

involved imprecise winding, and obviously the smaller the coil area, the smaller magnetic flux is created (2.3). On the contrary, a great area will imply to have an unbalanced drone which is not designed for carrying oversized objects. The increase in coil area probably will turn into an overall weight-gain.

Furthermore, it has been studied the relation between Tx and Rx coil area. An axial distance between coils several times the coil radius implies a very small coupling factor k which can be around 0.01 [33]. Taking into account that coupling factor lies between 0 and 1, this low value means that only a small amount of the flux generated by Tx coil links the Rx coil.

The dashed line set in 0.05 m on the vertical axis means the maximum Tx radius allowable owing to the nano-quadcopter dimensions.

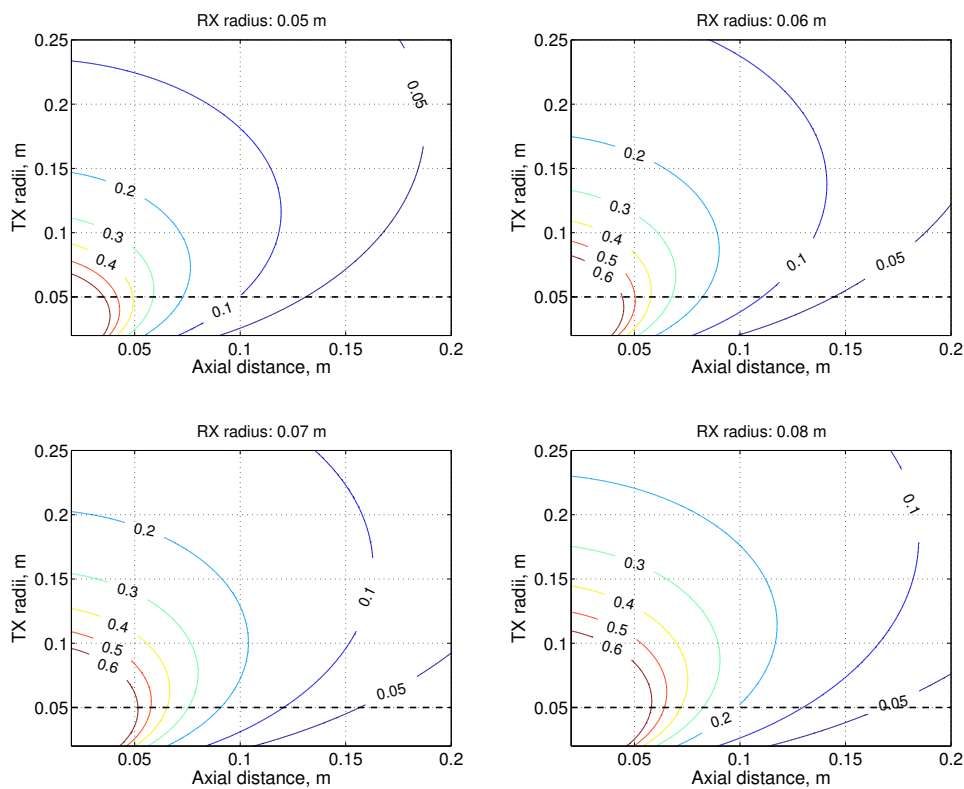


Figure 2.26: Contour lines of the magnetic coupling obtained for different distances

Contrary to common assumption, for larger air gaps the maximum of the magnetic coupling k can not be reached with coils of equal size [31]. Figure 2.26 shows the contour lines of the magnetic coupling factor for different air distances and transmitter coil radii for four receiver coil radii. In this case, it has been used the Equation 2.19 to calculate inductances.

It can be shown that bigger Rx coils radii improve the coupling factor between the coils, meanwhile increasing Tx coil radius does not involve achieving higher k factor. This can be seen with the following example; for a given air gap distance, $z = 0.1$ m, and a fixed Rx radius, $R_{RX} = 0.05$ m, by increasing Rx radius in 3 cm we see that the coupling factor doubles its value from 0.1 to 0.2. However much Tx radius is increased, it will never be possible to duplicate k for the chosen axial distance.

2.6.5.6 Weight

The *Crazyflie 2.0* 4 DC-motors give it a maximum take-off weight of 42 g [34]. Part of this payload must be reserved for the transmission circuit and coil's outfitting supports, so we decide to set the coil mass in about 12 g. It must be said that this limitation only affects to the transmitter side.

2.7 Detailed Designs

With intent to create completely different coils we decided to maximize both the coil area and the number of turns while fixing the other variables. The coil shape was round because of its benefits when creating a magnetic field. A copper wire was chosen for its low electrical resistance, as it was said previously.

Three coils were designed using the algorithm shown in Figure 2.27. The algorithm is thought for a 1 mm copper wire diameter. It maximizes the coil weight in order to take advantage of the quadcopter performance. This results in two completely different coil designs. Note that all coil possibilities have the same or similar lengths. The first model prioritizes the largest possible radius and so few turns. The second is designed with the minimum radius, which is defined in subsection 2.6.5.5, and the maximum turns permitted. A third model was created in order to test a trade-off model. These “candidates” will allow us to discern clearly the difference between coils’ behaviour.

Model name	Turns	Radius	Wire diameter	D/h ratio	Tx mass
Model A	8	5 cm	0.597 mm	11.9	13.4 g
Model B	19	2 cm	0.597 mm	1.5	14.1 g
Model C	10	4 cm	0.597 mm	5.71	13.5 g
Model D1	7	4 cm	1 mm	8	17.3 g
Model D2	11	1.5 cm	1 mm	2.73	9.8 g

Table 2.6: Geometric parameters of coil models

Both *Tx* and *Rx* coils were designed with the same dimensions for each of the models A, B and C. This assumption simplifies future computations and also provides us with an added ease for the coil winding procedure. Anyway, we build the last two single-models *D1* and *D2* in order to demonstrate the theoretical calculations, which state that an increment in *Rx* radius is preferred upon the same increment in *Tx* radius.

All the experimental results are carried out for wire of 1.4 mm of diameter, but including its covering (0.59 mm without covering). In this manner we take into account the increase in mass because of the thermal epoxy adhesive inclusion. The wire diameter reduction does not affect since it does still not surpass the boundary stated skin depth, $d > 5\delta$. Thus, we ensure not to surpass the maximum payload after adding the adhesive fixation, using a “lighter” wire owing to a reduction in the cross-sectional area. In addition, the parasitic capacitance of the coil is reduced due to wire plastic layers, and therefore more space between wires.

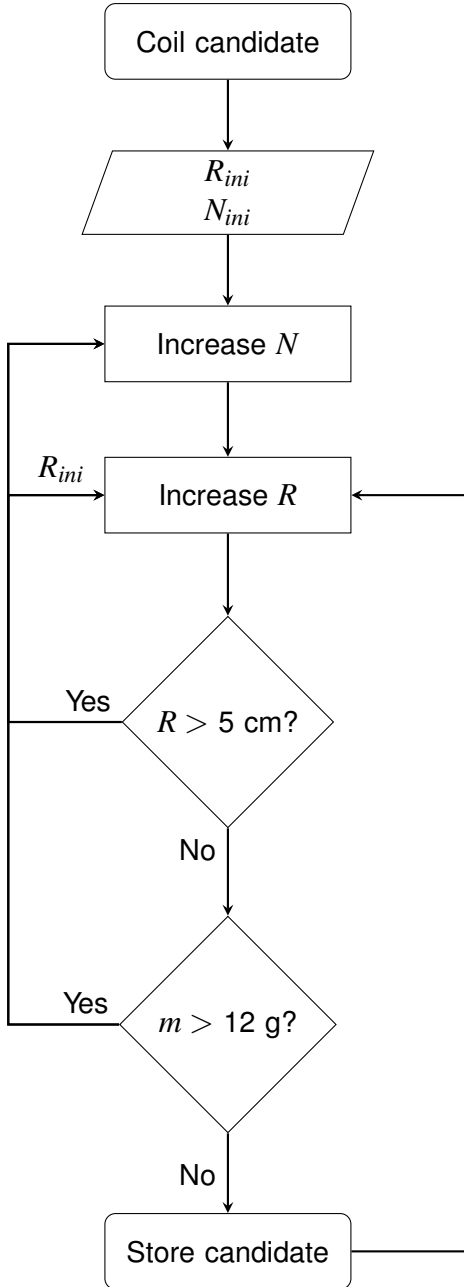


Figure 2.27: Flowchart of the algorithm to design the coil size

2.7.1 Discussion

The decision of which coil model will be outfitted on the quadcopter is based on two criteria: performance and stability. Performance is related with the ability of transfer energy from the source to the load, and so the power transferred and the efficiency. In spite of the fact that the performance has been studied in detail selecting the best compensation topology, in this project the main goal is intended to transfer power, hence the efficiency will not be a decisive parameter.

The second and not less important criteria has to do with weight and shape. Having all the models similar weight it will be determinant to see how does each model behaves,

together with the quadcopter.

It will be necessary to wait until experimental tests to decide which coil is the most suitable. Then, according to the chosen model, it will be set one or other operating frequency.

In Chapter 4, all models are tested and compared with theoretical results. It will also be demonstrated that model C is the most appropriate model for transferring power.

CHAPTER 3. ARCHITECTURE AND DESIGN OF THE WPT SYSTEM

Once the inductive coupling system has been studied in detail, it is time to outfit the selected coil model C on the drone. The selection of this model is argued in Chapter 4, after all the measures are performed. In this chapter, the required circuits to design the WPT system are discussed. In the first section, the nano-quadcopter used is introduced and all its main features are explained, as well as the necessity of designing brand new motor mounts in order to support the coil.

In the second part of the chapter, the architecture of the transmitter and receiver circuits is explained, as well as its design. The main feature of the WPT system lies on energy conversion. Hence, both the transmitter and the receiver circuits need of power converters. As shown in Figure 3.1 the transmitter includes a ultra low DC-DC converter and a DC-AC converter. At the receiving side, the power converters include at least an AC-DC converter. Later, for the used application, a DC-DC converter will be introduced for the battery recharging circuit.

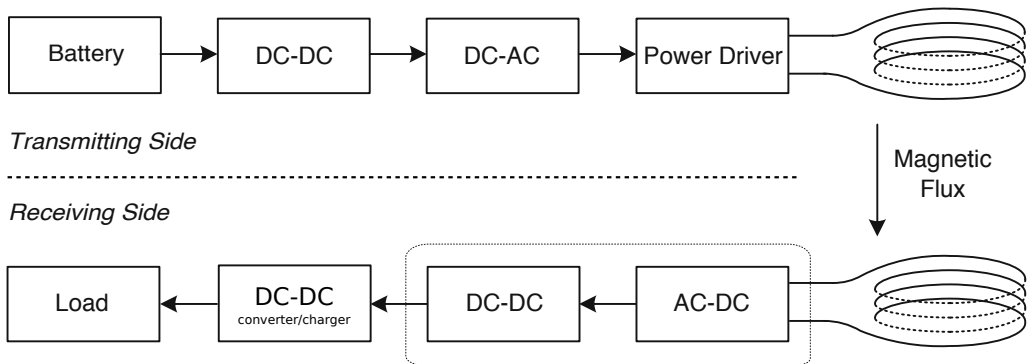


Figure 3.1: Block diagram

3.1 Quadcopter

One of the initial objectives of the project is the WPT system outfitting on the nano-quadcopter. The inclusion of the quadcopter as an energy *transporter* restricts both transmitter and receiver side, but mainly the transmitter because of the weight. The model used in this work is the created by *Bitcraze*, its second nano-quadcopter version, named *Crazyflie 2.0*.

The assembly of this quadcopter can be divided into two parts. The first is composed by the battery, motors and headers attaching. In the second, the propellers are introduced and balanced. This last procedure is really important due the fact that well balanced propellers reduce vibrations in the copter and noise in the sensors improving the stability of the *Crazyflie*.



(a) Crazyflie 2.0

(b) CrazyRadio USB dongle

Figure 3.2: Transmitter circuit

Contrary to other drones, *Crazyflie* allowed us the possibility to fly it indoor. It also has many interesting features listed in Table 3.3 which made us to select it. Owing to the fact that *Crazyflie* is an open source project it is possible to log, graph and set variables in real-time via the USB radio dongle.

Crazyflie 2.0 specification	
Size (WxHxD)	92x92x29 mm
Radio specs	Low energy Bluetooth Radio amplifier 1 km range
Controllers	STM32F405 MCU μ USB connector USB OTG capability
IMU	3 axis gyro 3 axis accelerometer 3 axis magnetometer Pressure sensor

Figure 3.3: Crazyflie 2.0 features

3.1.1 Controlling the *Crazyflie*

As it is shown in Table 3.3, the *Crazyflie* can be either controlled by a mobile device or a computer. Using a mobile device is the fastest way to control it, but its maneuverability is reduced compared to the computer option. Therefore, this last one is chosen.

The two needed requirements for flying the *Crazyflie* using a computer are: a radio USB dongle (*Crazyflie PA*) for communication and a standard gamepad for maneuvering. In addition, a virtualization program is required to run the *Crazyflie* client. Few drivers are needed, as well as the last updated software in order to avoid any *bug*. Both drivers and the needed code are uploaded on *Github* repositories [35].

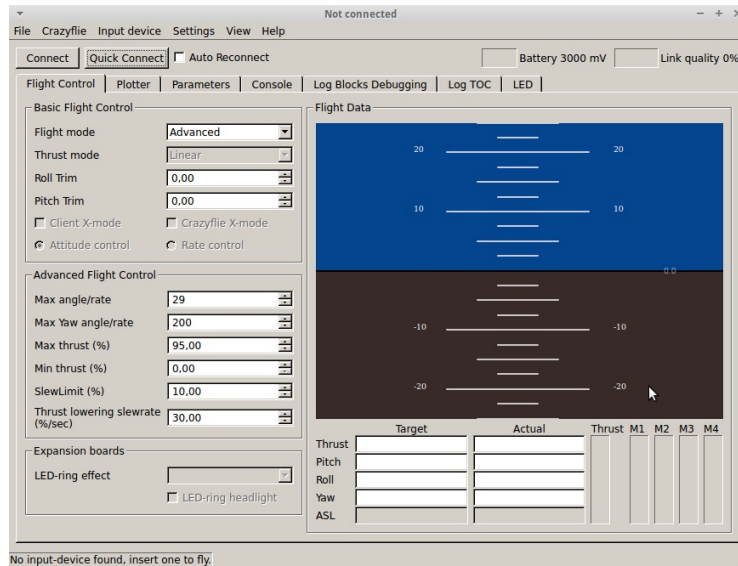


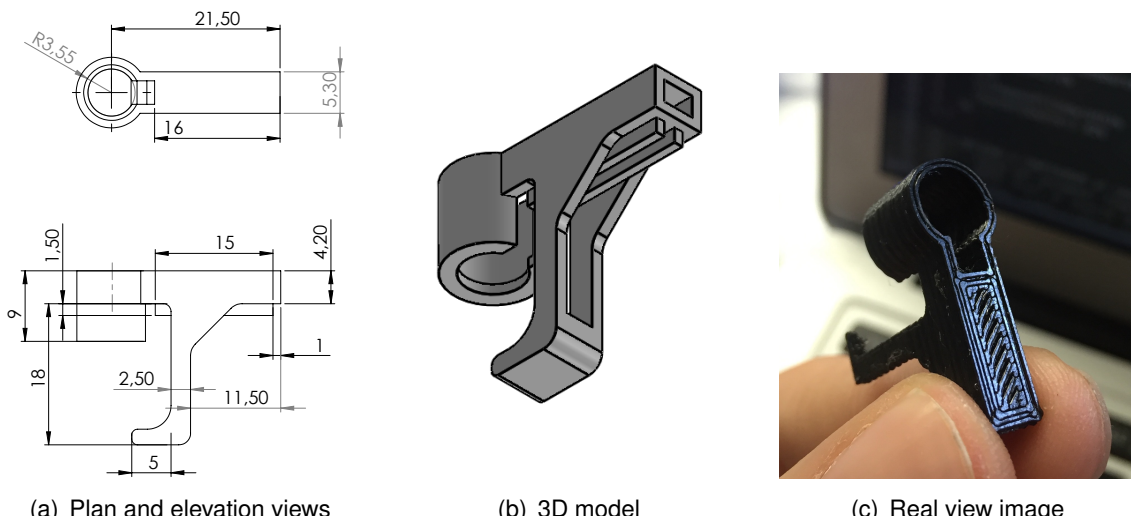
Figure 3.4: Crazyflie's computer client

3.1.2 Motor Mount Design

With the original design of the *Crazyflie* nano-quadcopter is almost impossible to install it the used coil. As a consequence, in this case, the coil would not be subjected neither precisely, nor “smartly”. The solution is to redesign the motor mounts of the *Crazyflie* to accomplish a good coil support.

Using the CAD software *SolidWorks*, it has been designed a motor mount with the same characteristics of the original mounts. The only difference is that the designed structure is made to place the coil under the *Crazyflie*.

This structure has the main characteristic of supporting lateral stresses, as the *default* mounts, and also to prevent the fall of the coil, by using a kind of hook placed at the end of the mount arm. The complete design schematics are located in the Appendices. All this mentioned characteristics are showed in Figures 3.5(a) and 3.5(b).



(a) Plan and elevation views

(b) 3D model

(c) Real view image

Figure 3.5: Motor mount process design

Once the motor mount is designed it can be printed with a 3D printer. The result is exhibited in Figure 3.5(c).

3.2 Transmission System

In a WPT system, the transmitter is intended for carrying power in order to satisfy the receiver demand. Its design is based on two premises; size and weight. Size is important in order to maintain the nano-quadcopter balanced owing to *Crazyflie* is not designed to carry objects. The weight constraint is repeated several times during this project.

3.2.1 Power Source

After considering different options, such as using two isolated batteries for feeding the drone and the induction system separately, we decided to use the default battery of the nano-quadcopter, and so avoiding to increase the total weight. The battery *Crazyflie* uses is of the type LiPo (Lithium-Polymer).

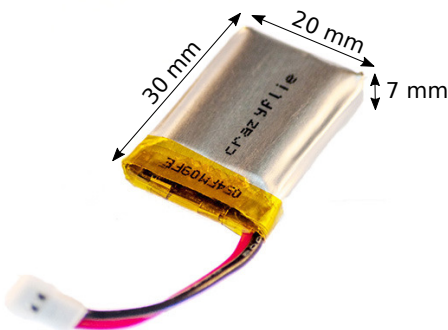


Figure 3.6: *Crazyflie's* battery size

Although LiPo is not the safest chemistry, these batteries are currently the most popular type for radiocontrol use. The reason is due to LiPo batteries has the best power to weight ratios and discharge currents. It also allows to use only a single cell.

Capacity	Nominal voltage	Discharge	Charge
240 mAh	3.7 V	15C	2C

Table 3.1: Battery's electrical specifications

The electrochemical batteries have the advantage over other energy storage devices, such as supercapacitors, that their main discharge curve is exponential, meaning that the energy stays high during most of the charge and then drops rapidly as the charge depletes [36]. The *Crazyflie* battery discharge rate or C-rate is of 15C which means 15-times the rated capacity.

As it is stated in [34], the maximum flight time with LiPo battery is up to 7 minutes. Theoretically with motors at full power and consuming 3600 mA, the flight is being reduced

to 4 minutes. Regrettably, this time will be even reduced by the inclusion of the induction system.

The end-of-discharge voltage for most LiPo is 3.0 V/cell. At this level, roughly 95 percent of the energy is spent and the voltage would drop rapidly if the discharge were to continue [36]. To protect the battery from over-discharging, which is very sensitive to, the quadcopter comes with a PCM (Protection Circuit Module) that prevents operation beyond a specified end-of-discharge voltage.

3.2.2 Voltage Regulator

The voltage regulator was the last system implementation. Owing to the necessity of having 12 V, explained in Chapter 4, on the transistor collector, a switching voltage regulator is the most appropriate solution. Linear regulators can only step down the input voltage and the possibility of adding a second battery was rejected because of weight.

Switching regulators are highly efficient and able to boost, buck and invert voltages with ease, but they also have weaknesses. One of them is that they are complex chips and, consequently, it can take a lot of design effort to get a new product working properly. In addition, the level of integration of contemporary switching regulators does not come cheaply and increases the chip size [37].

To solve these issues the *Webench* application is used. This design tool developed by *Texas Instruments* allows to design the voltage regulator that better adjusts to our input and output power requirements.

Input Voltage	Output Voltage	Output Current
3 - 3.7 V	12 V	0.5 A

Table 3.2: Regulator requirements

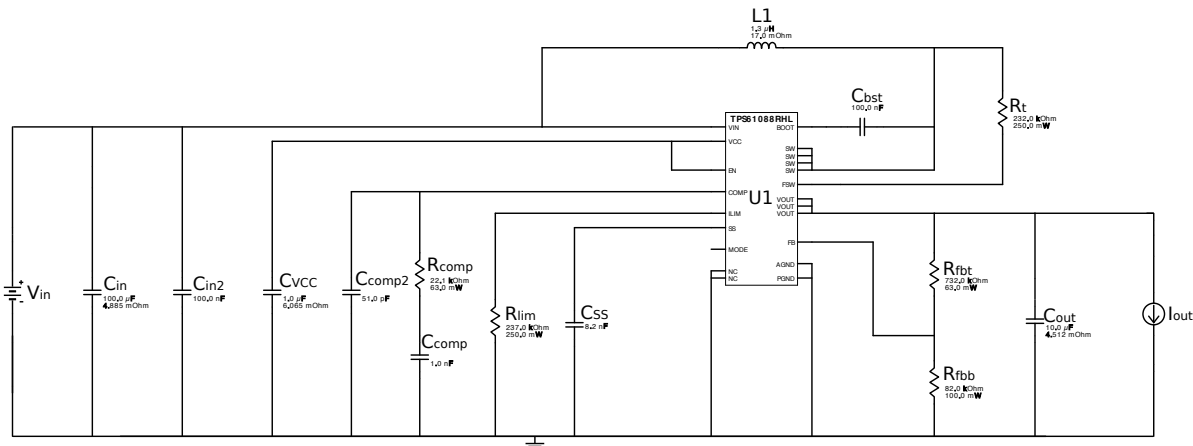


Figure 3.7: TPS61088 design circuit

It must be said that the regulator is designed to provide a maximum output current of 500 mA, which is the maximum input current of the power driver, discussed later.

The requirements above lead us to different switching regulators. By looking at size and efficiency, the TPS 61088 was the one with best efficiency per unit of area. The circuit schematic is given in Appendix D.1.

Although an ideal switcher has a 100% efficiency, the actual efficiency is about 92% (Appendix D.1) and it depends on the output current and the input voltage. The power *lost* is really low and it is dissipated following,

$$P_{dis} = \left(\frac{1}{\eta} - 1 \right) \cdot P_{out} \quad (3.1)$$

The input current that the regulator is drawing to the battery can be calculated using Equation 3.2, and it defines the global circuit consumption.

$$I_{in} = \left(I_{out} \cdot \frac{V_{out}}{V_{in}} \right) / \eta \quad (3.2)$$

Before computing I_{in} , it will be necessary to figure out which is the output current and which relies on the power driver.

3.2.3 Oscillator

A Quartz Crystal Oscillator (XO) is used to generate the necessary periodic signal which generates the alternating current in the *Tx* coil. It is selected for its good performance, a low power consumption, and a simple electronic circuit. This type of oscillator not only provides an extraordinary frequency stability, but it also provides a constant frequency output under varying load conditions, which is an important aspect to consider.

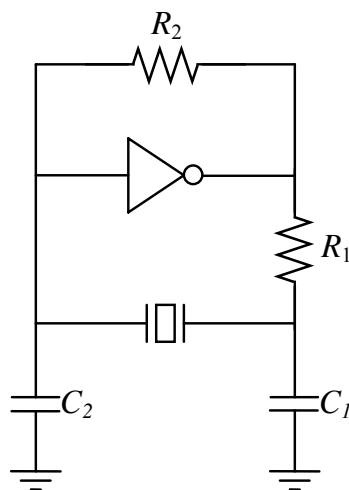


Figure 3.8: Oscillator schematic

The functioning of the quartz crystal oscillator is based on piezoelectric effect. Piezoelectricity is the primary property of a crystal which makes it usable as resonator. Piezoelectricity is a reversible property of a crystal by which an electrical charge produces a mechanical force by changing the shape of the crystal and vice versa, a mechanical force applied to the crystal produces an electrical charge [38].

As it is discussed at the end of the previous chapter, each coil model has its own resonant frequency, and therefore a unique oscillator circuit. For the selected coil model, the resonant frequency is 0.95 MHz.

The characteristic frequency of the crystal, or rate of vibration, is determined by the cut, size, and shape of the quartz crystal. Therefore, to achieve the desired frequency of 0.95 MHz a special crystal is needed. Hence, taking advantage on the wide Q factor of coils, a standard crystal frequency of 1 MHz is selected.

Parameter	Value
Frequency	1 MHz
R_1	9.1 MΩ
R_2	910 Ω
C_1	47 pF
C_2	47 pF
Consumption	8.4 mA

Table 3.3: XO parameters

In figure above, it is represented the Pierce oscillator circuit. This parallel oscillator is a derivative of the Colpitts oscillator. The circuit is implemented using a minimum of components: a single CMOS inverter gate, two resistors, two capacitors and the quartz crystal.

For high speed CMOS logic families, typically [39]:

- R_1 is between 8.2 MΩ and 10 MΩ
- R_2 is between 470 Ω and 2220 Ω
- C_1 and C_2 are of the order of 62 pF

3.2.4 Power Driver

The output power delivered from the oscillator is not enough to feed the inductor directly. Thus, a Darlington transistor has been placed after the oscillator to elevate the magnetizing current through the primary coil. This increase in the input power will allow the system to transfer power up to larger distances.

The ULN2803A driver is a high-voltage, high-current Darlington transistor array. The device consists of eight NPN Darlington pairs that feature high-voltage outputs with common-cathode clamp diodes for switching inductive loads. Figure 3.9 shows a simplified scheme of the power driver. The complete scheme is attached at Appendix D.2.

From Figure 3.9, it can be observed that the transistor is working such a switch and driven by the square signal of 0-12 V coming from the oscillator. When an input (pins 1 to 8) is driven "HIGH" the corresponding output will switch "LOW" sinking current. Likewise, when the input is driven "LOW" the corresponding output switches to a high impedance state. This high impedance "OFF" state blocks load current and reduces leakage current through the device improving efficiency.

Pin 8 (GND), is connected to the loads ground or 0 volts, while pin 10 (V_{CC}) connects to the loads supply. Then any load needs to be connected between $+V_{CC}$ and an output pin, pins 11 to 18. For inductive loads such as coils, pin 10 should always be connected to V_{CC} .

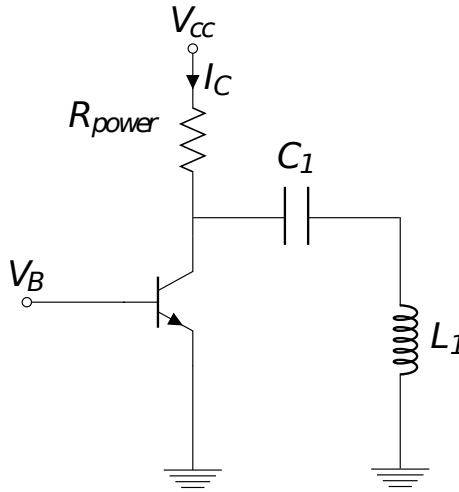


Figure 3.9: Simplified transistor diagram

Parameter	Value
V_{CC}	12 V
$V_{CE(SAT)}$	1.3 V
$I_{CC(MAX)}$	500 mA
R_{power}	33 Ω

Table 3.4: Electrical characteristics

The ULN2803A Darlington driver is capable of switching 500 mA per channel. In our case the collector-current I_{CC} is determined using the next expression,

$$I_{CC} = \frac{V_{CC} - V_{CE(SAT)}}{R_{power}} = 324 \text{ mA} \quad (3.3)$$

where R_{power} is achieved by combining three resistors in parallel. Each resistor has a resistance value of 100 Ω and tolerates powers around 1W without any problems. Once the collector current is calculated, it is possible to calculate the total power demanded from the battery. Substituting I_{CC} in equation 3.2 an input current of 1.05 A is obtained. Therefore, the total theoretical power consumed by the transmitter is:

$$P_{in} = V_{in} \cdot I_{in} = 3.88 \text{ W} \quad (3.4)$$

It must be also considered the maximum switching frequency of the ULN2803A. Table 3.5 exhibits the propagation delay-times. The most restrictive is the change from “LOW” to “HIGH” state which takes 130 ns. The delay time delimits a maximum operating frequency of 7.69 MHz. Lowering the operating frequency from this value ensures a better Darlington efficiency.

Propagation delay time	Value
High-Low	20 ns
Low-High	130 ns

Table 3.5: Switching characteristics

3.2.5 Transmitter Circuit Assembly

A printed circuit board (PCB) is needed for physically supporting and wiring the transmitter circuits (regulator, oscillator and power driver). Working with SMD technology makes possible to reduce mostly all the components size. Its round shape is owing to the fact that weight must be distributed as close as possible to the center of gravity. The circular shape also allows to maximize the board space, as well as, not to disturb the coil placement.

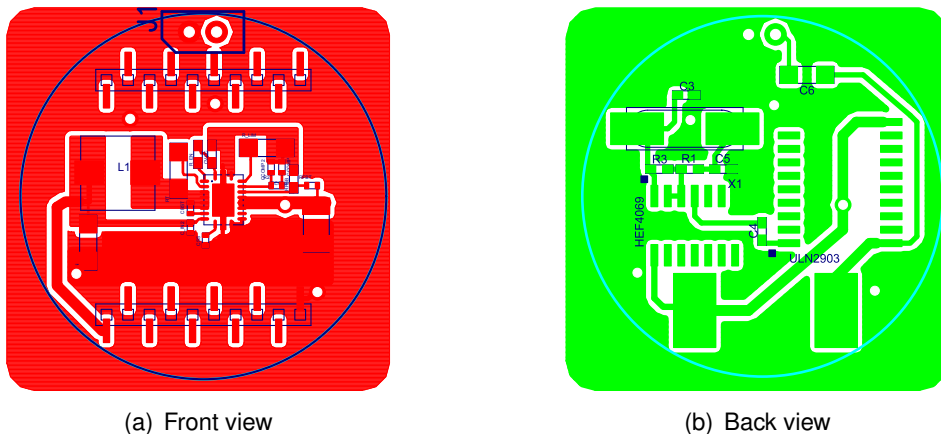
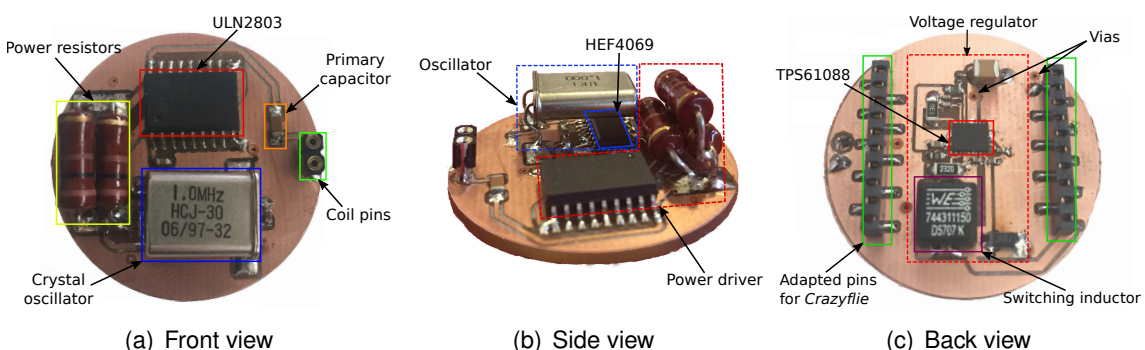
**Figure 3.10:** Transmitter SMD design

Figure 3.11 exhibits the final transmitter board which is divided in two parts. The top side 3.11(a) is composed by the power driver and the oscillator. It has the input coil pins to attach the primary inductor. The bottom side, invisible when the transmitter is connected to the *Crazyflie*, is formed by the voltage regulator and the adapted pins. Those pins permit to connect directly the board to the quadcopter. The board height is small enough to avoid to graze the floor.

**Figure 3.11:** Transmitter circuit

Eventually, the total mass is computed using a precision scale. Table 3.6 shows the mass of each section of the quadcopter. The experimental take-off mass depending on the motors thrust is shown in Figure 3.12.

Element	Weight
Battery	7.1 g
Tx Coil	13.5 g
Tx Circuit	8.5 g
Crazyflie	8.3 g
DC motors	4 x 2.8 g
Motor mounts	4 x 0.8 g
TOTAL	51.8 g

Table 3.6: Mass constraint at transmitter side

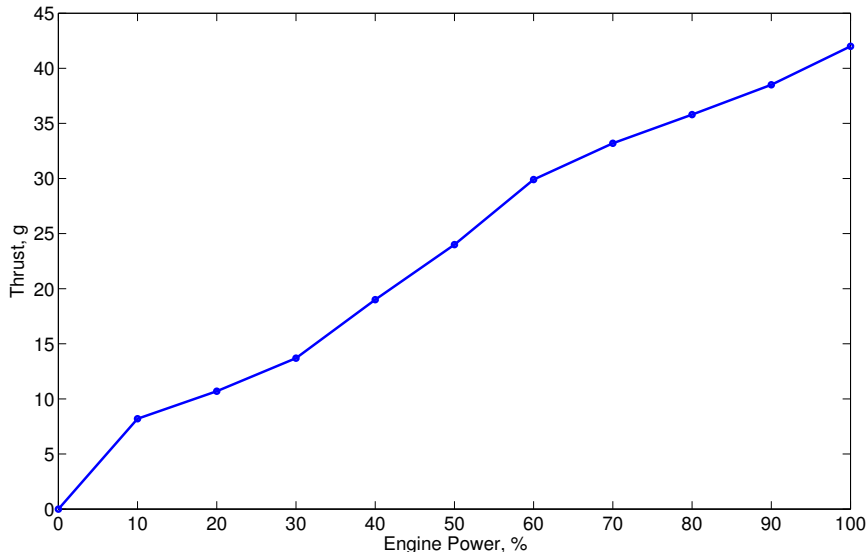


Figure 3.12: Thrust depending on the power level of the motors

3.3 Receiver system

The receiver side for a WPT system has the aim to rectify the transferred AC signal and, once it is in DC, to set it up to the desirable voltage levels. Depending on the application these two characteristic can be done in one stage. In the following sections the used circuits are explained in detail to accomplish a good signal rectification and conditioning. The chosen application for this project is presented in Section 3.3.4.

3.3.1 Voltage Doubler

To rectify the signal is selected a common used circuit for energy harvesting applications, the voltage doubler. This circuit is the perfect option for an energy harvesting. Owing to the low RF voltage levels, the doubler can rectify and condition at the same time. Voltage doubler circuits can be viewed as single stage or of a higher order multiplier; cascading identical stages together it is achieved a greater voltage multiplication. In Figure 3.13 is shown a single stage for voltage doubler.

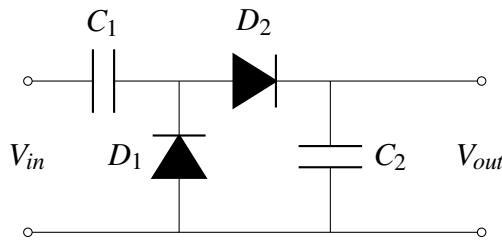


Figure 3.13: Single voltage doubler stage

An understanding of this circuit can be gained by interpreting firstly what occurs when the down swing of the AC current flows through the circuit. The diode D_2 blocks the current flow through C_2 , but not the flow that goes across C_1 . This current flow charges C_1 up to the same level of the AC voltage amplitude. Once the up swing of the AC voltage is reached, the voltage of both AC source and C_1 drop across C_2 , charging it approximately twice the peak voltage of the AC signal [40].

As it is said in the first paragraph the voltage doubler is used in many energy harvesting applications, where the frequency goes from MHz to GHz. Thus, not all diodes are able to commute at these frequencies. The operating frequency of the inductive system of this project is set of 1 MHz and the selected diodes for assembling the voltage doubler are the HSMS-2850 Schottky diodes (SOT-23 Package) from *Avago Technologies*:

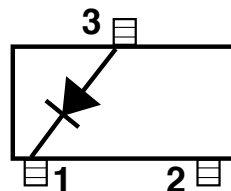


Figure 3.14: SOT-23 Package for HSMS-2850 Schottky diode

The impedance of the HSMS-2850 diode can be linearly modeled as Figure 3.15 shows [41]:

In this case R_s and C_j are the series resistance and the junction capacitance respectively, and R_j has the following expression:

$$R_j = \frac{8.33 \cdot 10^{-5} n T}{I_b + I_s} \quad (3.5)$$

where n is the ideality factor, T is the temperature in Kelvin degrees, I_b is the externally applied bias current in amperes and I_s is the saturation current. All this values, called

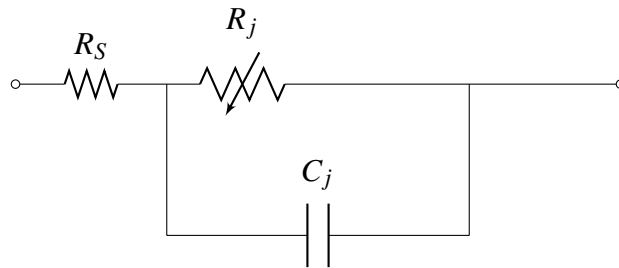


Figure 3.15: Single voltage doubler stage

SPICE¹ parameters, are tabulated in Table 3.7.

Parameter	Units	HSMS-2850
C_j	pF	0.18
I_b	A	$3 \cdot 10^{-4}$
I_s	A	$3 \cdot 10^{-4}$
R_s	Ω	25
n	—	1.06

Table 3.7: SPICE parameters for HSMS-2850

The total impedance Z_{diode} is given by:

$$Z_{diode} = R_S + \frac{R_j}{1 + j\omega C_j R_j} \quad (3.6)$$

In this project are used three stages for the design of the voltage doubler. This stages allows us to obtain good voltage levels at the output with good efficiency. Since, the more voltage doubler stages, the less efficiency.

3.3.2 DC-DC boost converter

The final stage introduced in the whole system is the *bq25504 EVM*. As it is defined in its datasheet on the Appendices, the *bq25504 EVM* is a ultra low power boost converter with battery management for energy harvester applications. This device is an evaluation module (EVM) programmed for deliver a 3.1 VDC maximum voltage (Over Voltage) for charging the storage element with a capacity larger than 100 μ F. The supercapacitor or the battery allows the system to provide any peak currents that never would be obtained from the input source.

The selection of the evaluation module is due to low power levels (among microwatts) needed to start converting the voltage to the programmed levels. The boost converter can be started with an input voltage lower than 330 mV. Below this level until 100 mV, it can operate but with more difficult. Once the 330 mV are reached, the boost converter will operate normally. This fact is called *cold start*.

¹ SPICE (Simulation Program with Integrated Circuit Emphasis) is a general-purpose, open source analog electronic circuit simulator.

The following figure shows the schematic of the *bq25504 EVM* and the output pins where the load and battery has to be placed:

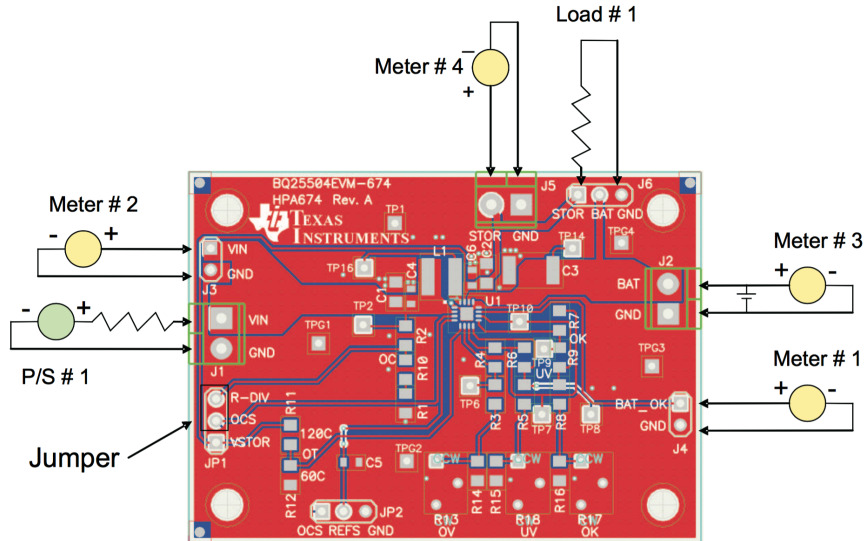


Figure 3.16: *bq25504 EVM* schematic

3.3.3 Storage element

Included as a part of the *bq25504 EVM*, the storage element has to be analyzed in detail because, depending on the used application and power source there are different options to select. The first constraint is based on the ability of the power source to provide enough voltage during a period of time to charge high capacity batteries or capacitors. In this project, the nano-quadcopter performances do not allow to charge this kind of storage elements in a small period of time. Thus, the storage element selection is reduced to batteries or capacitors up to 500 mF of capacity.

The total energy stored in a battery or capacitor is given by:

$$E = \frac{1}{2} CV^2 \quad (3.7)$$

where C is the capacitance of the storage element and V is the stored voltage. Imagine that the system consume 1 A and the storage element has a capacitance of 1 F and is charged with 1 V; assuming the following equations and doing some calculus,

$$t = \frac{E}{P}$$

$$P = VI$$

the system will provide this current consumption during 0.5 seconds.

By the previous considerations, it is possible to select the storage element used to run the application. The chosen supercapacitor is selected from *AVX BestCap*, and it has

140 mF of capacitance. This capacitance is adequate, taking into account the system performances. Its capacitance can provide peak currents of about milliamperes without any problem in a short period of time and still supplying voltage.

3.3.4 Application

Eventually, the definition of the used application to demonstrate the capability of the designed inductive transfer system is explained in this section. In a first instance, the purpose was to implement a low consumption sensor as a load. Usually, these sensors have a high constant consumption that prevents the battery last enough time. To solve this problem, it is used the *eZ430-RF2500*. This device is a wireless developing tool with an integrated temperature sensor. An *eZ430-RF2500T* target board is connected in the receiver and communicates with the other target board installed on a USB debugging interface to show the air temperature using the Sensor Monitor Visualizer Application provided by the manufacturer.

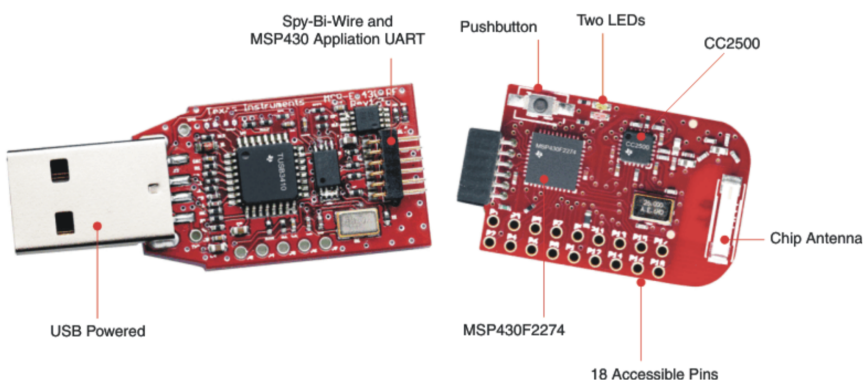


Figure 3.17: *eZ430-RF2500* debugging interface (left) and target board (right)

The main advantage is that the device consumption, when is in active mode, is about 270 μ A typically. The only drawback is that *eZ430-RF2500* needs 21.2 mA to communicate with the *CC2500* radio-frequency transceiver. This peak current can be easily supplied by the selected supercapacitor, mentioned in previous section. The device specifications are exposed in its datasheet, given in the Appendices.

3.3.5 Receiver Circuit Assembly

As the receiver is not constrained in mass, the assembling of this part has been done in a *stripboard*. Its relative small size allows to locate everywhere depending on the developed application. The resulting receiver circuit is exposed in Figure 3.18.

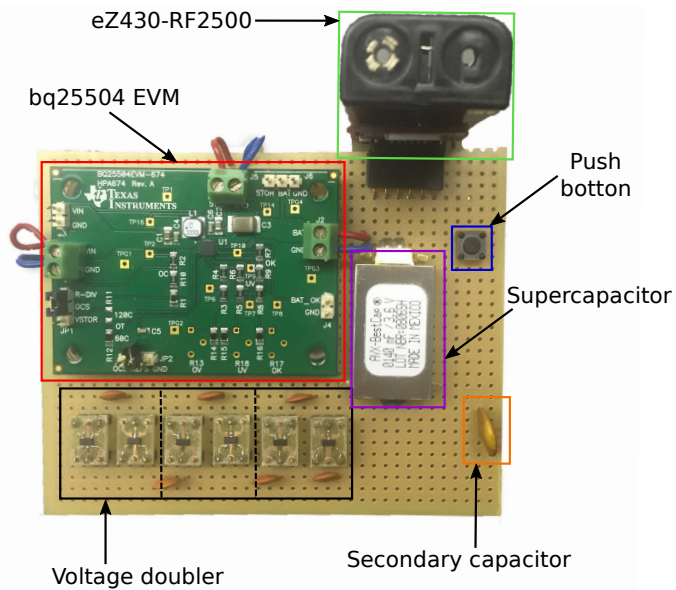


Figure 3.18: Receiver circuit

CHAPTER 4. EXPERIMENTAL RESULTS

In this chapter the model is *justified* using experimental information. Usually it is said to be the easiest part of model evaluation; whether it fits experimental measurements or not. Actually, it has been the most arduous task. Repetitive measures under different conditions, for each model, are carried out in order to validate the theoretical model.

Assumptions, simplifications and external factors made experimental results to separate from theoretical computations. Accepting this fact, the only intention is to get closer to resonant induction and be able to predict different behaviours depending on the input parameters selected.

4.1 Validations and Measurements

In this section has been evaluated separately the resonant inductive system and the final WPT system outfitted on the drone. While in the inductive system is intended to validate the model without paying attention to the result values, in the second part these results and overall performance are discussed.

4.1.1 Resistance Estimation

An accurate prediction of inductors' resistance is important when designing WPT systems, since it is some of the main factors that limit the power transfer capability and efficiency.

The resistance behaviour is constant until frequencies around 100 kHz. Then skin and proximity effects begin to increase the coil resistance value up to tens of ohms (C.1). The test frequency selected to compute the theoretical values is 1 MHz. The measures on the 8 test coils are performed by using an HP 4294A Precision Impedance Analyser (40 Hz - 110 MHz).

Coil model [-]	Measured resistance [Ω]	Calculated resistance (using 2.18) [Ω]	Relative error ϵ_1 [100%]
A_{Tx}	0.5639	0.6519	13.49
A_{Rx}	0.5916	0.6519	9.24
B_{Tx}	0.6071	0.6193	2.00
B_{Rx}	0.6380	0.6193	2.93
C_{Tx}	0.6704	0.6519	2.75
C_{Rx}	0.6286	0.6519	3.70
D_1	0.4485	0.2216	50.59
D_2	0.3368	0.1306	61.22

Table 4.1: Inductance calculation and measurement results

The results are in relatively good agreement with absolute errors smaller than 15% for

the 3 candidate models. However, the theoretical resistances for models D1 and D2 are far from reality. This could be explained by the presence of AC effects when increasing frequency, and so a wrong modeling of the wire due to the varnish insulation (Table 2.5).

4.1.2 Inductance Estimation

An accurate estimation of inductance is important because it is used to define the induction system model. It is also a vital parameter in tuning the resonant frequency of the WPT system. In Section 2.4.2 there are defined different equations which approximate multiple-layer air-core coils.

The theoretical computations are validated through individual measures performed on the 8 test coils using an HP 4294A Precision Impedance Analyser (40 Hz - 110 MHz). The experimental values of inductance are measured in the frequency range of 10 kHz to 20 MHz. It must be said that inductance values behind 15 MHz start to behave strangely.

Coil model [−]	Measured inductance [μH]	Calculated inductance (using 2.21) [μH]	Relative error ε ₁ [100%]	Calculated inductance (using 2.20) [μH]	Relative error ε ₂ [100%]
A_{Tx}	12.45	12.38	0.56	11.21	9.95
A_{Rx}	12.46	12.38	0.64	11.21	10.03
B_{Tx}	13.96	12.72	8.88	12.75	8.66
B_{Rx}	13.7	12.72	7.15	12.75	6.93
C_{Tx}	13.67	13.26	2.99	12.60	7.82
C_{Rx}	13.67	13.26	2.99	12.60	7.82
D_1	7.889	7.36	6.70	7.18	8.98
D_2	4.25	4.42	4.00	4.37	2.82

Table 4.2: Inductance calculation and measurement results

The results show good agreement with absolute errors smaller than 10% for Equation 2.21. The results of Equation 2.20 are also quite good specially for model D2. All these computations have been performed for a test frequency of 1 MHz. Note that inductance and resistance values are constant up to 500 kHz (see Appendix C.1).

4.1.3 Quality Factor

The experimental quality factor measurements of the coils reveal how *good* the coils are for transferring energy. From Figure 4.1 it can be observed that all coils have similar Q factors, and it increases with the frequency. Hence, we will try to work at the highest possible operating frequency, which is constrained by the Equation 2.43.

Table 4.3 exhibits the self-resonant frequency of models A, B and C, as well as their operating frequency.

The Q factor values of the table above are computed for the operating frequency. It would have not been *fair* to compute Q factor for the same frequency, owing to each coil has

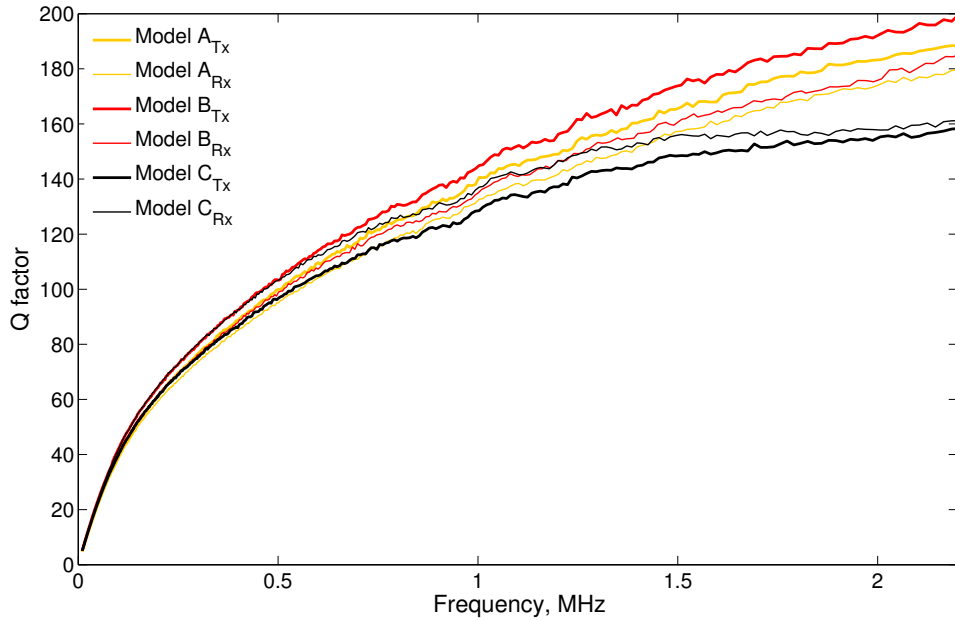


Figure 4.1: Experimental quality factor of model coils

Model	f_s	$f_{op(max)}$	Q factor
A	4.33 MHz	0.86 MHz	129
B	6.96 MHz	1.39 MHz	160
C	4.76 MHz	0.95 MHz	125

Table 4.3: Self-frequencies

its characteristic self-resonant frequency. The complete Q factor plot with respect to the frequency is presented in Appendix C.2, which includes the coil models D1 and D2.

4.1.4 Inductive System Performance

The inductive model verification and validation are performed in this part of the project. The obtained results are made with several laboratory measuring instruments that may influence in the experimental measurements. This involves the necessity of evaluate its influence in a detailed way to assure that the correct experimental value is measured.

4.1.4.1 Previous considerations

To make the analytical measurements of the resonant inductive system and compare it with the model, it is mandatory to drive this circuit with a sinusoidal voltage source. The chosen source is the *Agilent 33120A* waveform generator. This AC voltage source is selected to avoid the impedances and losses that can exist if the crystal oscillator is used as source (the overall transmission system), which its impedance and losses are more difficult to determine. Thus, the total impedance of the overall circuit depends on different stages.

Working with this waveform generator we ensure having a impedance determined by the manufacturer.

The output voltage rating of the *Agilent A33120A* is between 35.35 mV_{rms} to 7.071 V_{rms} and it has a fixed output impedance of 50 Ω. The first important point to be taken into account is that the default setting for the function generator is to display the desired voltage as though terminated into a 50 Ω load. As a consequence, whether the displayed voltage is set to 3.535 V_{rms}, the measured voltage at the output of the generator will be of 7.071 V_{rms}.

All voltage measurements are done with the *Agilent DSO3062A* oscilloscope and the *Agilent N2862A* probe. In this part appears the second and third important points to understand. The second one is related with the input resistance in parallel with the input capacitance of the oscilloscope probe. The problem appears when a capacitive component is measured. If this capacitance has its order of magnitude similar to the input capacitance of the oscilloscope probe (about 12 pF), the measurement may be erroneous because the input capacitance can not be negligible and they will be summed.

The last important consideration when a measurement is done is the called “ground effect”. This effect appears when the oscilloscope is used to measure the voltage drop across a circuit element, where the probe impedance is set in parallel with this component and forces to generate another reference of the ground. The following elements will be short circuited and the displayed value on the oscilloscope will be wrong. To solve this problem, floating oscilloscopes such as *Agilent U1604A* are used, allowing to cancel this “ground effect”.

4.1.4.2 Measurements methodology

Once the previous considerations are understood, the analytical measurements can be made. In this experiment exist four independent variables which condition the measures. These variables are the source voltage, the operating frequency, the distance and the load impedance. First of all, we set the AC voltage source in 1 V_{rms} displayed (2 V_{rms} measured). The selection of this output voltage is the one to ensure that the function generator can provide the necessary power to our system without any problem. In the case that the impedance becomes small, the output current will be limited, below its maximum, by the selected low level of voltage. The measurements are made with a sinusoidal wave for three different frequencies: 0.7 MHz, 1 MHz and 2 MHz. These frequencies are selected in order to compare the behavior of the system for different sinusoidal excitations. These selection of the voltage source and the frequency leaves two independent variables defined.

All measurements are done for SS and SP topologies for the primary and secondary coils of the same model, to simplify the comparison with the theoretical model. The optimal way to transfer energy is when the resonant frequency is the operating frequency, thus, compensation capacitors are determined depending on the operating frequency for each coil model. Two kinds of analysis are made: the efficiency and power dependence between the distance and the load impedance, the other two independent variables. This two analysis will allow us to verify the model equations for the energy transmission system, in terms of magnetic induction, and the power transferred to the secondary side, in terms of the optimal load that matches with the primary circuit.

The comparison between the real efficiency and output power with their respective theo-

retical values will allow us to validate the model. To perform that, first of all it is required to determine the input power. The calculation of the input power is done by computing the AC current flowing through the primary side of the core-less transformer and multiplying it by the source voltage. The calculation of an AC current is not a trivial task because typical multimeters can measure *RMS* magnitudes of AC waveforms up to 300 kHz approximately. The only option for computing the AC current is to place a small resistor¹ in series after the source voltage and measuring, with a floating oscilloscope, the dropped voltage in this resistor; using the Ohm's law it is possible to calculate the input current. The resistor value is set to 1 Ω.

Distance analysis are made by aligning the coils concentrically. The transmission range is set from 2.5 cm to 10 cm modifying the distance each 1.25 cm. Note that this range goes from the center of the primary coil to the center of the secondary one. The selected small amplitude voltage does not allow us to increment this range. The only parameter that is variable in this case is the distance, thus, it is necessary to fix the load impedance. As it is said in Section 2.5.2.5, the SS topology works better with small load impedances and the SP topology, with high load impedances. At the end of the Section 2.5.1 it was explained that maximum transferred power is when Z_R is equal to the primary circuit impedance. Knowing that this reflected impedance is dependent on the distance and the load impedance, for each distance will be a load impedance that maximizes this power. To simplify the measures, Z_L is fixed for SS and SP topologies with 75 Ω and 200 Ω respectively. In Figure 4.2(a) is exposed the analytical measuring procedure for a distance analysis.

The analysis with the load resistance are made by setting fixed the distance in 5 cm. For SS topology, the load is changed up to 100 Ω approximately and for SP topology, up to 7 kΩ. This procedure is shown in Figure 4.2(b), where the two coils are distanced 5 cm.

In Appendix E.4 it is demonstrated that an increment in R_x radius is preferred upon the same increment in T_x radius which was stated in Section 2.7. This means that larger receivers allow higher power levels for a certain distance.

4.1.4.3 Results

The obtained results for all coil models are exposed in Appendix E. The distance and load resistance analysis results are quite close to the theory. The differences are due to the tolerance of the laboratory measuring instruments used. Another factor that roughly affects to the comparison between the reality and the theory is the losses due to the transmission through the air, which is the main reason of having losses. Nevertheless, the tendency of the real measures is almost the same as theoretical values curves.

4.1.5 Overall System Performance

To complete the experimental results, the overall system performance has to be analyzed. As it has said in Chapter 3, the used coil model for the overall system is the Model C. Thus,

¹The small resistor up to 1 Ω is selected not to change the behavior of the system. Large resistors could be better for determining the dropped voltage and to compute the current in a more precise way, but they will change the measured values.

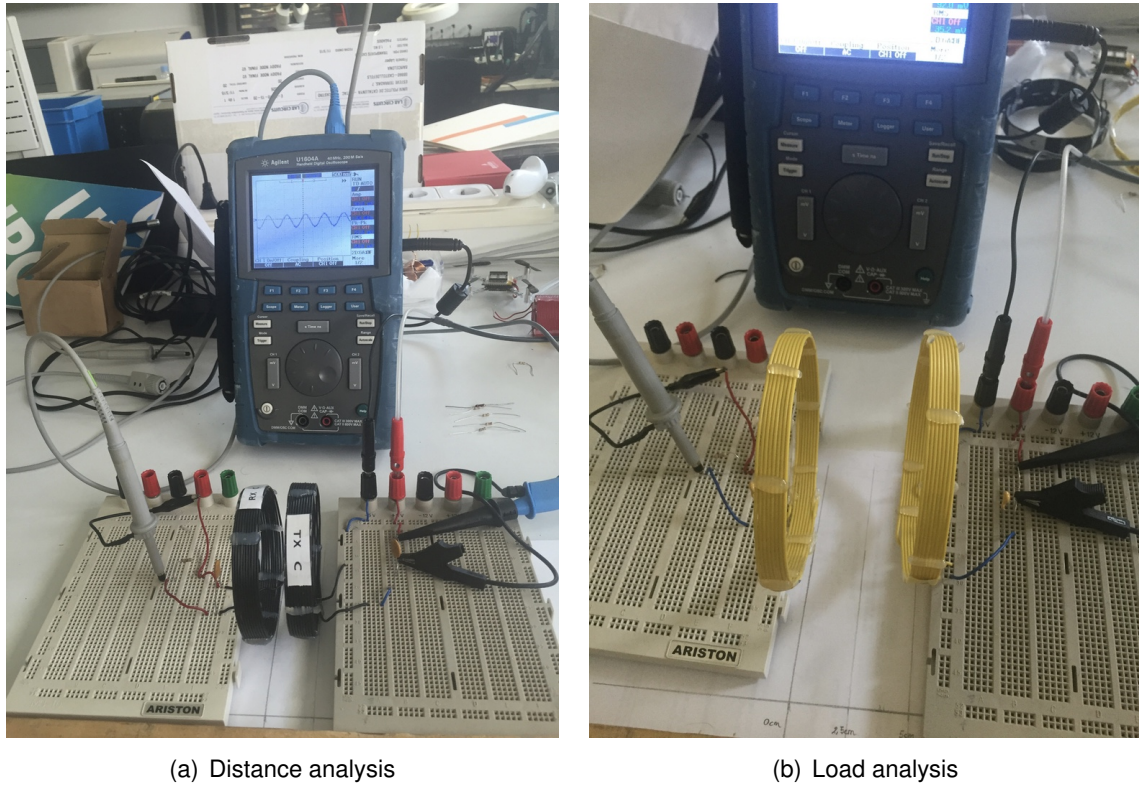


Figure 4.2: Measuring procedure

the experimental results are obtained by analyzing some interesting points corresponding to Model C performances.

The first test was to determine the autonomy of the nano-quadcopter battery using the transmitter circuit coupled to the receiver, and charging the super capacitor without the load installed. The methodology for this test was to put the nano-quadcopter at 2.5 cm from the receiving coil using the SS topology. The full charging of the super capacitor is reached at exactly 10 minutes with the nano-quadcopter battery without being discharged. As Figure 4.3 shows, the nano-quadcopter's battery is completely discharged after 16 minutes approximately. The blue dashed line indicates the voltage limit where the inductive system is turned off. This limit corresponds to the minimum voltage allowed by the regulator to boost the voltage level to 12 VDC. This voltage is experimentally selected to accomplish measurable power levels in the receiver, at a distance of 20 cm.

It has been proved the same test with the SP topology and the charge time is increased over 14 minutes. The conclusion of this fact is that the load impedance (that is difficult to determine in this part of the project) could be relatively small (above 50Ω). This means that the optimal topology to use is the SS compensation topology.

Once it has tested that the nano-quadcopter can charge the super capacitor, the same experiment is done by installing the eZ430-RF2500 target board. As it has expected, the system is not able to manage the charge of the super capacitor and to run the eZ430-RF2500 at the same time. The reason is that the CC2500 RF transceiver needs to communicate with the other target board, installed on a PC for running the Sensor Monitor Visualizer Application, consuming the 21.2 mA when the battery has the equivalent energy to this current. As a result, this sensor will not communicate to its receiver and the battery will not

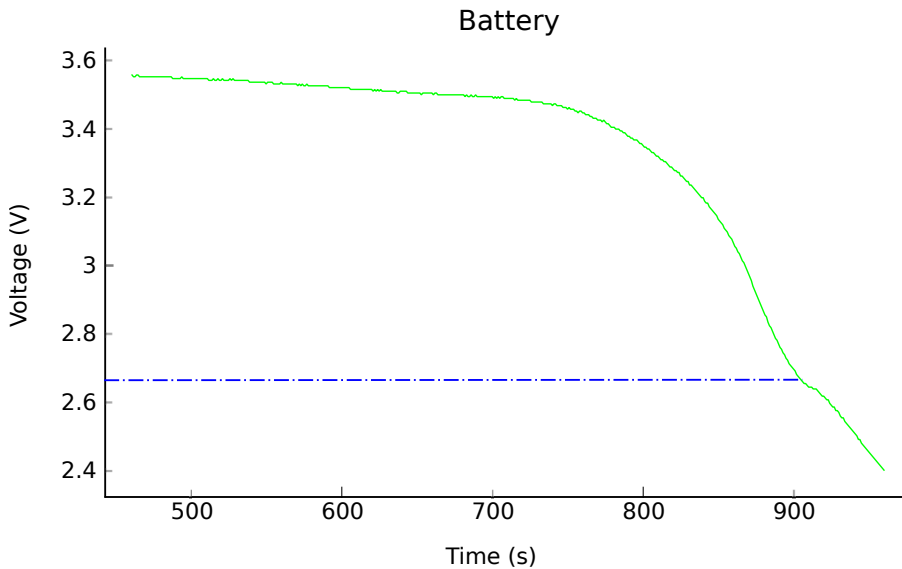


Figure 4.3: Nano-quadcopter's battery discharging profile

be charged; a voltage controlled switch (like a NMOS circuit) or a push button, such as in our case, has to be implemented.

The push button (see Figure 3.18) allows the nano-quadcopter to charge the battery and, when the battery is charged to the minimum voltage that can provide the enough energy for supply 21.2 mA, the push button can be triggered in order to feed the sensor. Figure 4.4 shows the realized experimental procedure for this section. In the figure it can be seen both the computer and the sensor target boards are displayed on the screen showing their temperature respectively.

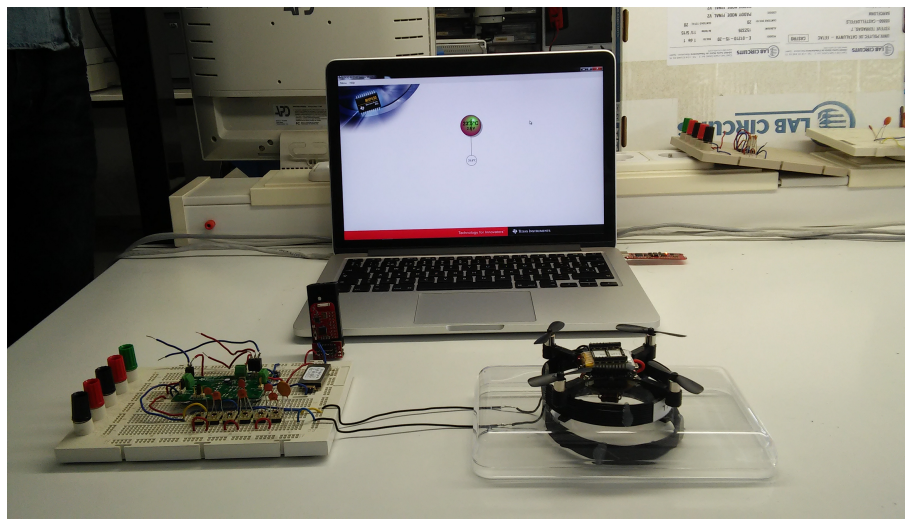


Figure 4.4: Overall system measurement.

Table 4.4 exhibits the comparison between the theoretical and analytical power consumption.

Source voltage	Theoretical current	Theoretical power	Consumed current	Consumed power
3.7 V	1.05 A	3.88 W	1.06 A	3.92 W

Table 4.4: Consumption comparison

CONCLUSIONS

In this project has been tested the viability to transport energy by using an inductive system mounted in a nano-quadcopter. The insertion of the drone allows to extend the number of induction applications, as well as provide the project with a differential regarding to other works until present.

To perform an accurate model, several theoretical electromagnetic principles are presented in Chapter 2. Firstly, it is discussed how resonance is created. This knowledge of resonance lead us to the *old*, because induction is more than a century old, and at the same time *new* way of transfer energy: the resonant induction. Since the *MIT* published in 2007 an article explaining the basis of resonant induction, several applications have been developing and commercialized. At the end of the Chapter, the multiple variables of the induction system and their effects are studied to predict the system's behaviour.

The constraints of weight and size of the nano-quadcopter complicates the design and assembly of the transmitter circuit. It is also important to select correctly the needed components, owing to multiple converter stages, a bad choice means to lose almost all the remaining circuit efficiency.

Using a restrictive drone, such as *Crazyflie* facilitate the design and implementation of the inductive system in bigger quadcopters. Then, it would be possible to carry bigger inductances, and consequently to increase the magnetic flux and power levels at the receiver side. Although is not the most efficiency way to increase the transfer distance, with larger drones it will be possible to place greater batteries, or maybe a unique battery reserved only for power transfer. However, future improvements lie in enhancing the overall system efficiency using computational coil designs. These designs, with higher Q factors, would be implemented by using PCB coils or special wires, like *Litz* wire, for instance.

The induction system meet the requirements in terms of performance, allowing to charge small batteries up to distances of 10 cm and a power level up to milliwatts. Depending on the desire application, the system can either power directly the sensor or power a battery. This last option is desired when the sensor requires a current peak which the inductive system can not provide. As a demonstrative application, the system charges a supercapacitor.

A future improvement could be the implementation of a PID controller to the *Crazyflie*. Large coil sizes difficult the maneuverability, and depending on the size make prevent to fly.

BIBLIOGRAPHY

- [1] H.H. Wu, A.P. Hu, P. Si, D. Budgett, C. Tung, and S. Malpas. A push-pull resonant converter with dual coils for transcutaneous energy transfer systems. In *Industrial Electronics and Applications, 2009. ICIEA 2009. 4th IEEE Conference on*, pages 1051–1056, May 2009. doi:10.1109/ICIEA.2009.5138362. 2, 32
- [2] *Wireless Safety*. EC-Council Press Series. Cengage Learning, 2009. URL: <https://books.google.es/books?id=Vsyyo94i5n8C>. 2
- [3] Pascal Meyer. *Modeling of Inductive Contactless Energy Transfer Systems*. PhD thesis, STI, Lausanne, 2012. doi:10.5075/epfl-thesis-5486. 2, 16, 20, 22, 25, 26, 30
- [4] Mark Roberti. The history of rfid technology. *RFID Journal*, 2005. 2
- [5] T. Sun, X. Xie, and Z. Wang. *Wireless Power Transfer for Medical Microsystems*. SpringerLink : Bücher. Springer, 2013. URL: https://books.google.es/books?id=kTA_AAAQBAJ. 2, 15, 16, 18, 30
- [6] E. Sazonov and M.R. Neuman. *Wearable Sensors: Fundamentals, Implementation and Applications*. Elsevier Science, 2014. URL: <https://books.google.es/books?id=wGJzAwAAQBAJ>. 3
- [7] Constantine A. Balanis. *Antenna Theory: Analysis and Design*. Wiley-Interscience, 2005. 3
- [8] Aristeidis Karalis, J.D. Joannopoulos, and Marin Soljačić. Efficient wireless non-radiative mid-range energy transfer. *Annals of Physics*, 323(1):34 – 48, 2008. January Special Issue 2008. URL: <http://www.sciencedirect.com/science/article/pii/S0003491607000619>, doi:<http://dx.doi.org/10.1016/j.aop.2007.04.017>. 4, 31
- [9] *MIT Tech Talk*. MIT, 13/06/2007. URL: <http://news.mit.edu/2007/techtalk51-30.pdf>. 4, 13
- [10] P.A. Tipler and G. Mosca. *Physics for Scientists and Engineers*. W. H. Freeman, 2007. URL: <https://books.google.es/books?id=paUkAAAAQBAJ>. 7, 8, 10
- [11] Q and bandwidth of a resonant circuit, 2015. URL: <http://www.allaboutcircuits.com/textbook/alternating-current/chpt-6/q-and-bandwidth-resonant-circuit/> [cited 12/09/2015]. 14
- [12] Power losses in wound components, August 2008. URL: http://info.ee.surrey.ac.uk/Workshop/advice/coils/power_loss.html [cited 16/01/2016]. 15
- [13] Ban-Leong Ooi, Dao-Xian Xu, Pang-Shyan Kooi, and Fu-Jiang Lin. An improved prediction of series resistance in spiral inductor modeling with eddy-current effect. *Microwave Theory and Techniques, IEEE Transactions on*, 50(9):2202–2206, Sep 2002. doi:10.1109/TMTT.2002.802337. 15

- [14] B.L. Cannon, J.F. Hoburg, D.D. Stancil, and S.C. Goldstein. Magnetic resonant coupling as a potential means for wireless power transfer to multiple small receivers. *Power Electronics, IEEE Transactions on*, 24(7):1819–1825, July 2009. doi:10.1109/TPEL.2009.2017195. 16
- [15] Skin depth, 2015. URL: <http://www.microwaves101.com/encyclopedias/skin-depth> [cited 05/01/2016]. 17
- [16] Jungsuk Kim, Hyunchul Kim, and K.D. Pedrotti. Power-efficient inductive link optimization for implantable systems. In *Radio and Wireless Symposium (RWS), 2011 IEEE*, pages 418–421, Jan 2011. doi:10.1109/RWS.2011.5725496. 17
- [17] Chunbo Zhu, Kai Liu, Chunlai Yu, Ma Rui, and Hexiao Cheng. Simulation and experimental analysis on wireless energy transfer based on magnetic resonances. In *Vehicle Power and Propulsion Conference, 2008. VPPC '08. IEEE*, pages 1–4, Sept 2008. doi:10.1109/VPPC.2008.4677400. 18, 33
- [18] B. Griffin and C. Detweiler. Resonant wireless power transfer to ground sensors from a uav. In *Robotics and Automation (ICRA), 2012 IEEE International Conference on*, pages 2660–2665, May 2012. doi:10.1109/ICRA.2012.6225205. 18, 33
- [19] Shouguo Fu, Kan Liu, Xinyu Zhang, An Ji, and Changsheng Xie. Design of wireless power driving and controlling system for electrically driving liquid crystal micro-lens array, 2011. URL: <http://dx.doi.org/10.1117/12.901881>, doi:10.1117/12.901881. 18
- [20] H.A. Wheeler. Simple inductance formulas for radio coils. *Radio Engineers, Proceedings of the Institute of*, 16(10):1398–1400, Oct 1928. doi:10.1109/JRPROC.1928.221309. 18
- [21] W.K. Chen. *The Circuits and Filters Handbook, Second Edition*. Circuits & Filters Handbook 3e. CRC Press, 2002. URL: <https://books.google.es/books?id=0SPNBQAAQBAJ>. 18, 35
- [22] CLW Christoph Sonntag. Design of a variable-phase contactless energy transfer platform using air-cored planar inductor technology : Contactless energy transfer platform using air-cored planar inductors. Master's thesis, Eindhoven University of Technology, 2010. URL: <https://pure.tue.nl/ws/files/3379291/201010122.pdf>, doi:<http://dx.doi.org/10.6100/IR669103>. 18, 32
- [23] H. Hoang and F. Bien. *Maximizing Efficiency of Electromagnetic Resonance Wireless Power Transmission Systems with Adaptive Circuits*. INTECH Open Access Publisher, 2012. URL: <https://books.google.es/books?id=m4zSoAEACAAJ>. 20
- [24] Dan Jiang, Yong Yang, Fuxin Liu, Xinbo Ruan, and Chenghua Wang. Modeling and investigation of magnetically coupled resonant wireless power transfer system with varying spatial scales. In *Energy Conversion Congress and Exposition (ECCE), 2015 IEEE*, pages 2269–2274, Sept 2015. doi:10.1109/ECCE.2015.7309979. 23
- [25] Venugopal Prasanth. Wireless power transfer for e-mobility. Master's thesis, TU Delft, Delft University of Technology, 2012. URL: http://repository.tudelft.nl/assets/uuid:38f16698-0567-4ac3-8e25-06c3971383a4/Venugopal_Prasanth_Thesis.pdf. 26

- [26] S. Jalali Mazlouman, A. Mahanfar, and B. Kaminska. Mid-range wireless energy transfer using inductive resonance for wireless sensors. In *Computer Design, 2009. ICCD 2009. IEEE International Conference on*, pages 517–522, Oct 2009. doi: 10.1109/ICCD.2009.5413106. 30
- [27] The wireless power consortium, 2015. URL: <http://www.wirelesspowerconsortium.com/> [cited 23/12/2015]. 30
- [28] Byungcho Choi, Jaehyun Nho, Honnyong Cha, Taeyoung Ahn, and B. Choi. Design and implementation of low-profile contactless battery charger using planar printed circuit board windings as energy transfer device. *Industrial Electronics, IEEE Transactions on*, 51(1):140–147, Feb 2004. doi:10.1109/TIE.2003.822039. 32
- [29] N. Phokaphan, K. Choeisai, K. Noguchi, T. Araki, K. Kusaka, K. Orikawa, and J.-I. Itoh. Wireless power transfer based on mhz inverter through pcb antenna. In *Future Energy Electronics Conference (IFEEC), 2013 1st International*, pages 126–130, Nov 2013. doi:10.1109/IFEEC.2013.6687491. 32
- [30] S. Aldhaher, P.C.-K. Luk, and J.F. Whidborne. Electronic tuning of misaligned coils in wireless power transfer systems. *Power Electronics, IEEE Transactions on*, 29(11):5975–5982, Nov 2014. doi:10.1109/TPEL.2014.2297993. 33
- [31] R. Bosshard, J. Muhlethaler, J.W. Kolar, and I. Stevanovic. Optimized magnetic design for inductive power transfer coils. In *Applied Power Electronics Conference and Exposition (APEC), 2013 Twenty-Eighth Annual IEEE*, pages 1812–1819, March 2013. doi:10.1109/APEC.2013.6520541. 33, 36
- [32] F.E. Terman. *Radio engineer's handbook*. McGraw-Hill Book Company, inc., 1943. URL: <https://books.google.co.uk/books?id=b7Q8AAAAIAAJ>. 34
- [33] Wenshan Hu, Hong Zhou, Qijun Deng, and Xingran Gao. Optimization algorithm and practical implementation for 2-coil wireless power transfer systems. In *American Control Conference (ACC), 2014*, pages 4330–4335, June 2014. doi:10.1109/ACC.2014.6858998. 36
- [34] Bitcraze. Crazyfile 2.0, 2016. URL: <https://www.bitcraze.io/crazyfile-2/> [cited 02/12/2015]. 37, 44
- [35] Bitcraze repositories. URL: <https://github.com/bitcraze> [cited 17/11/2015]. 42
- [36] Battery University. Basics about discharging, 2003. URL: http://batteryuniversity.com/learn/article/discharge_methods [cited 24/01/2016]. 44, 45
- [37] Steven Keeping. Understanding the advantages and disadvantages of linear regulators. URL: <http://www.digikey.com/en/articles/techzone/2012/may/understanding-the-advantages-and-disadvantages-of-linear-regulators> [cited 02/02/2016]. 45
- [38] Quartz crystal oscillators, 2016. URL: <http://www.electronics-tutorials.ws/oscillator/crystal.html> [cited 26/01/2016]. 46

- [39] Daniel Bolaños. Introducción a osciladores. Technical report. URL: <http://www.bolanosdj.com.ar/TEORIA/OSCILADORES1.PDF>. 47
- [40] Thomas Steven Salter. *Low Power Smartdust Receiver with Novel Applications and Improvements of an RF Power Harvesting Circuit*. PhD thesis, University of Maryland (College Park, Md.), 2009. URL: <http://hdl.handle.net/1903/9104>. 51
- [41] Chandan Kumar Chakrabarty Kavuri Kasi Annapurna Devi, Norashidah Md. Din. *Optimization of the Voltage Doubler Stages in an RF-DC Convertor Module for Energy Harvesting*. PhD thesis. [doi:10.4236/cs.2012.33030](https://doi.org/10.4236/cs.2012.33030). 51

APPENDICES

APPENDIX A. INDUCTANCE CHARACTERIZATION

A.1 Inductance Estimation Table

D/l	K	D/l	K	D/l	K	D/l	K
0.02	0.1957	0.32	2.769	0.80	5.803	2.20	10.93
0.04	0.3882	0.34	2.919	0.85	6.063	2.40	11.41
0.06	0.5776	0.36	3.067	0.90	6.171	2.60	12.01
0.08	0.7643	0.38	3.212	0.95	6.559	2.80	12.30
0.10	0.9465	0.40	3.355	1.00	6.795	3.00	12.71
0.12	1.126	0.42	3.497	1.10	7.244	3.50	13.63
0.14	1.303	0.44	3.635	1.20	7.670	4.00	14.43
0.16	1.477	0.46	3.771	1.30	8.060	4.50	15.14
0.18	1.648	0.48	3.905	1.40	8.453	5.00	15.78
0.20	1.817	0.50	4.039	1.50	8.811	6.00	16.90
0.22	1.982	0.55	4.358	1.60	9.154	7.00	17.85
0.24	2.144	0.60	4.668	1.70	9.480	8.00	18.68
0.26	2.305	0.65	4.969	1.80	9.569	9.00	19.41
0.28	2.406	0.70	5.256	1.90	10.09	10.00	20.07
0.30	2.616	0.75	5.535	2.00	10.37	12.00	21.21

Table A.1: Coefficient K

A.2 Equivalent coil impedance

The impedance of the coil is defined as follows:

$$Z = \left(j\omega C_{par} + \frac{1}{R + j\omega L} \right)^{-1} \quad (\text{A.1})$$

by developing the equation, this impedance can be separated into a real and an imaginary term,

$$\Re Z = \frac{R}{(\omega R C_{par})^2 + (1 - \omega^2 L C_{par})^2} \quad (\text{A.2})$$

$$\Im Z = \frac{\omega L - \omega R^2 C - \omega^3 L^2 C_{par}}{(1 - \omega^2 L C_{par})^2 + (\omega R C_{par})^2} \quad (\text{A.3})$$

APPENDIX B. MODEL EQUATIONS

B.1 Secondary capacitor in series

By adding a capacitor in series in the secondary side, there is a notable different expressions for Z_2 and Z_R . Z_R has a capacitive reactance that prevents to transfer the maximum power to the secondary.

$$Z_2 = R_2 + R_L + j\omega L_2 - j \frac{1}{\omega C_2} \quad (\text{B.1})$$

$$Z_R = \frac{(R_2 + R_L)\omega^4 L_2^2 C_2^2}{(R_2 + R_L)^2 \omega^2 C_2^2 + (\omega^2 L_2 C_2 - 1)^2} - j \frac{\omega^3 M^2 C_2 (\omega^2 L_2 C_2 - 1)}{(R_2 + R_L)^2 \omega^2 C_2^2 + (\omega^2 L_2 C_2 - 1)^2} \quad (\text{B.2})$$

When the operating frequency is the resonance frequency ω_0 , obtained by using the Equation 2.11, the imaginary part of Z_R , that is a source of additional losses, is canceled and it will only remain its real part. Thus, the power transferred to the receiving circuit becomes only active power, and as a result, the consumable power. A simpler equation of Z_R is obtained which only depends on R_L if the distance is fixed, allowing to match this impedance with the primary circuit.

$$Z_R = \frac{\omega_0^2 M^2}{R_2 + R_L} \quad (\text{B.3})$$

B.2 Secondary capacitor in parallel

The same steps as above are followed for obtaining the impedances Z_2 and Z_R when the secondary capacitor is placed in parallel:

$$Z_2 = R_2 + j\omega L_2 + \frac{1}{\frac{1}{R_L} + j\omega C_2} \quad (\text{B.4})$$

$$Z_R = \frac{\omega^2 M^2 (1 + \omega^2 L_2^2 R_L^2) (R_2 + R_L + \omega^2 L_2 C_2 R_L)}{(R_2 + R_L + \omega^2 L_2 C_2 R_L)^2 + (\omega L_2 - \omega C_2 R_L R_2 - \omega C_2 R_L^2)^2} \\ - j \frac{\omega^2 M^2 (1 + \omega^2 L_2^2 R_L^2) (\omega L_2 - \omega C_2 R_L R_2 - \omega C_2 R_L^2)}{(R_2 + R_L + \omega^2 L_2 C_2 R_L)^2 + (\omega L_2 - \omega C_2 R_L R_2 - \omega C_2 R_L^2)^2} \quad (\text{B.5})$$

In this case, Z_R shows also a capacitive reactance that has to be avoided to transfer the maximum power. If we work at resonance frequency ω_0 , this reactance still remains:

$$Z_R = \frac{\omega_0^2 M^2 (1 + \omega_0^2 L_2^2 R_L^2) (R_2 + 2R_L)}{(R_2 + 2R_L)^2 + (\omega_0 L_2 - \frac{R_L R_2}{\omega_0 L_2} - \frac{R_L^2}{\omega_0 L_2})^2} \\ - j \frac{\omega_0^2 M^2 (1 + \omega_0^2 L_2^2 R_L^2) (\omega_0 L_2 - \frac{R_L R_2}{\omega_0 L_2} - \frac{R_L^2}{\omega_0 L_2})}{(R_2 + 2R_L)^2 + (\omega_0 L_2 - \frac{R_L R_2}{\omega_0 L_2} - \frac{R_L^2}{\omega_0 L_2})^2} \quad (B.6)$$

The solution is to select a capacitance value able to delete the imaginary part of the Equation B.5. A drawback of this option is the dependence of this capacitor on the load and that the system will not oscillate at the resonance frequency in the secondary side:

$$C_2 = \frac{L_2}{R_L} \frac{1}{(R_2 + R_L)} \quad (B.7)$$

B.3 Primary capacitor in series

The goal of the secondary capacitor was to cancel the imaginary part of the reflected impedance and the primary capacitor had a similar objective, that is to cancel the inductance of the coil. In a series compensated primary that works at resonance frequency, the imaginary part is fully deleted. The total impedance seen by the voltage source Z_{eq} has the following expression:

$$Z_{eq} = R_1 + j\omega L_1 - j \frac{1}{\omega C_1} + Z_R \quad (B.8)$$

At resonance frequency ω_0 , the imaginary part of Z_{eq} is canceled and this impedance becomes dependent only on the secondary circuit expressed in Z_R .

$$Z_{eq} = R_1 + Z_R \quad (B.9)$$

B.4 Primary capacitor in parallel

When the primary capacitor is placed in parallel, the total impedance Z_{eq} is given by:

$$Z_{eq} = \frac{1}{j\omega C_1 + \frac{1}{R_1 + j\omega L_1 + Z_R}}$$

$$Z_{eq} = \frac{R_1 + Z_R}{(1 - \omega^2 C_1 L_1)^2 + \omega^2 C_1^2 (R_1 + Z_R)^2} - j \frac{\omega C_1 (R_1 + Z_R)^2 - \omega L_1 (1 - \omega^2 C_1 L_1)}{(1 - \omega^2 C_1 L_1)^2 + \omega^2 C_1^2 (R_1 + Z_R)^2} \quad (B.10)$$

When the operating frequency is the resonance frequency ω_0 , Z_{eq} becomes as it is shown below.

$$Z_{eq} = \frac{\omega_0^2 L_1^4}{R_1 + Z_R} - j\omega_0 L_1^3 \quad (\text{B.11})$$

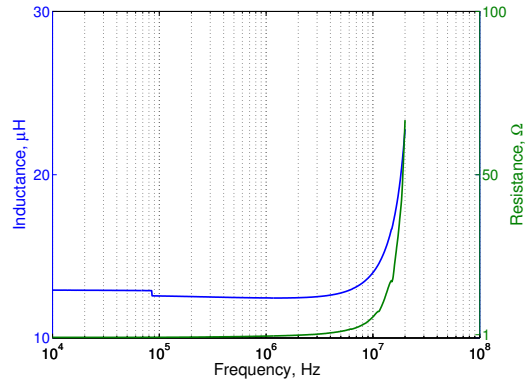
Note that as in case of the secondary capacitor in parallel, the reactance still remains and the solution could also be to select a capacitor that cancels the imaginary part of the Equation B.10.

$$C_1 = \frac{L_1}{(R_1 + Z_R)^2 + \omega_0^2 L_1^2} \quad (\text{B.12})$$

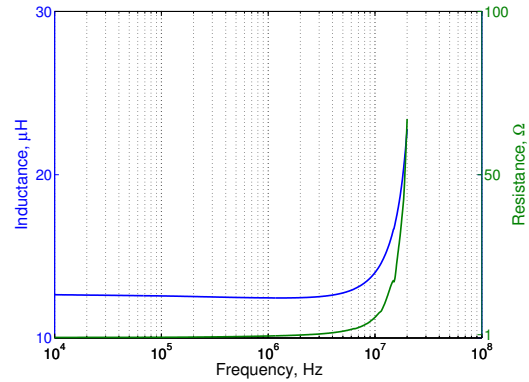
Now, this capacitor depends on the frequency and the reflected impedance which is dependent on the topology used in the secondary, the mutual inductance and the load resistance.

APPENDIX C. COILS EXPERIMENTAL RESULTS

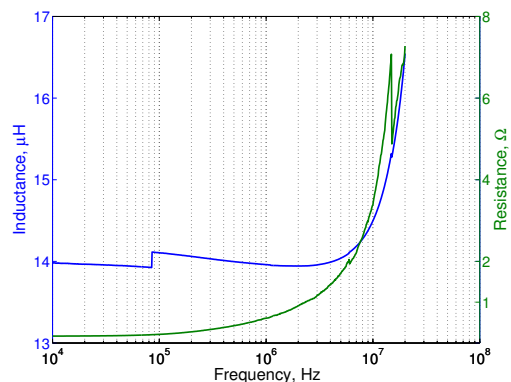
C.1 Inductance and Resistance



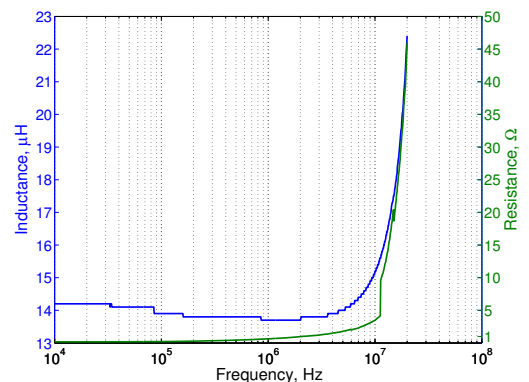
(a) Model A transmitter



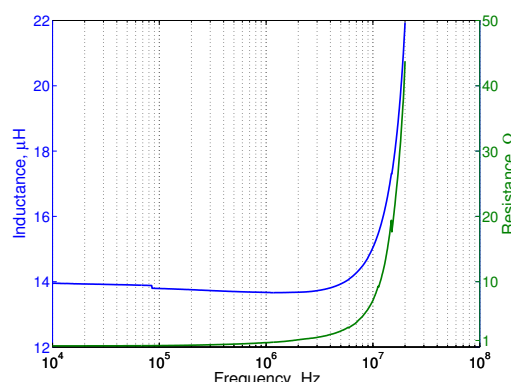
(b) Model A receiver



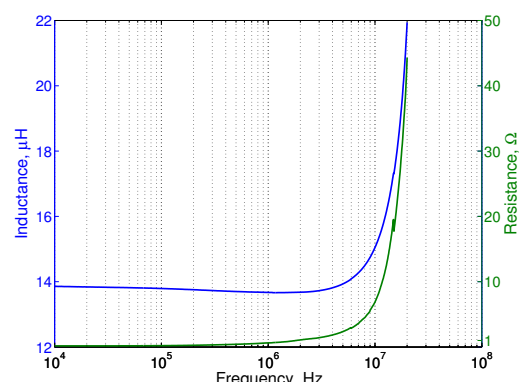
(c) Model B transmitter



(d) Model B receiver



(e) Model C transmitter



(f) Model C receiver

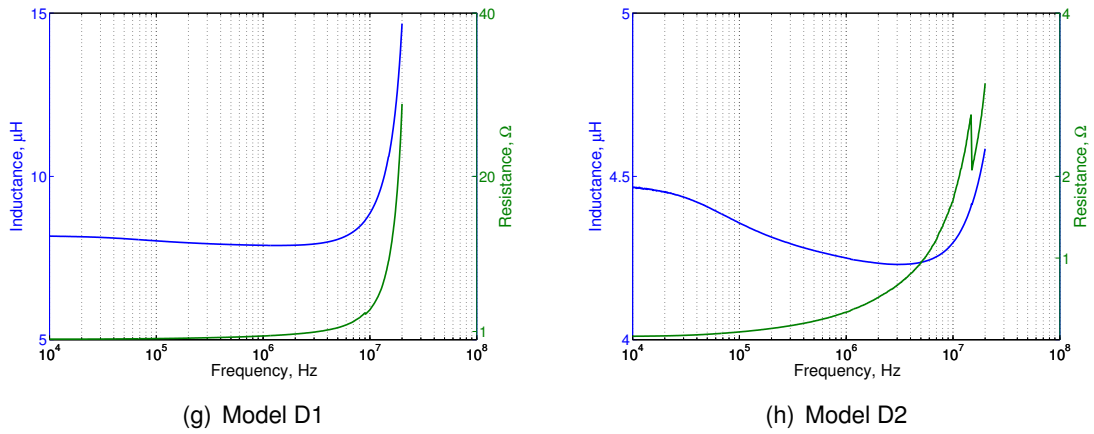


Figure C.1: Inductance and resistance w.r.t. frequency

C.2 Quality Factor

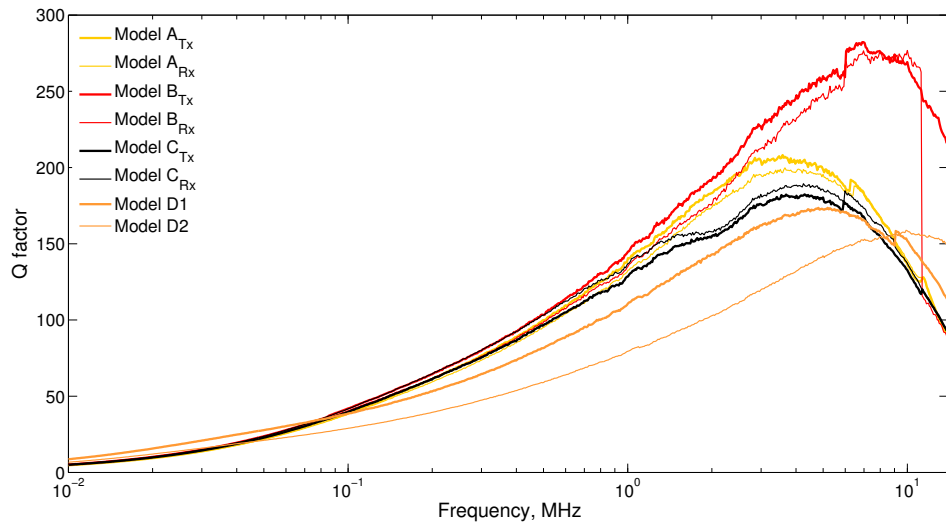


Figure C.2: Experimental quality factor

APPENDIX D. CIRCUIT SCHEMATICS

D.1 Voltage Regulator

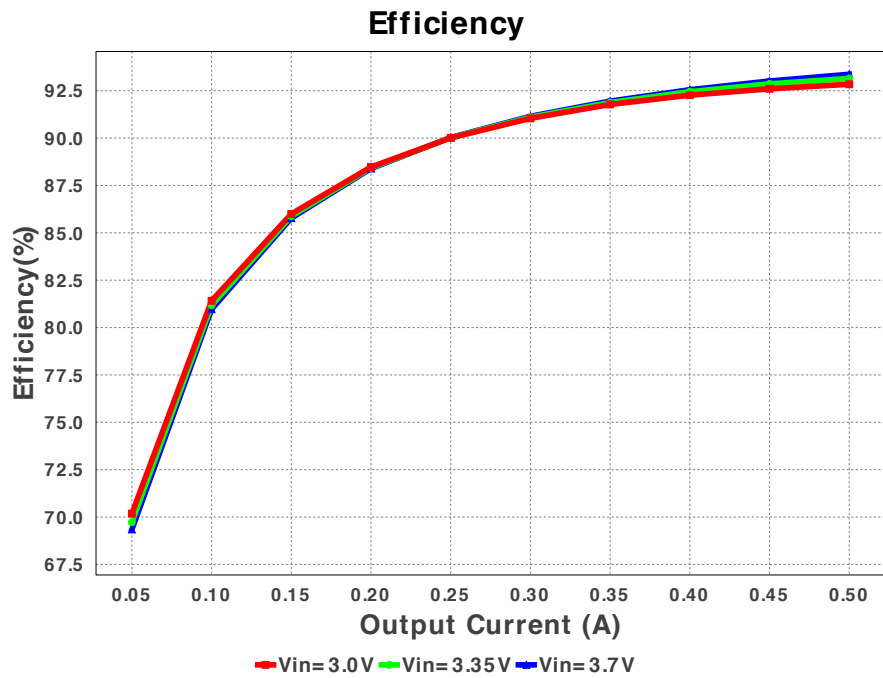


Figure D.1: Efficiency w.r.t. output current

D.2 Power Driver

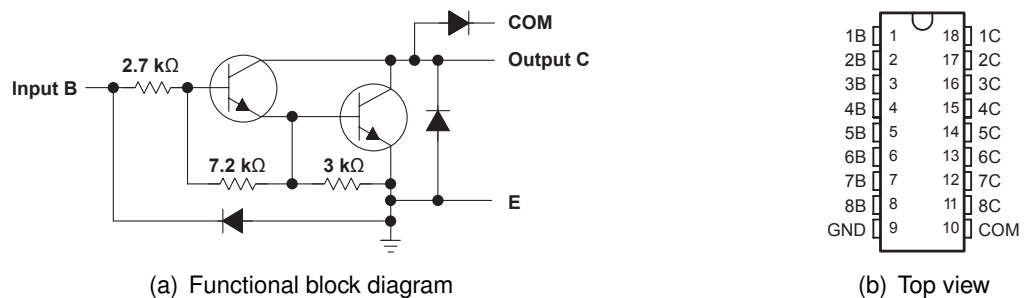


Figure D.2: ULN2803 Darlington driver

D.3 Transmitter

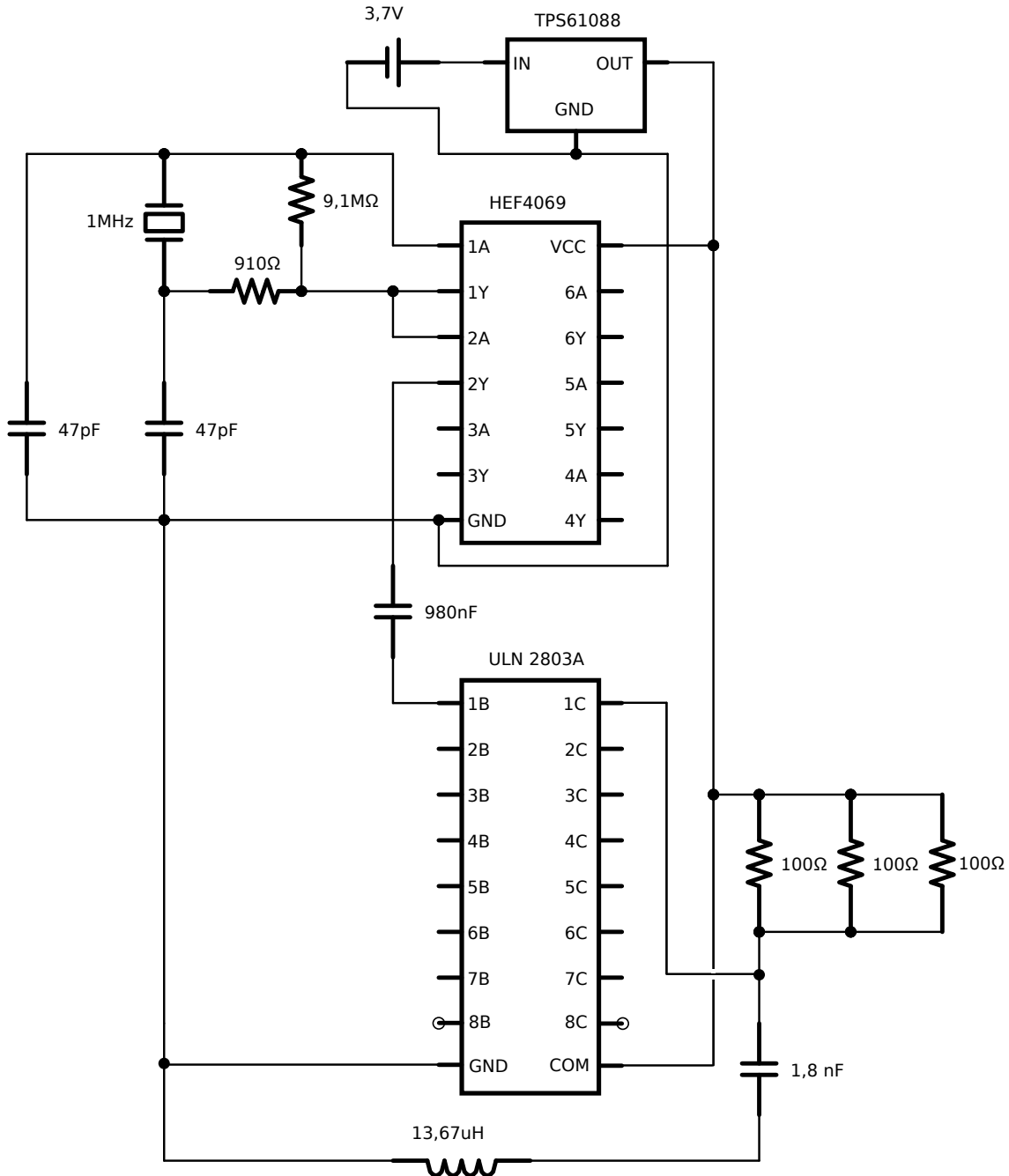


Figure D.3: Transmitter circuit schematic

D.4 Receiver

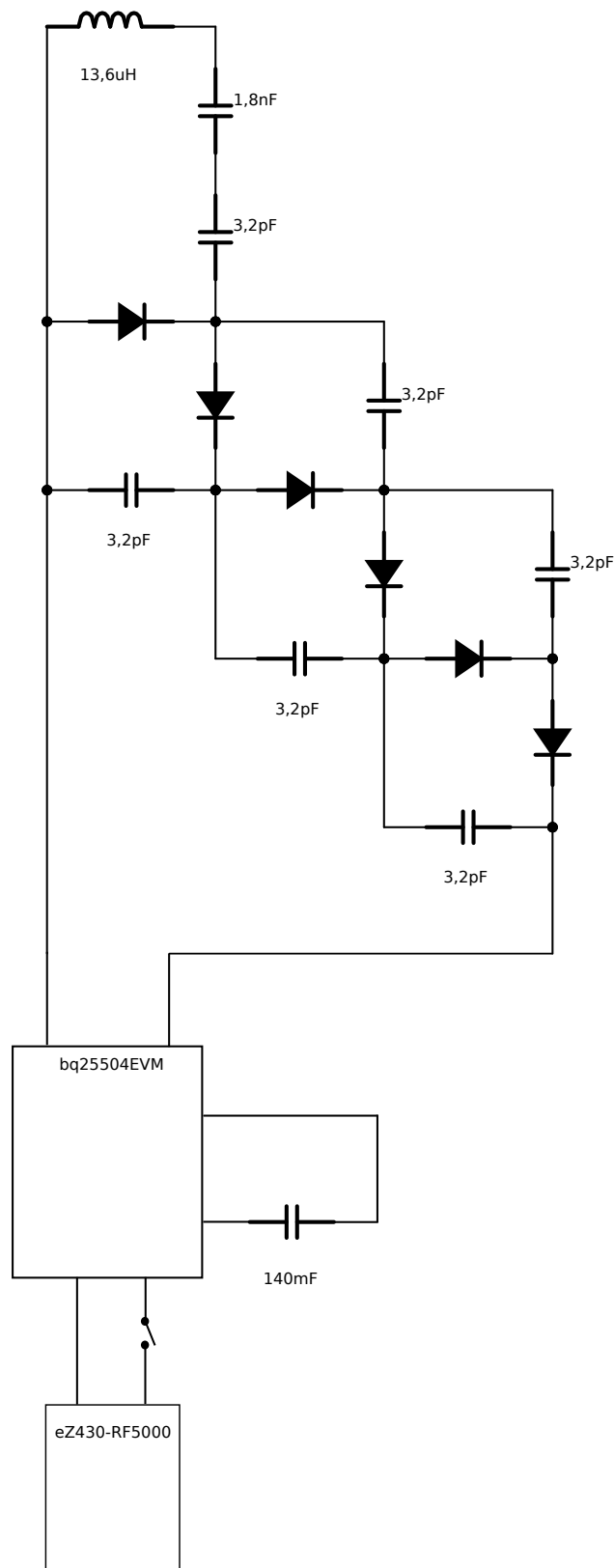


Figure D.4: Receiver circuit schematic

APPENDIX E. EXPERIMENTAL RESULTS

E.1 Model A

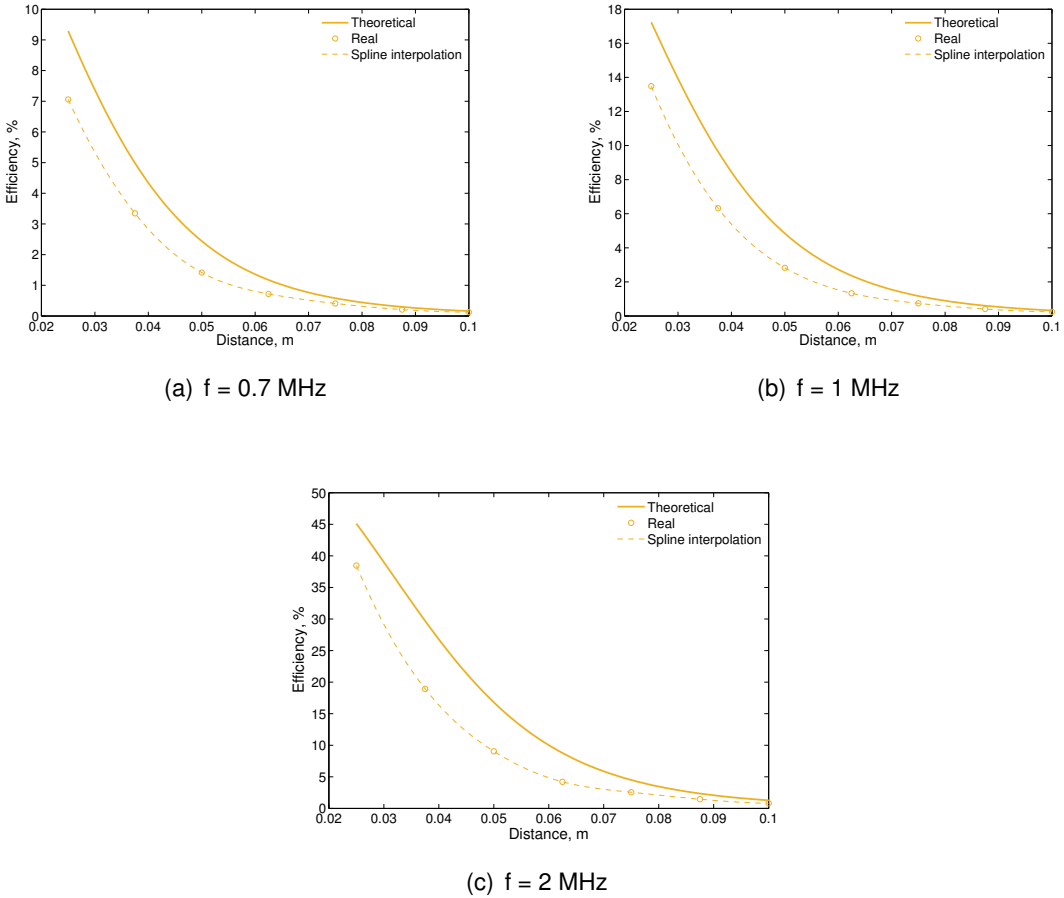
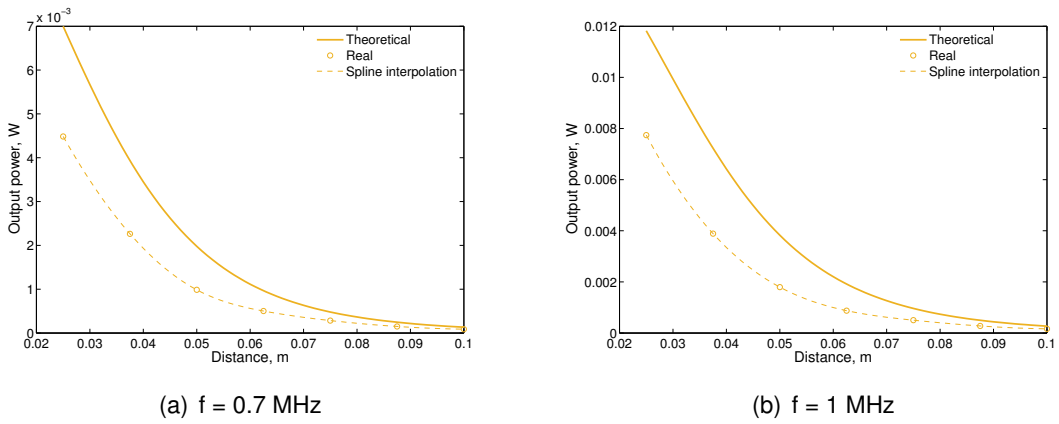
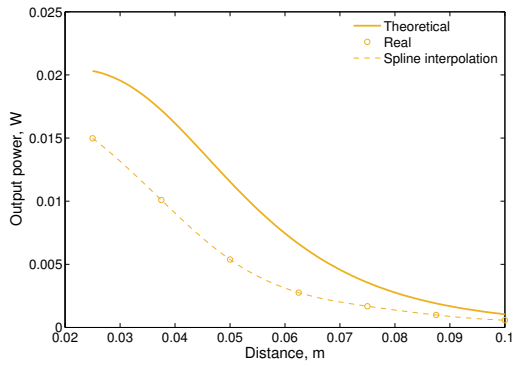


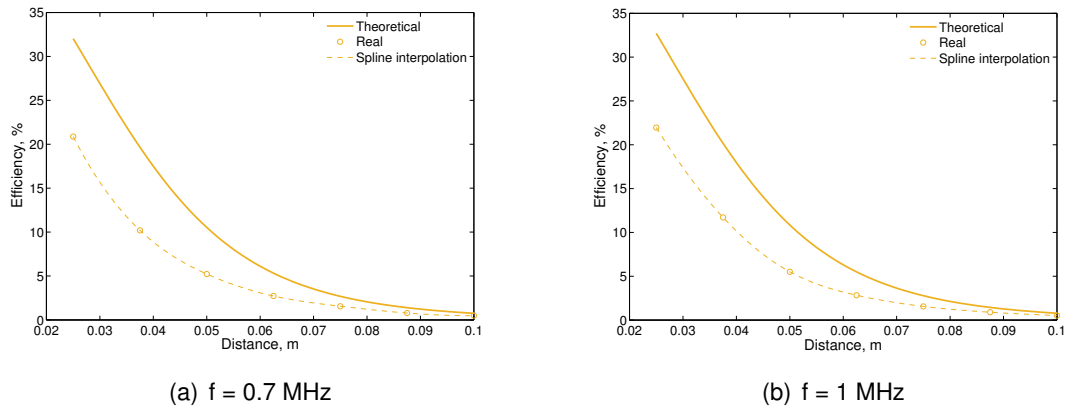
Figure E.1: Efficiency w.r.t. distance for SS topology





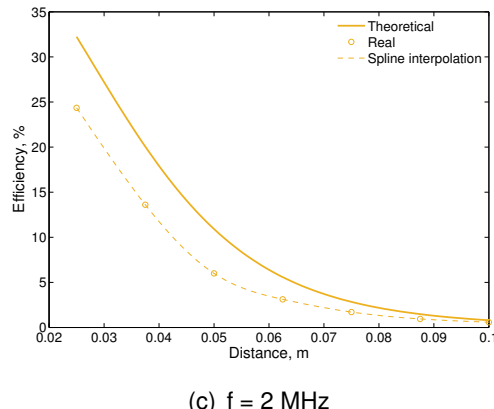
(c) $f = 2 \text{ MHz}$

Figure E.2: Output power w.r.t. distance for SS topology



(a) $f = 0.7 \text{ MHz}$

(b) $f = 1 \text{ MHz}$



(c) $f = 2 \text{ MHz}$

Figure E.3: Efficiency w.r.t. distance for SP topology

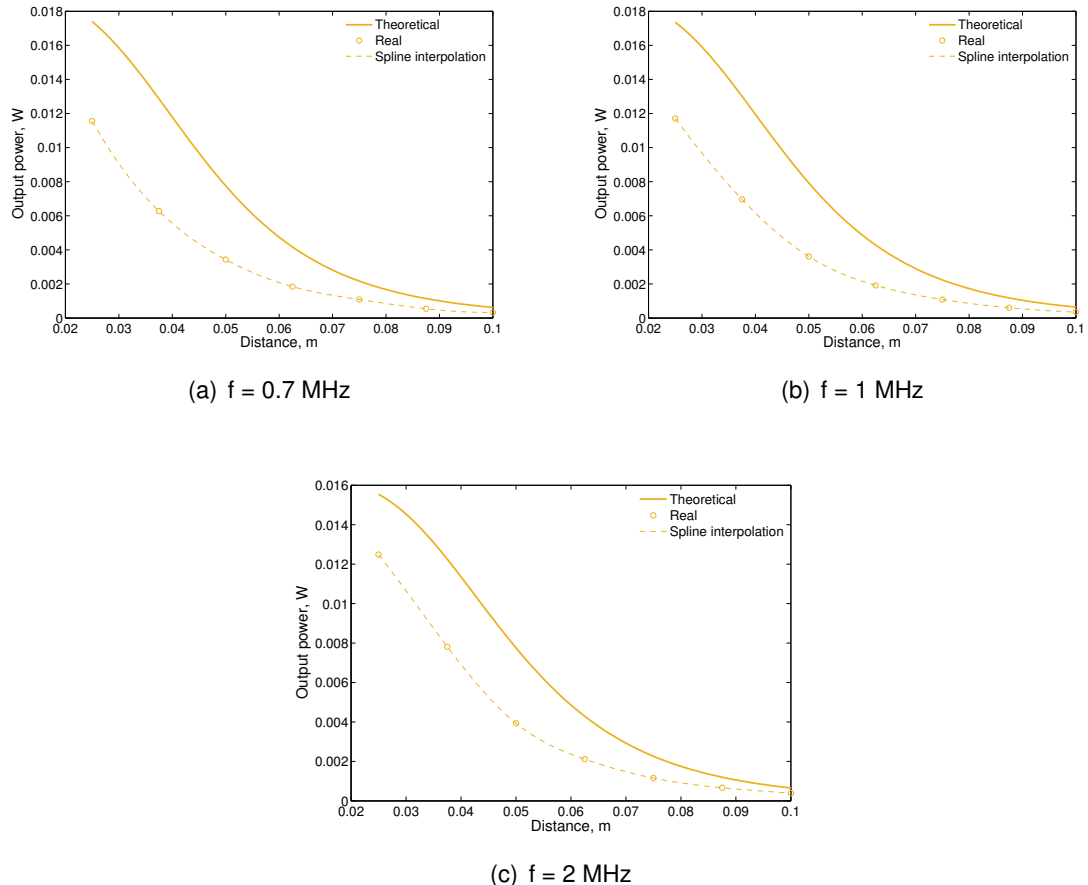
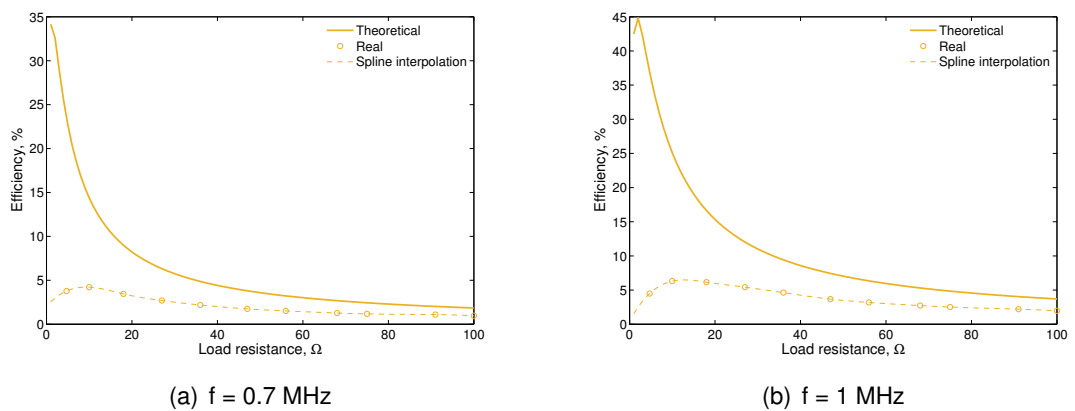
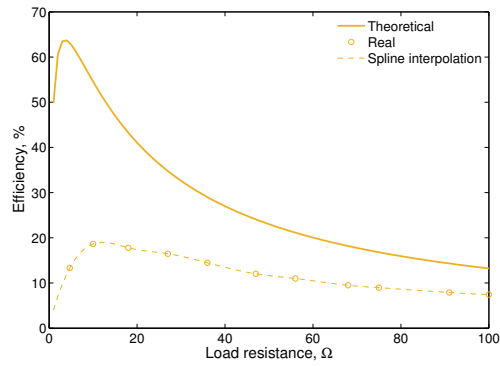


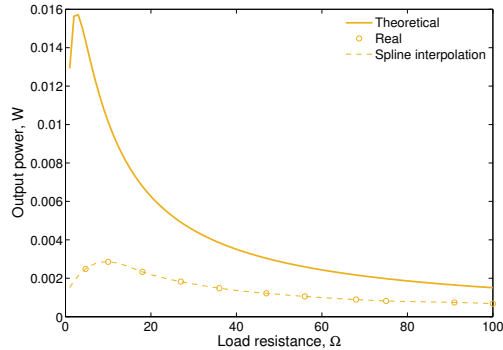
Figure E.4: Output power w.r.t. distance for SP topology



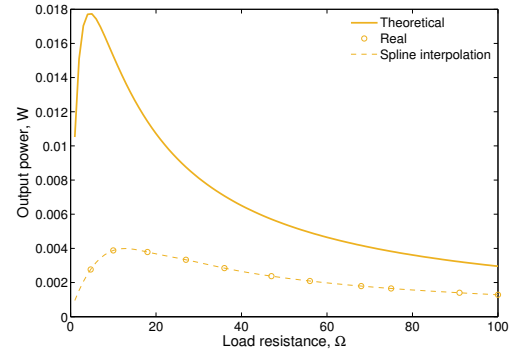


(c) $f = 2 \text{ MHz}$

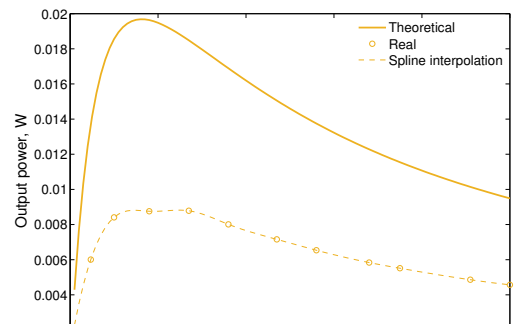
Figure E.5: Efficiency w.r.t. load resistance for SS topology



(a) $f = 0.7 \text{ MHz}$

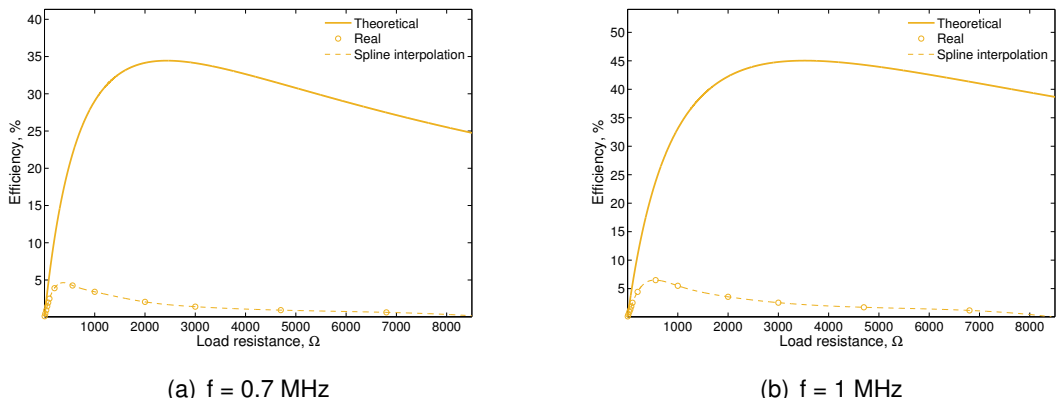
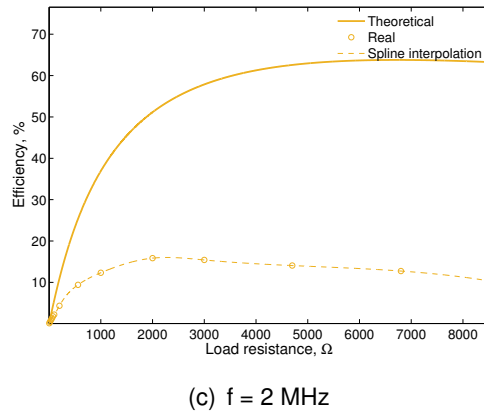
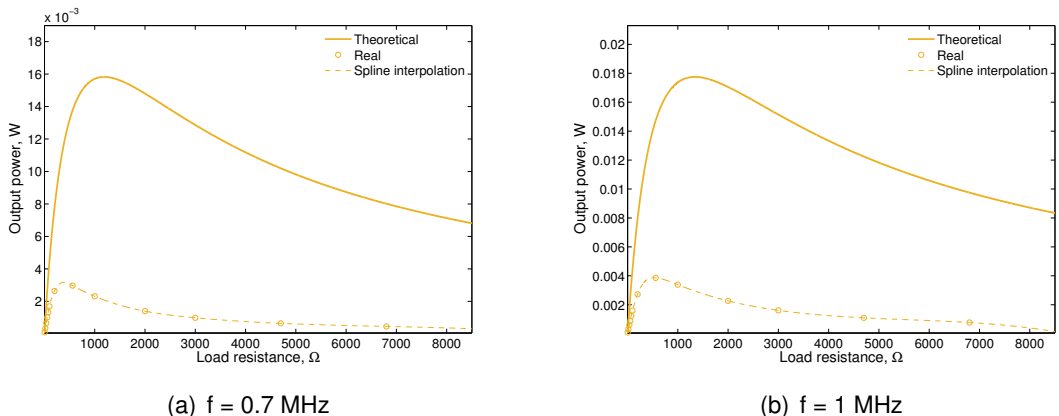


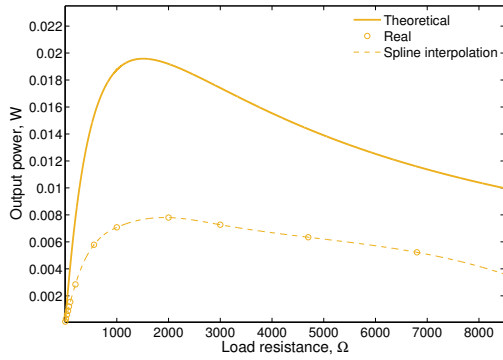
(b) $f = 1 \text{ MHz}$



(c) $f = 2 \text{ MHz}$

Figure E.6: Output power w.r.t. load resistance for SS topology

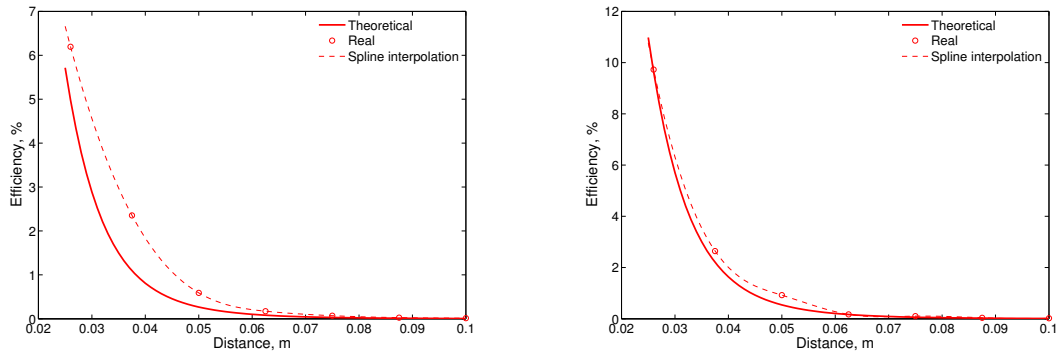
(a) $f = 0.7 \text{ MHz}$ (b) $f = 1 \text{ MHz}$ (c) $f = 2 \text{ MHz}$ **Figure E.7: Efficiency w.r.t. load resistance for SP topology**(a) $f = 0.7 \text{ MHz}$ (b) $f = 1 \text{ MHz}$



(c) $f = 2$ MHz

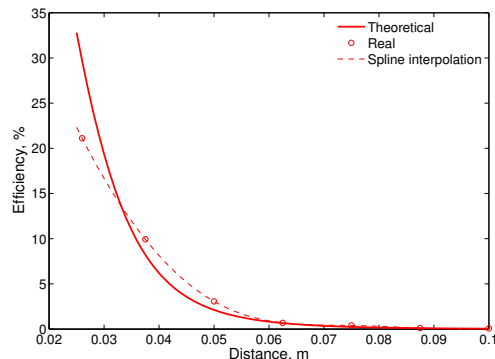
Figure E.8: Output power w.r.t. load resistance for SP topology

E.2 Model B



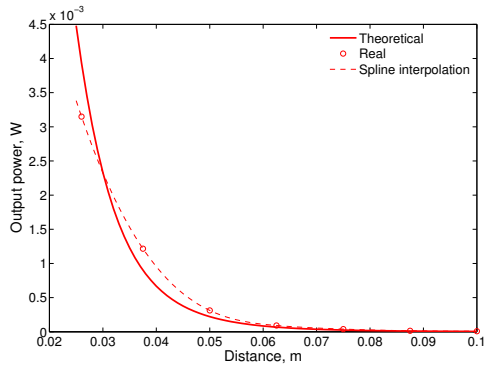
(a) $f = 0.7$ MHz

(b) $f = 1$ MHz

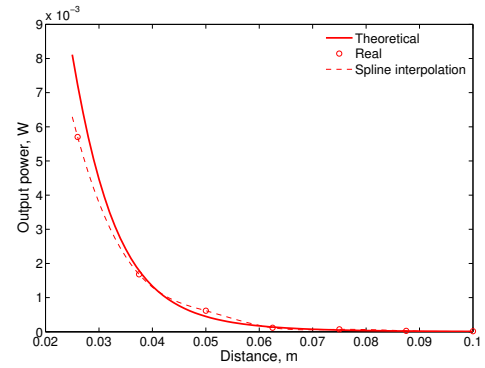


(c) $f = 2$ MHz

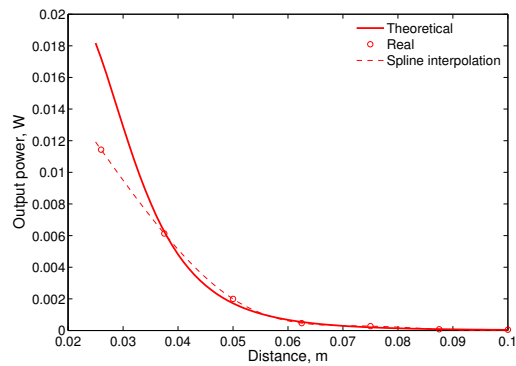
Figure E.9: Efficiency w.r.t. distance for SS topology



(a) $f = 0.7 \text{ MHz}$

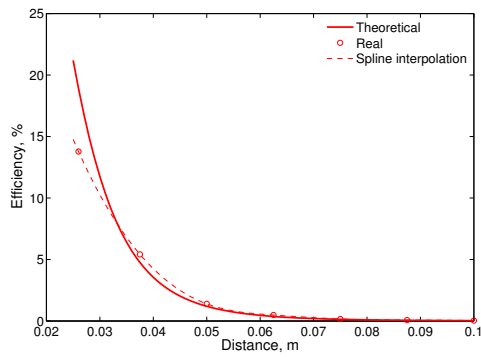


(b) $f = 1 \text{ MHz}$

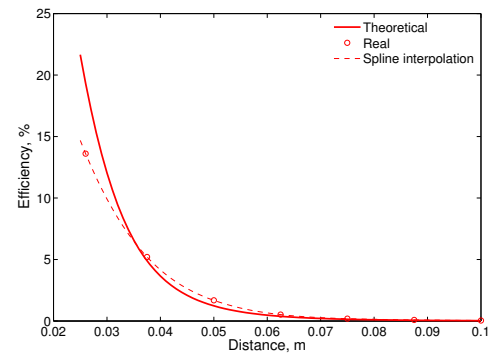


(c) $f = 2 \text{ MHz}$

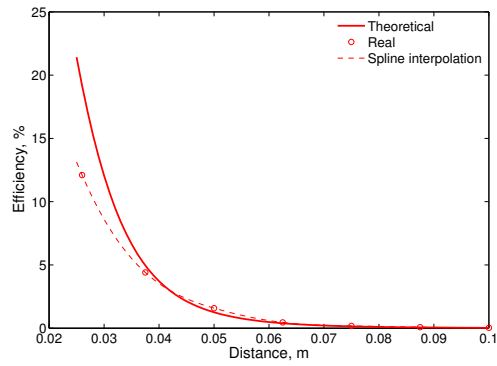
Figure E.10: Output power w.r.t. distance for SS topology



(a) $f = 0.7 \text{ MHz}$

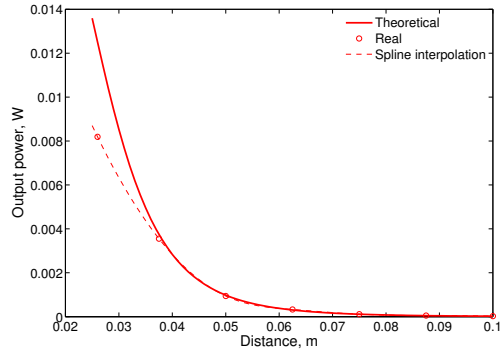


(b) $f = 1 \text{ MHz}$

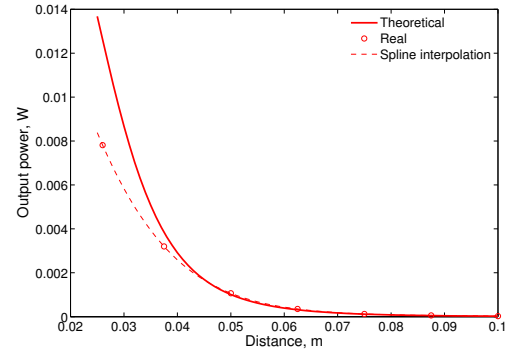


(c) $f = 2 \text{ MHz}$

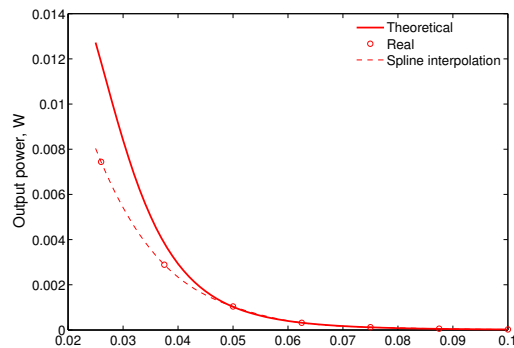
Figure E.11: Efficiency w.r.t. distance for SP topology



(a) $f = 0.7 \text{ MHz}$

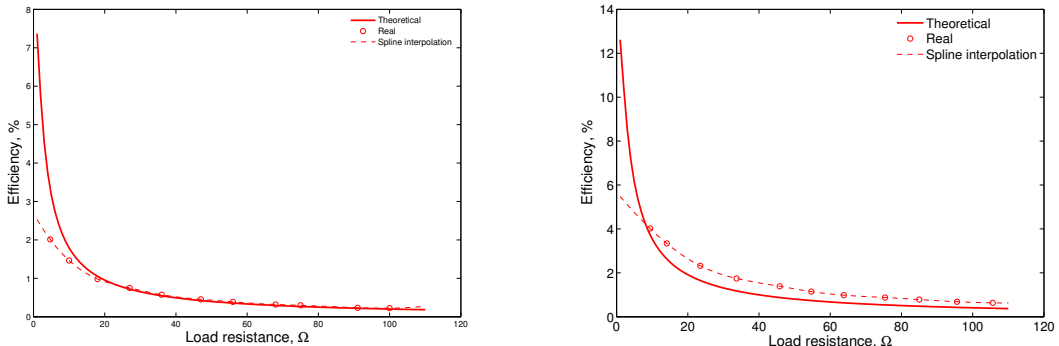


(b) $f = 1 \text{ MHz}$



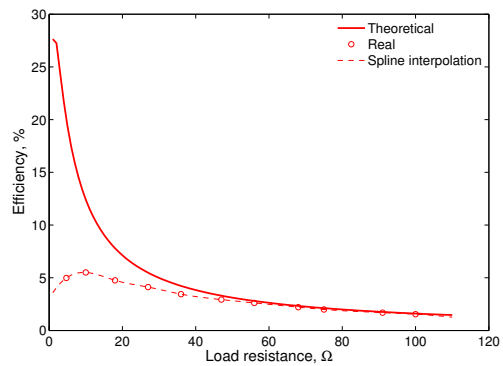
(c) $f = 2 \text{ MHz}$

Figure E.12: Output power w.r.t. distance for SP topology



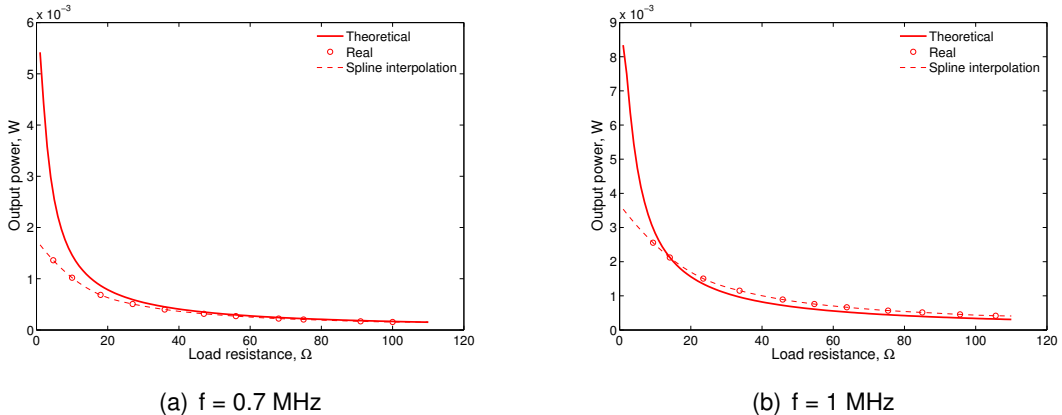
(a) $f = 0.7 \text{ MHz}$

(b) $f = 1 \text{ MHz}$



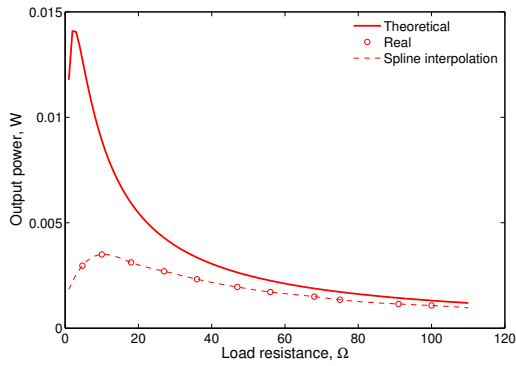
(c) $f = 2 \text{ MHz}$

Figure E.13: Efficiency w.r.t. load resistance for SS topology



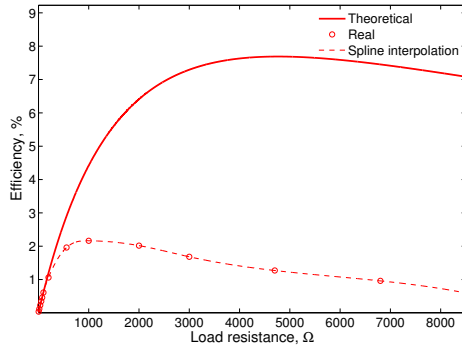
(a) $f = 0.7 \text{ MHz}$

(b) $f = 1 \text{ MHz}$

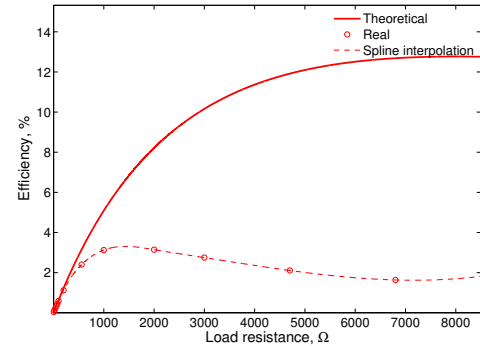


(c) $f = 2 \text{ MHz}$

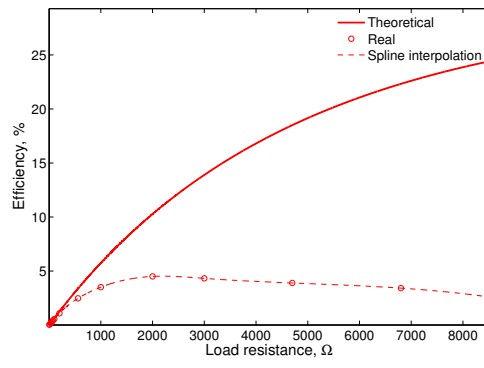
Figure E.14: Output power w.r.t. load resistance for SS topology



(a) $f = 0.7 \text{ MHz}$



(b) $f = 1 \text{ MHz}$



(c) $f = 2 \text{ MHz}$

Figure E.15: Efficiency w.r.t. load resistance for SP topology

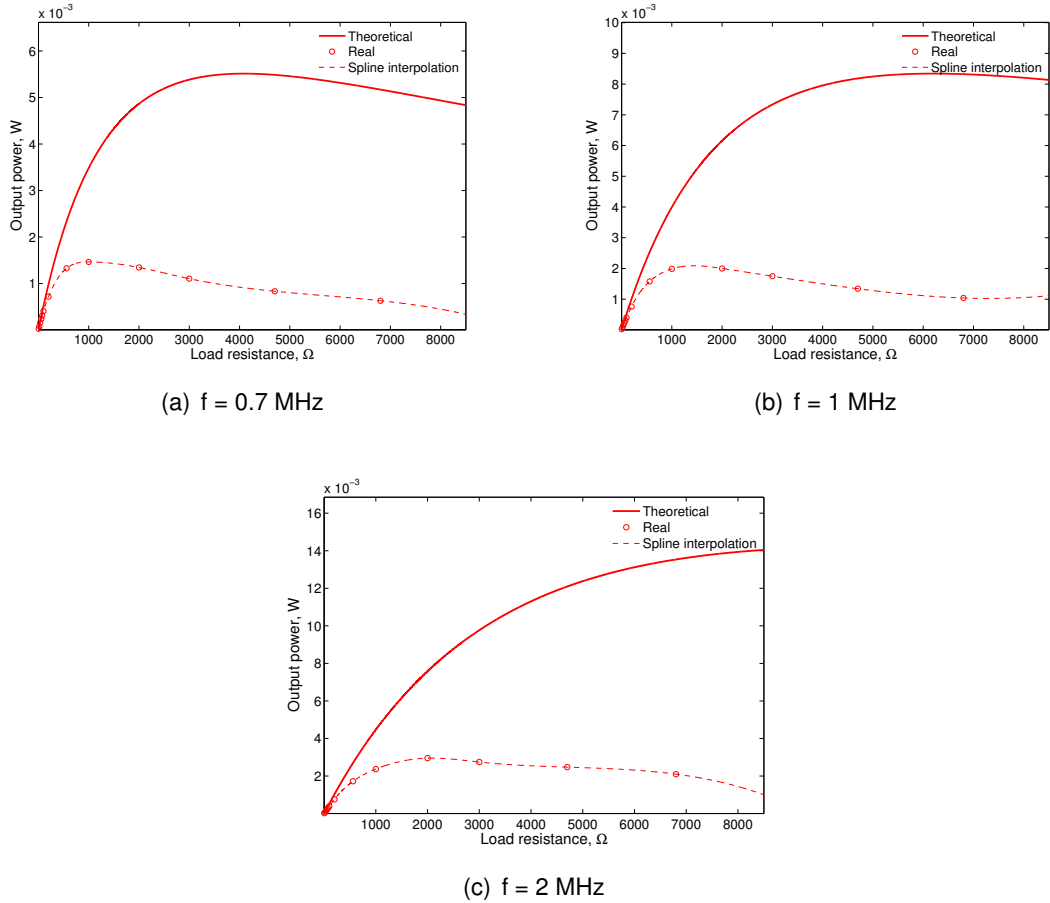
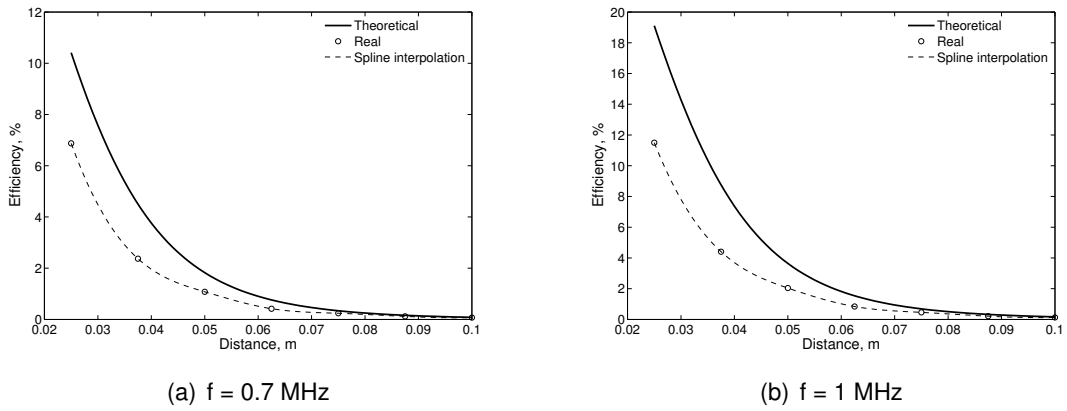
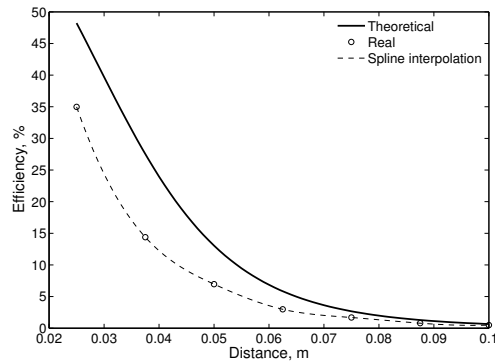


Figure E.16: Output power w.r.t. load resistance for SP topology

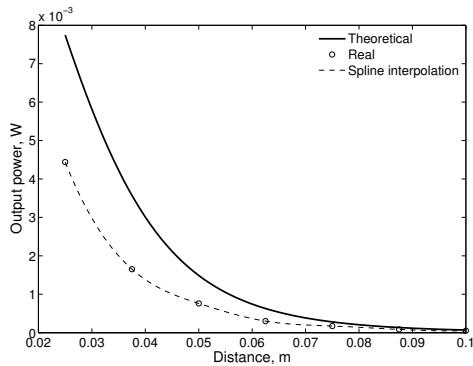
E.3 Model C



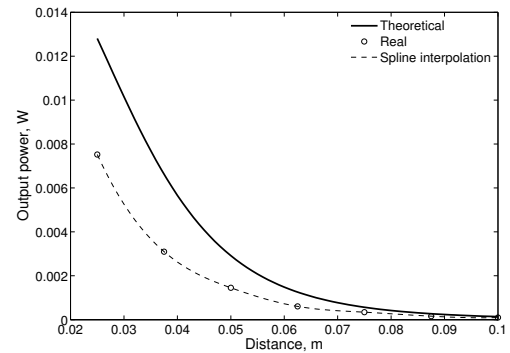


(c) $f = 2 \text{ MHz}$

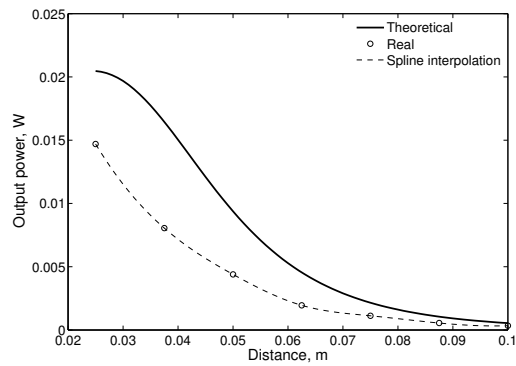
Figure E.17: Efficiency w.r.t. distance for SS topology



(a) $f = 0.7 \text{ MHz}$



(b) $f = 1 \text{ MHz}$



(c) $f = 2 \text{ MHz}$

Figure E.18: Output power w.r.t. distance for SS topology

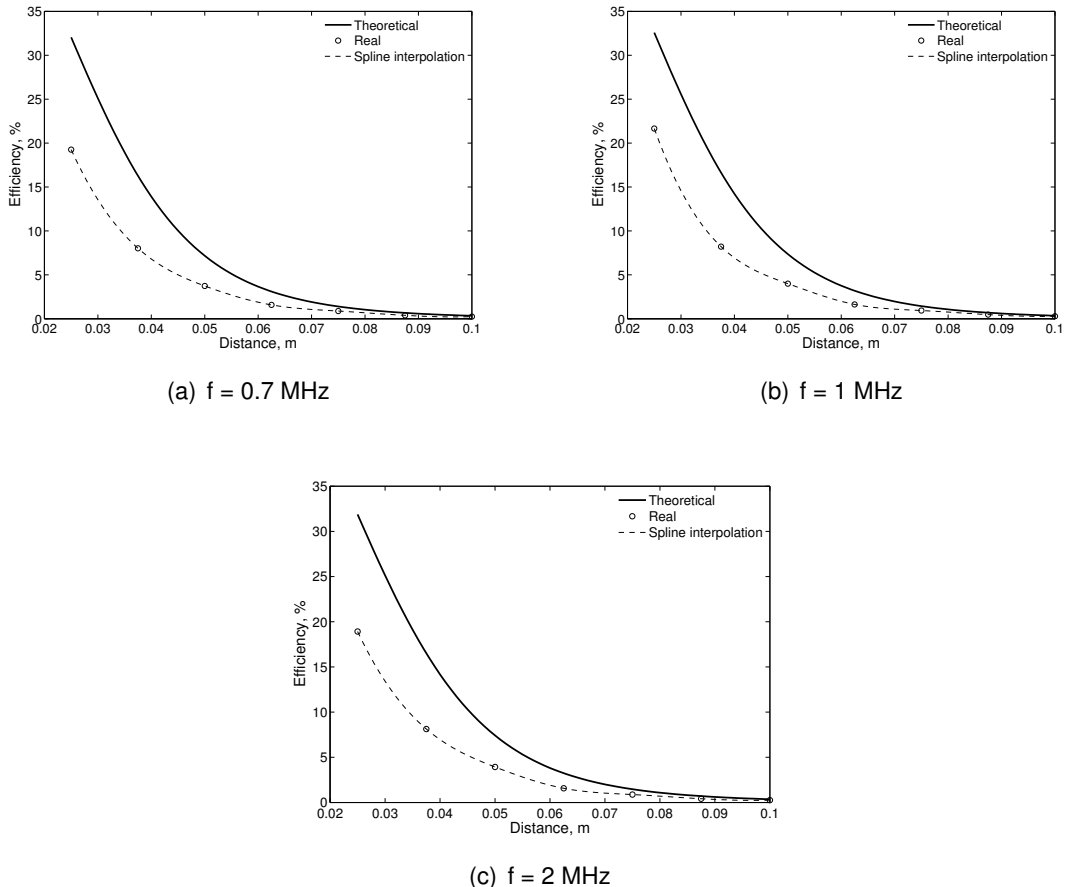
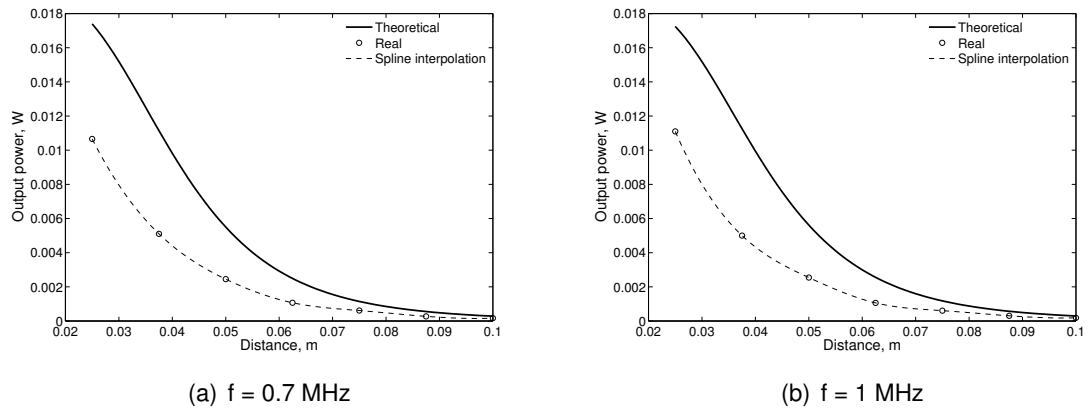
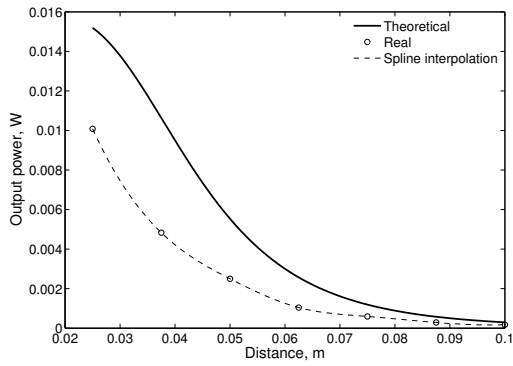


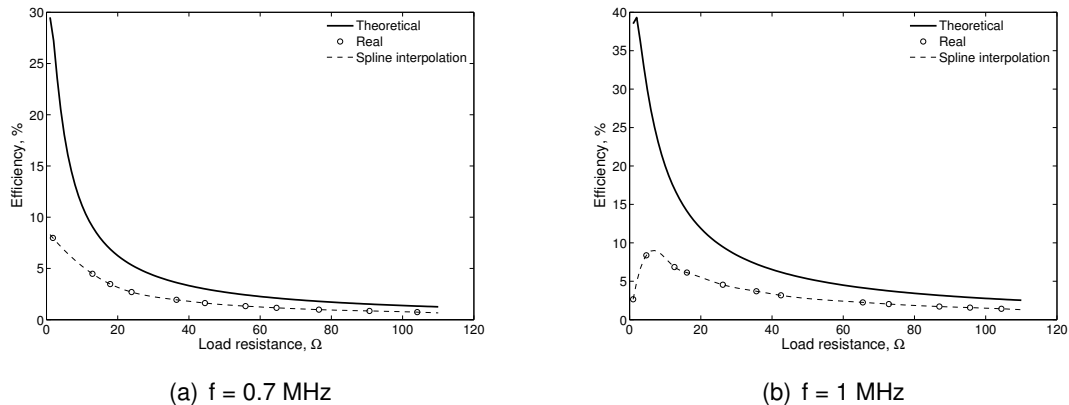
Figure E.19: Efficiency w.r.t. distance for SP topology





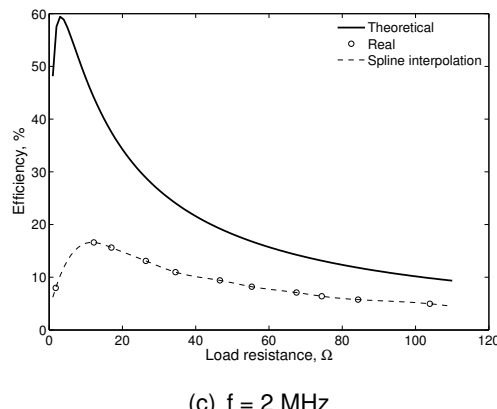
(c) $f = 2 \text{ MHz}$

Figure E.20: Output power w.r.t. distance for SP topology



(a) $f = 0.7 \text{ MHz}$

(b) $f = 1 \text{ MHz}$



(c) $f = 2 \text{ MHz}$

Figure E.21: Efficiency w.r.t. load resistance for SS topology

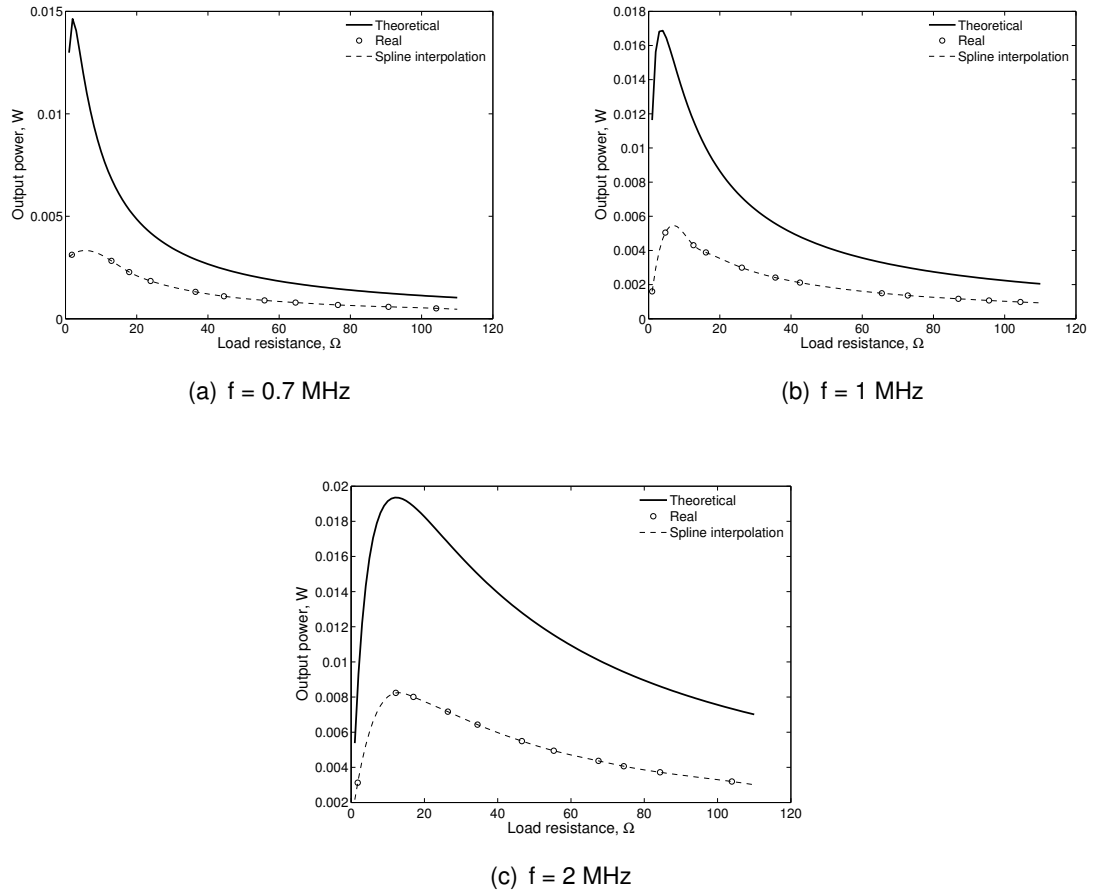
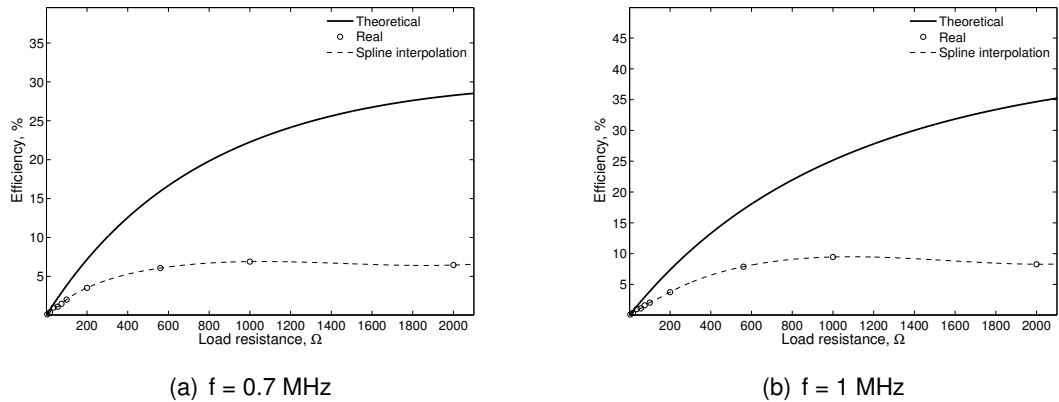
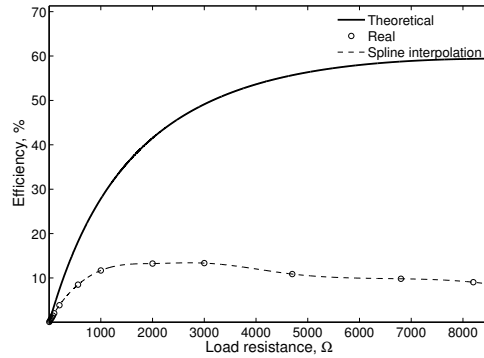


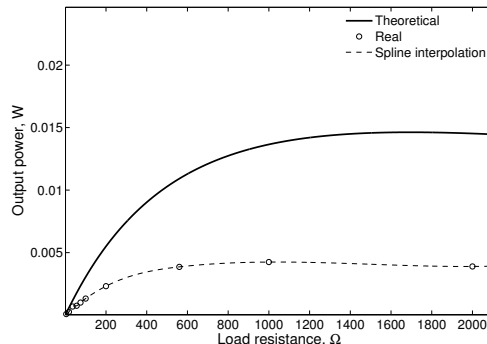
Figure E.22: Output power w.r.t. load resistance for SS topology



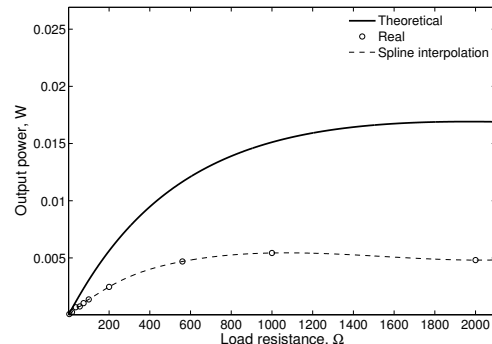


(c) $f = 2 \text{ MHz}$

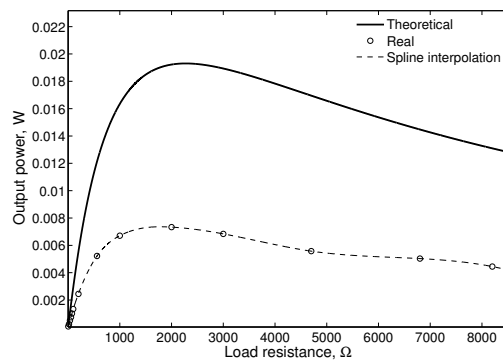
Figure E.23: Efficiency w.r.t. load resistance for SP topology



(a) $f = 0.7 \text{ MHz}$



(b) $f = 1 \text{ MHz}$

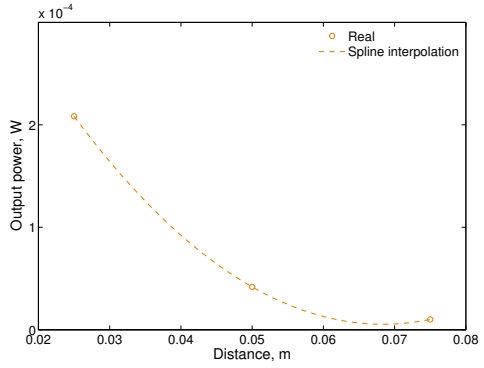


(c) $f = 2 \text{ MHz}$

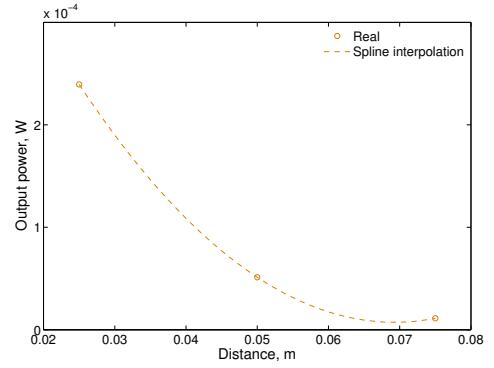
Figure E.24: Output power w.r.t. load resistance for SP topology

E.4 Output power for models D1 and D2

This plots demonstrate that a bigger receiver coil diameter is preferred upon a bigger transmitter coil diameter. This is stated at Section 2.6.5.5



(a) D1 (Tx) / D2 (Rx)



(b) D2 (Tx) / D1 (Rx)

Figure E.25: Experimental demonstration of the output power depending on the coil receiver radius

APPENDIX F. PROGRAMMING CODE

Along this project, the plots and the mathematical model have been performed using *MATLAB*. Some important codes are shown below.

```
1
2 close all
3 clear all
4 clc
5
6 global rhoC
7
8 select = input('--> Press 1... L-R vs. f\n--> Press 2... Q vs. ...
    f\n--> Press 3... Q COILS\n--> Press 4... Resistance ...
    Comparison\n');
9 if select!=3
10 prompt = 'MODEL SELECTION      Enter key\nnModel Atx ...
    a1\nnModel Arx          a2\nnModel Btx          b1\nnModel ...
    Brx                  b2\nnModel Ctx          c1\nnModel Crx ...
    c2\nnModel D1          d1\nnModel D2          ...
    d2\n';
11 key = input(prompt,'s');
12
13 if strcmp(key,'a1') == 1; modelo = 'modeloATX'; N = 8; Radius = ...
    0.05; end
14 if strcmp(key,'a2') == 1; modelo = 'modeloARX'; N = 8; Radius = ...
    0.05; end
15 if strcmp(key,'b1') == 1; modelo = 'modelo0TX'; N = 19; Radius = ...
    0.02; end
16 if strcmp(key,'b2') == 1; modelo = 'modelo0RX'; N = 19; Radius = ...
    0.02; end
17 if strcmp(key,'c1') == 1; modelo = 'modelo00TX'; N = 10;Radius = ...
    0.04; end
18 if strcmp(key,'c2') == 1; modelo = 'modelo00RX'; N = 10;Radius = ...
    0.04; end
19 if strcmp(key,'d1') == 1; modelo = 'modeloCobreGrande'; N = ...
    7;Radius =0.04; end
20 if strcmp(key,'d2') == 1; modelo = 'modeloCobrePequena'; N = 11; ...
    Radius = 0.015; end
21 end
22
23 %% Inductance and Resistance w.r.t Frequency
24 if select == 1
25     for i=1:1
26         Coil = LRF(modelo);
27         f = Coil(:,1);
28         L = Coil(:,2)*1e6;
29         R = Coil(:,3);
30         Q = Coil(:,4);
31         [ax,p1,p2] = plotyy(f,L,f,R,'semilogx','semilogx');
32
33         % Plots
34         xlabel(ax(1),'Frequency, Hz','FontSize',20)
35         ylabel(ax(1),'\mu H','FontSize',20)
36         ylabel(ax(2),'Resistance, \Omega','FontSize',20)
```

```

37         set(gcf,'color','white')
38         set(ax(1),'fontsize',18)
39         set(ax(2),'fontsize',18)
40         set(p1,'LineWidth',2)
41         set(p2,'LineWidth',2)
42
43 %             set(ax(2),'YTick',[0.05 0.1 0.15]);
44     end
45 end
46
47 %% Q-Factor w.r.t Frequency
48 if select == 2
49     for i=1:1
50         Coil = LRF(modelo);
51         f = Coil(:,1);
52         L = Coil(:,2)*1e6;
53         R = Coil(:,3);
54         Q = 1e-6*2*pi*f.*L./R;
55
56         % Plots
57         plot(f,Q,'LineWidth',2)
58         xlabel('Frequency, Hz','FontSize',17)
59         ylabel('Q factor','FontSize',17)
60         set(gcf,'color','white')
61         set(gca,'fontsize',15)
62         grid on
63     end
64 end
65
66 %% All Q-Factors
67 if select == 3
68 C = {[1 .8 0],[1 .8 0],'r','r','k','k',[1 .6 .2],[1 .6 .2]};
69 figure
70 for i=1:8
71     % Type: 1-->Tx / 0-->Rx
72     if i == 1; modelo = 'modeloATX'; type = 1; end
73     if i == 2; modelo = 'modeloARX'; type = 0; end
74     if i == 3; modelo = 'modelo0TX'; type = 1; end
75     if i == 4; modelo = 'modelo0RX'; type = 0; end
76     if i == 5; modelo = 'modelo00TX'; type = 1; end
77     if i == 6; modelo = 'modelo00RX'; type = 0; end
78     if i == 7; modelo = 'modeloCobreGrande'; type = 2; end
79     if i == 8; modelo = 'modeloCobrePequena'; type = 2; end
80     Coil = LRF(modelo);
81     f = Coil(:,1);
82     L = Coil(:,2)*1e6;
83     R = Coil(:,3);
84     Q = 1e-6*2*pi*f.*L./R;
85     f = f/1e6;
86     if type == 1
87         plot(f,Q,'LineWidth',2,'color',C{i})
88     elseif type == 0
89         plot(f,Q,'LineWidth',1,'color',C{i})
90     end
91     hold on
92 end
93 xlabel('Frequency, MHz','FontSize',17)
94 ylabel('Q factor','FontSize',17)

```

```

95 set(gcf,'color','white')
96 set(gca,'fontsize',15)
97 grid on
98 axis([0 2.2 0 200])
99 legend('Model A_{Tx}', 'Model A_{Rx}', 'Model B_{Tx}', 'Model ...'
    'B_{Rx}', 'Model C_{Tx}', 'Model C_{Rx}', 'Model D1', 'Model ...'
    'D2', 'Location', 'southeast')
100 end
101
102 if select == 4
103     Coil = LRF(modelo);
104     f = Coil(:,1);
105     L = Coil(:,2)*1e6;
106     R = Coil(:,3);
107     Q = Coil(:,4);
108     % Select wire diameter
109     if strcmp(key,'d1') == 1 || strcmp(key,'d2') == 1
110         D = 1e-3;
111     else
112         D = 0.597e-3;
113     end
114
115     rhoC = 1.68e-8;
116     frequency = 1e4:1e3:1e7;
117     lth1=2*pi*Radius*N;
118     S = pi*(D^2)/4;
119
120     for j=1:length(frequency)
121         Rac(j) = AC_Resistance(lth1,S,D,frequency(j),N);
122     end
123
124     % Plots
125     semilogx(f,R,frequency,Rac,'LineWidth',2);
126     xlabel('Frequency, Hz','FontSize',17)
127     ylabel('Resistance, \Omega','FontSize',17)
128     set(gcf,'color','white')
129     set(gca,'fontsize',15)
130     legend('Experimental', 'Theoretical', 'Location', 'northwest')
131     legend boxoff
132     axis([0 1e7 0 4])
133 end

```

```

1 clear all
2 close all
3 clc
4
5 % /////////////////////////////////
6 % ///////////////////////////////////////////////////
7 % // Power Analysis /////
8 % ///////////////////////////////////////////////////
9 % /////////////////////////////////
10
11 % The power received by the RX mainly depends upon the separation
12 % between the coils or the mutual coupling. Two coils are said ...
13 % to be linked
14 % inductively, when the primary coil excited by the external ...

```

```

    source is able
14 % to have a magnetic field induced in the secondary coil, ...
    producing a
15 % voltage across its terminals as a result.
16
17 % Define Global Variables
18 global u0 rhoC
19
20 u0 = 4*pi*1e-7;      % Permeability of air [H/m]
21 rhoC = 1.71e-8;       % Copper Resistivity [Ohm*m]
22
23 %% Coil Parameters and Theoretical Inductance Values
24 R1 = 0.5;
25 R2 = 0.5;
26 L1 = 10e-6;
27 L2 = 10e-6;
28 C1 = 2e-9;
29 C2 = 2e-9;
30 M = 3e-6;
31
32 fres = 1/(2*pi*sqrt(L1*C1));
33 %% Define system parameters
34 Vs = 5;
35 Vamp = Vs*sqrt(2);
36 Zs = 50;
37 ZL = 100;
38 %% Operating frequency
39 f = 1:1000:0.5e8;
40 % f = fres;
41 % f = 1.05e6:1e3:1.2e7;
42 % f = 1.064e6;
43 %% Secondary Capacitor in Series
44
45 % Primary Capacitor in SERIES / Secondary Capacitor in SERIES
46 [eff,Pout,Pin,I1,I2] = ...
    SStopologyModel(L1,L2,f,Zs,ZL,Vamp,R1,R2,C1,C2,M);
47
48 % Primary Capacitor in SERIES / Secondary Capacitor in PARALLEL
49 [eff2,Pout2,Pin2,I12,I22] = ...
    SPtopologyModel(L1,L2,f,Zs,ZL,Vamp,R1,R2,C1,C2,M);
50
51 % Primary Capacitor in PARALLEL / Secondary Capacitor in SERIES
52 [eff3,Pout3,Pin3,I13,I23] = ...
    PStopologyModel(L1,L2,f,Zs,ZL,Vamp,R1,R2,C1,C2,M);
53
54 % Primary Capacitor in PARALLEL / Secondary Capacitor in PARALLEL
55 [eff4,Pout4,Pin4,I14,I24] = ...
    PPtopologyModel(L1,L2,f,Zs,ZL,Vamp,R1,R2,C1,C2,M);
56
57 close all
58
59 figure;
60 semilogx(f/fres,eff,'r','linewidth',1.5);
61 hold on
62 semilogx(f/fres,eff2,'y','linewidth',1.5);
63 semilogx(f/fres,eff3,'Color',[0.2 0.8 0.4],'linewidth',1.5);
64 semilogx(f/fres,eff4,'Color',[0.0 0.2 1.0],'linewidth',1.5);
65
```

```

66 xlabel('Normalized frequency (f/f_0)', 'FontSize', 17)
67 ylabel('Efficiency, %', 'FontSize', 17)
68 set(gcf, 'color', 'white')
69 axis([10^(-2) 4e1 0 30])
70 legend('SS', 'SP', 'PS', 'PP');
71 legend('PS', 'PP');
72 legend('SS', 'SP');
73 legend boxoff
74
75 % close all
76
77 figure;
78 semilogx(f/fres, Pout, 'r', 'LineWidth', 1.5);
79 hold on
80 semilogx(f/fres, Pout2, 'y', 'LineWidth', 1.5);
81 semilogx(f/fres, Pout3, 'Color', [0.2 0.8 0.4], 'LineWidth', 1.5);
82 semilogx(f/fres, Pout4, 'Color', [0.0 0.2 1.0], 'LineWidth', 1.5);
83
84 xlabel('Normalized frequency (f/f_0)', 'FontSize', 17)
85 ylabel('Output Power, W', 'FontSize', 17)
86 set(gcf, 'color', 'white')
87 axis([10^(-1) 10^1 0 0.12])
88 legend('SS', 'SP', 'PS', 'PP');
89 legend boxoff

```

```

1 function [eff, Pout, Pin, I1, I2] = ...
   SStopologyModel(L1, L2, f, Zs, ZL, Vamp, R1, R2, C1, C2, M)
2
3 w = 2*pi*f; % Angular frequency [rad/s]
4
5 fres = 1/(2*pi*sqrt(C1*L1));
6
7 Z1 = Zs+R1+1i*w*L1-1i./(w*C1);
8 modZ1 = abs(Z1);
9
10 Z2 = R2+ZL+1i*w*L2-1i./(w*C2);
11 modZ2 = abs(Z2);
12
13 ZR = w.^2.*M.^2./Z2;
14 modZR = abs(ZR);
15
16 Zeq = Z1+ZR;
17 modZeq = abs(Zeq);
18 argZeq = angle(Zeq);
19
20 I1 = Vamp./modZeq;
21 I1eff = I1/sqrt(2);
22
23 I2 = w.*M.*I1./modZ2;
24 I2eff = I2/sqrt(2);
25
26 powerfactor = cos(argZeq);
27 Pin = Vamp/sqrt(2).*I1eff.*cos(argZeq);
28 Pout = I2eff.^2*ZL;
29 eff = (Pout./Pin)*100;
30

```

```

31 figure;
32 semilogx(f/fres,modZeq,'r','linewidth',2);
33 hold on
34 semilogx(f/fres,imag(Zeq),'Color',[0.2 0.8 0.4],'linewidth',2);
35 semilogx(f/fres,real(Zeq),'k','linewidth',2);
36 xlabel('Normalized frequency (f/f_0)', 'FontSize',17)
37 ylabel('Impedance, \Omega', 'FontSize',17)
38 set(gcf,'color','white')
39 legend('Z_{eq}', 'X_{eq}', 'R_{eq}', 'Location', 'Northwest')
40 legend boxoff
41 axis([10^(-1) 5e1 -1000 1500])
42 plot([min(f)/fres, max(f)/fres],[0,0], 'k--')
43
44 end

```

```

1 function [eff,Pout,Pin,I1,I2] = ...
    SPtopologyModel(L1,L2,f,Zs,ZL,Vamp,R1,R2,C1,C2,M)
2
3 w = 2*pi*f; % Angular frequency [rad/s]
4
5 % C2 = L2/ZL*1/(R2+ZL);
6
7 fres = 1/(2*pi*sqrt(C1*L1));
8
9 Z1 = Zs+R1+1i*w*L1-1i./(w*C1);
10 modZ1 = abs(Z1);
11
12 Z2 = R2+1i*w*L2+1./(1./ZL+1i*w*C2);
13 modZ2 = abs(Z2);
14
15 ZR = w.^2.*M.^2./Z2;
16 modZR = abs(ZR);
17
18 Zeq = Z1+ZR;
19 modZeq = abs(Zeq);
20 argZeq = angle(Zeq);
21
22 I1 = Vamp./modZeq;
23 I1eff = I1/sqrt(2);
24
25 I2 = w.*M.*I1./modZ2;
26 I2eff = I2/sqrt(2);
27
28 V2 = abs(ZL./(1+1i*w*C1*ZL)).*I2eff;
29 Iload = V2/ZL;
30
31 powerfactor = cos(argZeq);
32 Pin = Vamp/sqrt(2).*I1eff.*cos(argZeq);
33 Pout = Iload.^2*ZL;
34 eff = (Pout./Pin)*100;
35
36 figure;
37 semilogx(f/fres,modZeq,'r','linewidth',2);
38 hold on
39 semilogx(f/fres,imag(Zeq),'Color',[0.2 0.8 0.4],'linewidth',2);
40 semilogx(f/fres,real(Zeq),'k','linewidth',2);

```

```

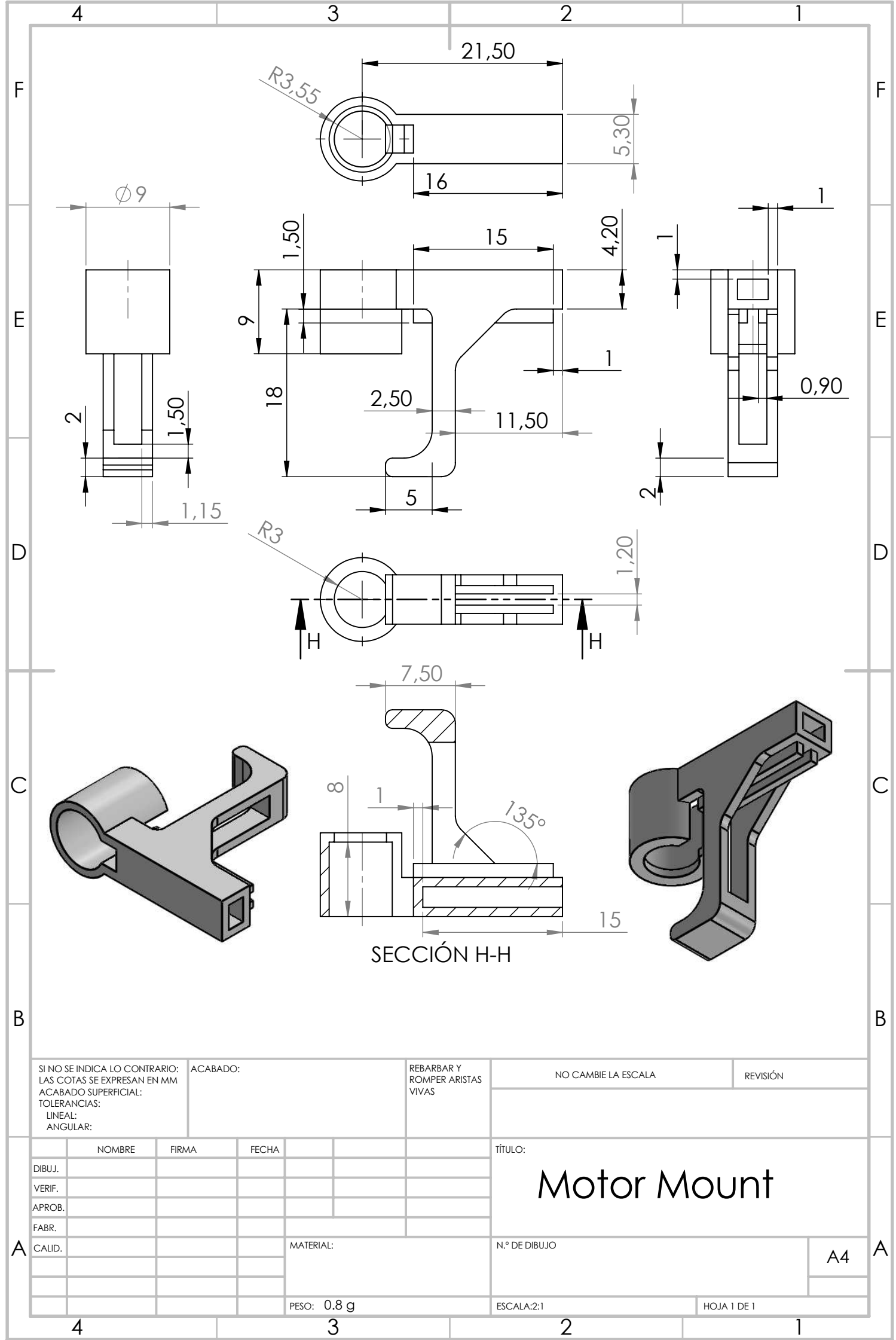
41 xlabel('Normalized frequency (f/f_0)', 'FontSize', 17)
42 ylabel('Impedance, \Omega', 'FontSize', 17)
43 set(gcf, 'color', 'white')
44 legend('Z_{eq}', 'X_{eq}', 'R_{eq}', 'Location', 'Northwest')
45 legend boxoff
46 axis([10^(-1) 5e1 -1000 1500])
47 plot([min(f)/fres, max(f)/fres], [0,0], 'k--')
48
49 end

```

```

1 function [Rac,R_skin,R_proximity,R_dc] = ...
AC_Resistance(lth1,S,d,f,N1)
2
3 global rhoC
4
5
6 R_dc = rhoC*lth1/S; % DC Resistance
7
8 R_skin = R_dc*(d*20.8*pi/rhoC.*...
9 f.^1/2)*1e-9;
10
11 sigma = 6.74./sqrt(f); % Skin depth
12
13 eps = d./(2*sigma)*sqrt((pi*N1*d)/(N1*d));
14
15 R_proximity = R_dc*eps*((sinh(2*...
16 eps)+sin(2*eps))/(cosh(2*eps)-...
17 cos(2*eps)));
18
19 Rac = R_dc+R_skin+R_proximity; % AC Resistance
20
21 end

```



bq25504 EVM – Ultra Low Power Boost Converter with Battery Management for Energy Harvester Applications

This user's guide describes the bq25504 evaluation module (EVM), how to perform a stand-alone evaluation and allows the EVM to interface with the system and host. This EVM is programmed from the factory for settings compatible with most MCU's and 3V coin cell batteries. The EVM is programmed to deliver a 3.1VDC maximum voltage (OV) for charging the storage element and the under voltage is programmed to 2.2VDC. The VBAT_OK indicator toggles high when VSTOR ramps up to 2.8VDC and toggles low when VSTOR ramps down to 2.4VDC.

Contents

1	Introduction	2
1.1	EVM Features	2
1.2	General Description	2
1.3	Design and Evaluation Considerations	3
2	Performance Specification Summary	4
3	Test Summary	4
3.1	Equipment	4
3.2	Equipment and EVM Setup	4
3.3	Test procedures	5
4	PCB Layout Guideline	11
5	Bill of Materials, Board Layout and Schematics	12
5.1	Bill of Materials	12
5.2	EVM Board Layout	13
5.3	EVM Schematic	15

List of Figures

1	Test Setup for HPA674A (bq25504 EVM)	5
2	Startup with no Battery and 10k Load.....	6
3	Startup with Battery Less Than UV.....	7
4	Powering up with a Battery above UV	7
5	BAT_OK High/Low 2.8V/2.34V – Ramping Battery from 0V to 3.1V (OV) and Down to 1.8V.....	8
6	Basic Switching Converter, Vin = 1V, Vbat = 2.5V	9
7	EVM Operation Near OV With 100- Ω Battery Impedance	10
8	EVM PCB Top Assembly.....	13
9	EVM PCB Top Layer	13
10	EVM PCB Bottom Layer.....	14
11	EVM Schematic.....	15

List of Tables

1	I/O Connections and Configuration for Evaluation of bq25504 EVM.....	4
2	Bill of Materials.....	12

1 Introduction

1.1 EVM Features

- Evaluation module for bq25504
- Ultra low power boost converter/charger with battery management for energy harvester applications
- Resistor-programmable settings for under voltage, over voltage providing flexible battery management; POTs Included for fine tuning the settings (not populated)
- Programmable push-pull output Indicator for battery status (VBAT_OK)
- Test points for key signals available for testing purpose – easy probe hook-up.
- Jumpers available – easy to change settings

1.2 General Description

The bq25504 is the first of a new family of intelligent integrated energy harvesting Nano-Power management solutions that are well suited for meeting the special needs of ultra low power applications. The product is specifically designed to efficiently acquire and manage the microwatts (μW) to miliwatts (mW) of power generated from a variety of DC sources like photovoltaic (solar) or thermal electric generators. The bq25504 is the first device of its kind to implement a highly efficient boost converter/charger targeted toward products and systems, such as wireless sensor networks (WSN) which have stringent power and operational demands. The design of the bq25504 starts with a DC-DC boost converter/charger that requires only microwatts of power to begin operating. Once started, the boost converter/charger can effectively extract power from low voltage output harvesters such as thermoelectric generators (TEGs) or single / dual cell solar panels. The boost converter can be started with VIN as low as 330 mV typ., and once started, can continue to harvest energy down to $\text{V}_{\text{IN}} \approx 100$ mV.

The bq25504 also implements a programmable maximum power point tracking (MPPT) sampling network to optimize the transfer of power into the device. The MPP is listed by the harvesting manufacturer as a percentage of its open circuit (OC) voltage. Typically solar cells are at their MPP when loaded to ~80% of their OC voltage. The bq25504 periodically samples the open circuit input voltage by disabling the boost converter (approximately every 16 seconds) and stores the programmed MPP ratio of the OC voltage on the external reference capacitor, C5. If the storage element is less than the maximum voltage (OV) then the boost converter will load the harvesting source until it reaches the MPP (C5 voltage reference) and then regulate the input voltage of the converter, thus transferring the maximum amount of power to the output. Alternatively, an external reference voltage can be provided, by a MCU to the REFS pin, to adjust C5 independently. The shunt on JP1 has to be moved from the Divider setting to STOR when providing this external reference (JP1-2 tied to JP1-1 – OSC/STOR).

The bq25504 was designed with the flexibility to support a variety of energy storage elements. The availability of the sources from which harvesters extract their energy can often be sporadic or time-varying. Systems will typically need some type of energy storage element, such as a re-chargeable battery, super capacitor, or conventional capacitor. The storage element will make certain constant power is available when needed for the systems. The storage element also allows the system to handle any peak currents that can not directly come from the input source.

To prevent damage to a customer's storage element, both maximum and minimum voltages are monitored against the user programmed under-voltage (UV) and over-voltage (OV) levels.

To further assist users in the strict management of their energy budgets, the bq25504 toggles the battery good flag to signal the microprocessor when the voltage on an energy storage element or capacitor has dropped below a pre-set critical level. This should trigger the shedding of load currents to prevent the system from entering an under voltage condition.

The OV, UV and battery good thresholds are programmed independently. The EVM has three 500K Ω potentiometers (not installed at factory) to allow fine tuning of the three programmable thresholds. This only need be done if the user needs precision, the POTs provide about $\pm 50\text{mV}$ shift.

For details, see bq25504 data sheet ([SLUSAH0](#)).

1.3 Design and Evaluation Considerations

This user's guide is not a replacement for the data sheet. Reading the data sheet first will help in understanding the operations and features of this IC. Be sure to make note of the capacitor selection section when designing the EVM. Many of the IC's pin names start with a "V" and this "V" is removed on the EVM connector's label. The names are interchangeable.

This IC is a highly efficient charger for a storage element such as a battery or super capacitor. In this document, "battery" will be used but one could substitute any appropriate storage element. The main difference between a battery and a super capacitor is the capacity curve. The battery typically has little or no capacity below a certain voltage, whereas the capacitor does have capacity at lower voltages.

In the lab when using a lab power supply rather than an energy harvester, one will have the output of the lab supply, V_{source} , followed by the harvester's impedance (about 20Ω) and connected to V_{IN} of the EVM. These two signals are separated by the 20Ω source impedance which represents the internal impedance of the source. V_{IN} is equal to V_{source} when there is no load (open circuit) and is pulled down to the MPPT harvester threshold when the charger is able to deliver the maximum power before reaching OV.

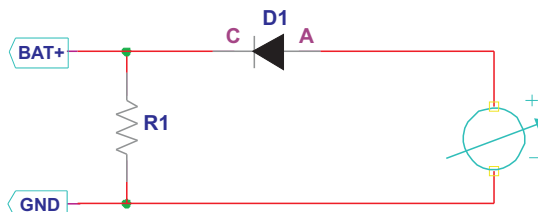
The over voltage (OV) setting initially is lower than the programmed value at startup (varies on conditions) and is updated after the first ~32ms. Subsequent updates are every ~64ms. The OV threshold is the reference for maximum voltage on VSTOR and the boost converter will stop switching if the voltage on VSTOR reaches the OV reference. The UV is checked every ~64ms to determine if the BAT FET should be on or off. The open circuit (OC) input voltage is measured every ~16 seconds which is used to calculate the Maximum Power Point Tracking (MPPT) threshold (programmed with resistors to 78% at the factory). This periodic update continually optimizes maximum power delivery based on the harvesting conditions.

Harvesting ultra low power energy requires a different mind set when designing a system. Often there is not enough real time input harvested power to run the system in full operation so energy is collected over a period of time, stored in a battery and then used periodically to power the system.

The designer needs to define a "Battery OK" threshold and battery discharged threshold (Not OK) to allow successful system operation. The BAT_OK high/low threshold are programmed at the factory to 2.8V and 2.4V using resistors R7, R8, and R9. A BAT_OK high signal would typically indicate to the host that the battery is above 2.8V and ready to use and if low would indicate that the cell is discharged such that the system load should be reduced or disabled. The BAT_OK signal is checked every 64ms.

The quiescent current, which is basically the current from the battery to the IC, can be measured at the STOR pin. To measure the current the user should connect a $100k\Omega$ resistor to J5-2 (STOR) and connect a 3V supply from the other end of this resistor to the ground of the EVM. A $10M\Omega$ meter can be used to measure the voltage drop across the resistor and calculate the current. No other connections should be made to the EVM and the measurement should be taken after steady state conditions are reached (may take a few minutes). The reading should be in the range of 375nA.

The battery (storage element) can be replaced with a simulated battery. Often electronic 4 quadrant loads give erratic results with a "battery charger" due to the charger changing states (fast-charge to termination and refresh) while the electronic load is changing loads to maintain the "battery" voltage. The charging and loading get out of phase and creates a large signal oscillation which is due to the 4 quadrant meter. A simple circuit can be used to simulate a battery and works well and can quickly be adjusted for voltage. It consists of load resistor ($\sim 10\Omega$, 2W) to pull the output down to some minimum storage voltage (sinking current part of battery) and a lab supply connected to the BAT pin via a diode. The lab supply biases up the battery voltage to the desired level. It may be necessary to add more capacitance across R1.



2 Performance Specification Summary

See Data Sheet “Recommended Operating Conditions” for component adjustments. For details about the resistor programmable settings, see bq25504 data sheet ([SLUSAH0](#)).

		MIN	NOM	MAX	UNIT
V _{IN} (DC)	DC input voltage into VIN_DC	0.13		3.0	V
V _{IN_Start-up} (DC)	DC minimum Start-up Voltage		330		mV
V _{OV}	Over Voltage – Sets maximum output voltage	2.9	3.1	3.3	V
V _{UV}	Under voltage setting for shorting VSTOR to VBAT	2.1	2.2	2.3	V
V _{BAT_OK}	VBAT_OK indication toggles high when VSTOR ramps up	2.65	2.8	2.95	V
	VBAT_OK indication toggles low when VSTOR ramps down	2.25	2.4	2.55	V
MPPT	Maximum Power Point Tracking, Programmed % of Open Circuit Voltage		78%		
C _{BAT}	Battery Pin Capacitance or equivalent battery capacity	100			μF

3 Test Summary

3.1 Equipment

Power Supplies

Power Supply #1 (PS#1): Adjustable 5V Power supply with Current Limit of 100mA.

Power Supply #2 (PS#2): Adjustable 5V Power supply with 20Ω series impedance (can just be a discrete resistor) with Current Limit of 100mA.

Loads

Load #1: 10kΩ, 5%, 0.25W resistor and 1kΩ, 5%, 0.25W resistor as per procedure P/S#2 series resistance: 20Ω, 5%, 0.25W

Meters

Meter#1,2,3: Fluke 75 multi-meter, (equivalent or better) for voltage measurements

Scope

Standard scope with at least two channels

3.2 Equipment and EVM Setup

Table 1. I/O Connections and Configuration for Evaluation of bq25504 EVM

Jack	Description	Factory Setting
J1–VIN	Input Source (+)	
J1–GND	Input Source Return (-)	
J2–BAT	Battery connection (+)	
J2–GND	Battery Connection Return (-)	
J3 – VIN	Input Source Sense (+) [for J1]	
J3 -GND	Input Source Return Sense (-) [for J1]	
J4 – BAT_OK	Battery Status Indicator (+)	
J4 - GND	Battery Status Indicator Return (-)	
J5 – STOR	Charger Output (+)	
J5 – GND	Charger Output Return (-)	
J6 – STOR	Charger Output Sense (+)	
J6 – BAT	Battery Connection Sense (+) [for J2]	
J6 - GND	Battery Connection Sense (-) [for J2]	
JP1	MPPT setting: Enabled-Divider; Disabled-STOR	Place Shunt on JP1-2/3 (Divider)
JP2	OCS Setting: C5 Capacitor-No Shunt; Disabled-Shunt on REF-GND (JP1 should be Disabled)	No Shunt

eZ430-RF2500 Development Tool

1 eZ430-RF2500 Overview. Wireless Made Easy.

The eZ430-RF2500 is a complete USB-based MSP430 wireless development tool providing all the hardware and software to evaluate the MSP430F2274 microcontroller and CC2500 2.4-GHz wireless transceiver.

The eZ430-RF2500 uses the IAR Embedded Workbench Integrated Development Environment (IDE) or Code Composer Studio™ (CCS) IDE to write, download, and debug an application. The debugger is unobtrusive, allowing the user to run an application at full speed with both hardware breakpoints and single stepping available while consuming no extra hardware resources.

The eZ430-RF2500T target board is an out-of-the box wireless system that may be used with the USB debugging interface, as a stand-alone system with or without external sensors, or may be incorporated into an existing design.

The USB debugging interface enables the eZ430-RF2500 to remotely send and receive data from a PC using the MSP430 Application UART.

eZ430-RF2500 features:

- USB debugging and programming interface featuring a driverless installation and application backchannel
- 21 available development pins
- Highly-integrated ultra-low-power MSP430 MCU with 16-MHz performance
- Two general-purpose digital I/O pins connected to green and red LEDs for visual feedback
- Interruptible push button for user feedback

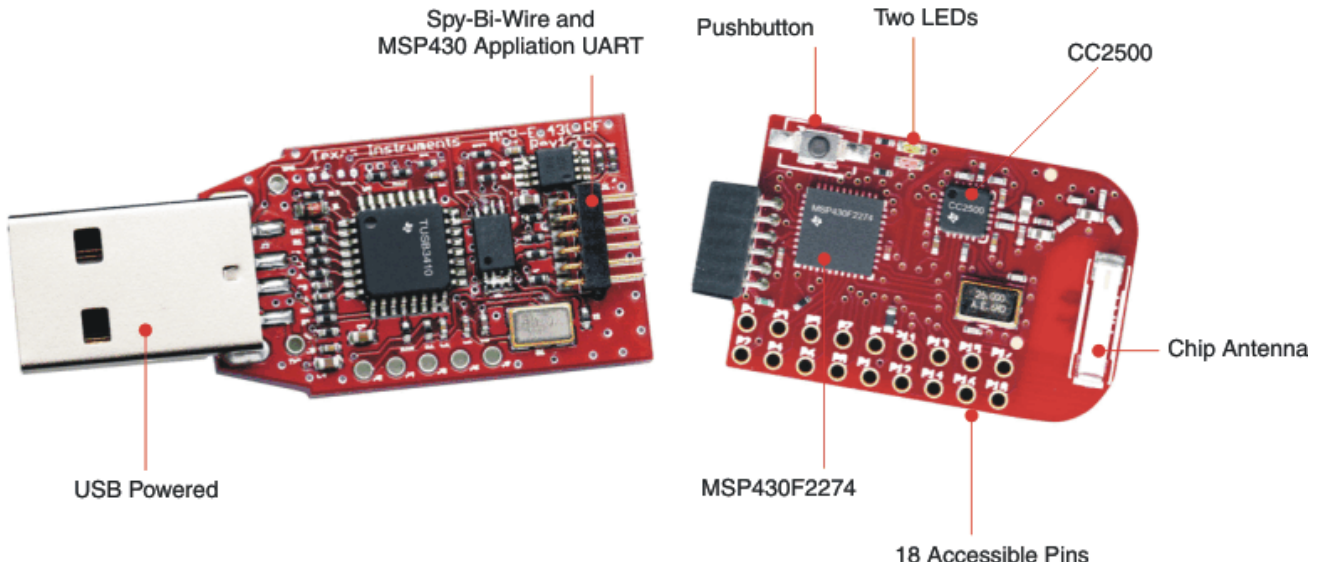


Figure 1. eZ430-RF2500

Table 1. eZ430-RF2500T Target Board Pinouts (continued)

Pin	Function	Description
15	P3.2 / UCB0SOMI / UCB0SCL	General-purpose digital I/O pin USCI_B0 slave out/master in when in SPI mode SCL I ² C clock in I ² C mode
16	P3.3 / UCB0CLK / UCA0STE	General-purpose digital I/O pin USCI_B0 clock input/output USCI_A0 slave transmit enable
17	P3.0 / UCB0STE / UCA0CLK / A5	General-purpose digital I/O pin USCI_B0 slave transmit enable USCI_A0 clock input/output ADC10, analog input A5
18	P3.1 / UCB0SIMO / UCB0SDA	General-purpose digital I/O pin USCI_B0 slave in/master out in SPI mode SDA I ² C data in I ² C mode

Table 2. Battery Board Pinouts

Pin	Function	Description
1	P3.4 / UCA0TXD / UCA0SIMO	General-purpose digital I/O pin USCI_A0 transmit data output in UART mode (UART communication from 2274 to PC) Slave in/master out in SPI mode
2	GND	Ground reference
3	RST / SBWTDIO	Reset or nonmaskable interrupt input Spy-Bi-Wire test data input/output during programming and test
4	TEST / SBWTCK	Selects test mode for JTAG pins on Port1. The device protection fuse is connected to TEST. Spy-Bi-Wire test clock input during programming and test
5	VCC (3.6V)	Supply voltage
6	P3.5 / UCA0RXD / UCA0SOMI	General-purpose digital I/O pin USCI_A0 receive data input in UART mode (UART communication from 2274 to PC) Slave out/master in when in SPI mode